Ph.D. program in Agri-food Engineering and Biotechnology

Improving monitoring and management of low-lying coastal areas with Sentinel-2 data: the Ebro Delta showcase

A thesis submitted to obtain the title of Ph.D.

Jesús Soriano González

Supervisors:

Guido Luzi, Centre Tecnològic de Telecomunicacions de Catalunya (CTTC), Unitat de Recerca de Geomàtica.

Carles Alcaraz Cazorla, Institut de Recerca i Tecnologia Agroalimentàries, Programa d'Aigües Marines i Contnentals (IRTA-AMiC).

Tutor:

Lourdes Reig Puig, Universitat Politècnica de Catalunya (UPC), Vicerectora de Política Internacional

Advisor:

Eduard Angelats Company, CTTC, Unitat de Recerca de Geomàtica.

Castelldefels, November 2022

Preface

Aquesta tesi doctoral sorgeix com a continuació de la tesina 'Caracterización de la dinámica espacial del fitoplancton en las bahías del delta del Ebro a partir de la estimación de la clorofila-a con Sentinel-2: Implicaciones para la miticultura', presentada com a treball de fi del màster interuniversitari d'aqüicultura (UPC, UAB, UB).

La tesi s'ha desenvolupat dins el programa de doctorat 'Enginyeria Agroalimentària i Biotecnologia' de la UPC, amb la supervisió dels doctors Guido Luzi (CTTC) i Carles Alcaraz (IRTA), i la tutorització de la doctora Lourdes Reig, en el marc del projecte europeu H2020 'HEIMDALL: Multi-hazard cooperative management tool for data exchange'.

Durant el període de formació predoctoral, J. Soriano-González ha gaudit d'una beca d'ajudes per a la contractació de personal predoctoral en formació (FI) de l'Agència de Gestió d'Ajuts Universitaris i de Recerca (AGAUR).

Acknowledgments

Han sigut quatre anys llargs, tres comunitats autònomes, dos-centes onades Covid, tres centres de recerca, molts mals de cap, més d'una satisfacció i, sobretot, innumerables companys de viatge. Aquesta secció és per vosaltres, també pels que no apareixeu, però sabeu que hi hauríeu de ser.

Primer, per la família. Els de sempre, la mama, el papa i la tata, els que no fallen i a qui no puc fallar; companys de vida incondicionals i, sens dubte, el meu màxim suport. Soc qui soc i estic on estic per vosaltres, us ho dec tot i ni aquest, ni qualsevol altre agraïment, seria just i suficient per tot el que heu fet, feu i fareu per mi. És això, sou atemporals, sinònim d'estabilitat, una sort que tinc garantida, el meu major poder, sou un deute que mai podré pagar.

Per la família nova, l'ala valenciana, la de 'Los del Polar y Tomás', la bona gent d'Alfafar. El vostre tracte i la forma d'acollir-me han sigut clau en la meva etapa final de doctorat; m'heu fet sentir un més des del primer dia. Sou un gran equip del qual estic feliç i orgullós de poder formar part. Vau aparèixer del no-res, per algú que per mi ara ho és tot. El meu dia a dia, qui em pateix contínuament, l'única persona capaç de recolzar-me en tots, absolutament tots, els aspectes de la vida. Elena, plenes els meus buits, i fas grans les meves virtuts. Ets font de consell i d'alegries i has sigut un pilar fonamental per a acabar aquesta etapa; continuem creixent junts.

També pels meus tiets, els tetes Jose i Juanjo, als que espero fer sentir tan orgullosos com jo em sento d'ells. Per seguir gaudint amb vosaltres mil anys més, escoltant-vos i llegint-vos.

Per vosaltres, els supervisors oficials, els oficiosos, i els no supervisors, guies indiscutibles des de 2017 de la meva vida acadèmica, professional i, sovint, personal. Carles, María, Eduard, Eulàlia i Guido. Aquells que vau signar l'adopció quasi sense llegir les condicions, i vau assumir les conseqüències. M'heu aportat enfocaments molt diferents dins i fora de la recerca, sou imprescindibles d'aquells que fa uns anys no sabia que necessitava. M'emporto cadascun dels segons que he passat amb vosaltres; un temps d'aprenentatge i connexió. M'emporto cinc companys d'un viatge ple de pujades i baixades, xerrades, dinars, consells, revisions (algunes en plan escorxador), i una sensació brutal de suport incondicional. Tots vosaltres formeu part del jack pot d'aquesta tesi, un extra de valor incalculable que és meu per sempre.

Per la resta de Geomàtica; els del cafè virtual dels divendres liderats pel mític Pep, i els del despatx del costat, on és l'Anna. Tant pels que heu fet fotos de la platja, com pels que no. Per tots els que continueu, els nouvinguts, i pels que es van baixar del tren. També per les irreemplaçables, i sempre disponibles Susi, Cris, Ana, Montse, Jona, i Jordi, de la cara amagada del B4. Amb vosaltres tot ha sigut sempre fàcil.

Pels B6 originals, la gent de les cavernes. Especialment per en Carlos, en Fabiano, i la Vrinda, per tots els bons moments i la companyia dins i fora de les coves, perquè sou el més gran que m'emporto. També per l' Àngel, la Laura, i en Moha, i per tots els que heu fet aquesta etapa més lleugera i divertida. Sou uns personatges a qui sempre m'agradaria tindre a prop; ens tornarem a trobar.

Per a les dues persones més importants de l'altre passadís del campus. La Lourdes, peça fonamental en l'existència de la meva tesi, professora i tutora, el vincle institucional i, sens dubte, el tret de sortida d'aquest doctorat. I la Montserrat, imprescindible en la meva relació amb l'escola, atenta i sempre súper resolutiva. M'heu aplanat moltíssim el camí, sempre responent als meus dubtes, i mostrant una paciència infinita. Perdó per tots els meus moments incendiaris; us estaré eternament agraït pel vostre tracte i compromís. Afortunat el DEAB de poder comptar amb vosaltres, i afortunat jo d'haver-ho pogut viure.

Per a tota la gent del Delta; en Jorge i els AMICs, que em van rebre a l'IRTA. Per a la colla de l'antic SMM, amb el Patró i els dies a mar i les matinades, la tutela de l'Ester i la Vanessa, i els seus ous; i tots els que m'heu fet un més durant les meves estades. Tècnicament, i a la pràctica, aquest dia no hauria arribat sense vosaltres. També per a tots els doctorands que sempre m'han tractat com un més tot i ser un estrany intermitent. I el més especial, en Riki, una casualitat del doctorat, un gran company, la meva seu al Delta, i font de moltes convivències.

Pels amics de València, els de sempre, i pels nous col·legues. En especial, per la gent de l'IPL, en Jesús, la Patricia, l'Antonio i tota la colla a qui em van introduir. Em vau oferir formació, bon rotllo, i heu fet profitosa la meva estada en molts sentits. Espero repetir el Bienmesabe, l'Albufera i que continuem descobrint junts. Estic súper agraït de la vostra acceptació i tutela. La tesi i jo ens emportem un bon grapat de coneixement de València, el vostre mèrit.

Pels de la sorra, per tots els amics de vòlei, i ara de fora; en Gonçalo, la Marta, en Roger, l'Adri, la Mar i tots aquells que m'heu fet desconnectar al sol, i sota la pluja.

I, per acabar, tornem als orígens. Aquesta secció també va per vosaltres despenyats de Sant Andreu. Els que sembla que no estan mai, però estan des de sempre. El Monxi, l'Ernol, el Campi, el Quim, el Xavi, el Zarza, el Geri, el Cuesta, el Cabes, i el recuperat Moyano. Vosaltres sou una constant. Amb tesi o sense, esteu des de la infància, formeu part de qui soc. Papus, continuem comptant anys i recollint mèrits junts.

A totes i tots, gràcies! Mai haguera arribat fins aquí sol.

Jesús Soriano González
Castelldefels, 2022

CONTENTS

List of Figures

Chapter 1. Introduction

Chapter 2. Sentinel-2 for aquaculture

Chapter 3. Impact of agriculture runoff on coastal waters

Chapter 4. Sentinel-2 for agricultural monitoring

Chapter 5. Atmospheric correction in inland and coastal waters

Chapter 6. Monitoring coastal storm's effects with Sentinel-2

Chapter 7. General discussion and Further research

Chapter 8. Conclusions

List of Tables

Abstract

Coastal areas support important ecosystems with great ecological value, giving rise to countless resources increasingly exploited by humans. Understanding the processes occurring in both inland and aquatic ecosystems, as well as their mutual interactions, and with anthropic activities is required. In this line, the new generation of high-resolution multispectral Sentinel satellites (Sentinel-2; S2) extend the capabilities for the integrated monitoring of coastal areas thanks to their spatial and temporal resolutions (up to 10 m and 5 days). However, global remote sensing issues/limitations (*e.g.,* cloud screening, spectral mixing, atmospheric correction) and regional-specific characteristics (*e.g.*, involved ecosystems, economic fabric, interlinkages), make up challenges of diverse nature. The basis of the research presented in this thesis is to explore the potential of S2 for the monitoring of coastal areas, and the associated technical and scientific questions. The work is focused on the processing of S2 imagery for characterizing Ebro Delta (Spain) coastal features and their dynamics, involving aquaculture, agriculture, spatial planning, environmental monitoring, and preparedness for natural hazards. From atmospheric correction and image pre-processing (first steps) to data modelling and analysis (last steps), a number of technical and scientific challenges have been addressed.

In coastal waters, different atmospheric correction levels, processors, spectral combinations, and statistical models have been used for mapping water quality (*i.e.,* chlorophyll-*a*, Secchi disk depth) and macrophytes (*i.e.,* seagrass, macroalgae). For estimating chlorophyll-*a* (proxy of phytoplankton biomass), the best results were obtained using simple ratios including visible and/or red-edge bands applied to Rayleigh or full-atmospheric corrected imagery, by fitting either linear or 2nd-degree polynomial (MAE ~ 0.6 mg/m^3), obtaining time series which allowed to relate the distribution of phytoplankton with the environmental and anthropic forcing. The relationship between Secchi disk depth and light attenuation products ($r > 0.75$) demonstrated the feasibility of monitoring water clarity with S2. In relation to the estimation of macrophytes coverage, machine-learning supervised classification of S2 VIS-NIR composites was used for assessing the spatial coverage of seagrass and macroalgae communities in shallow waters, unveiling a negative impact of agricultural runoff on macrophytes' communities. Inland, an automatic method was developed based on the identification of key points in the combined temporal profiles of three common vegetation and land surface water indexes for the extraction of rice phenological metrics, irrigation management, and crop yield proxy. The results provided information on significant rice phenological stages and field status (*e.g.,* rice maturity, hydroperiod), also showing that crop yield is better estimated during the rice heading period ($r = - 0.8$). Finally, for assessing storms' effects with S2, a combined flooding-water quality monitoring method was defined and implemented, reaffirming the capabilities of S2 for depicting the different grades of land and aquatic environments' resilience.

The conducted research has been applied to the estimation of phytoplankton biomass at coastal bays (aquaculture), the generation of information on crop dynamics and management (agriculture), the assessment of agriculture runoff disturbance in coastal waters (environmental monitoring), and the characterization of storms' effects on land and water ecosystems (natural hazards). A work that brings the application of satellite image processing to scientists, engineers, coastal managers, and stakeholders by providing results that demonstrate the usefulness of these viable and low-cost techniques for high-quality coastal monitoring.

Resumen

Las zonas costeras albergan importantes ecosistemas de gran valor ecológico, que dan lugar a innumerables recursos cada vez más explotados por el ser humano. Por ello, es necesario comprender los procesos que ocurren tanto en los ecosistemas terrestres como en los acuáticos, así como sus interacciones mutuas y con las actividades antrópicas. En esta línea, la nueva generación de satélites multiespectrales Sentinel de alta resolución (Sentinel-2; S2) amplía las capacidades para la monitorización integrada de las zonas costeras gracias a su resolución espacial y temporal (hasta 10 m y 5 días). Sin embargo, los problemas/limitaciones globales de la teledetección (*e.g.,* cribado de nubes, mezcla espectral, corrección atmosférica) y las características específicas de cada región (*e.g.,* ecosistemas implicados, tejido económico del lugar, interrelaciones), componen retos de diversa naturaleza. En este sentido, la base de la investigación presentada en esta tesis es explorar el potencial de S2 para la monitorización de zonas costaras, y las cuestiones técnicas y científicas asociadas. El trabajo se centra en el procesamiento de imágenes S2 para la caracterización de aspectos costeros del Delta del Ebro (España) y su dinámica, involucrando la acuicultura, la agricultura, la planificación espacial, el seguimiento medioambiental, y la preparación ante riesgos naturales. Desde la corrección atmosférica y el preprocesamiento de las imágenes (primeros pasos) hasta el modelado y el análisis de los datos (últimos pasos), se han abordado distintos retos técnicos y científicos.

En las aguas costeras, se han utilizado diferentes niveles de corrección atmosférica, procesadores, combinaciones espectrales y modelos estadísticos para cartografiar la calidad del agua (*i.e.,* clorofila-*a*, profundidad del disco de Secchi) y los macrófitos (*i.e.,* praderas marinas, macroalgas). Para estimar la clorofila-*a* (indicador de la biomasa fitoplanctónica), los mejores resultados se obtuvieron utilizando ratios simples que incluían bandas visibles y/o del borde rojo aplicados a imágenes corregidas por Rayleigh o con corrección atmosférica completa, con un ajuste lineal o polinomial de 2º grado (*MAE* ~ 0,6 mg/m^3), obteniendo series temporales que permitieron relacionar la distribución del fitoplancton con el forzamiento ambiental y antrópico. La relación entre la profundidad del disco Secchi y los productos de atenuación de la luz (r > 0,75) demostró la viabilidad de la monitorización de la claridad del agua con S2. En cuanto a la estimación de la cobertura de macrófitos, la clasificación supervisada por aprendizaje automático de composiciones de bandas VIS-NIR de S2 fue útil para evaluar la cobertura espacial de las comunidades de praderas marinas y macroalgas en aguas poco profundas, revelando un impacto negativo de la escorrentía agrícola en las comunidades de macrófitos. En el interior, se desarrolló un método automático basado en la identificación de puntos clave en los perfiles temporales combinados de tres índices comunes de vegetación y agua superficial de la tierra para la extracción de métricas fenológicas del arroz, la gestión de la irrigación y la aproximación al rendimiento de los cultivos. Los resultados proporcionaron información significativa sobre las etapas fenológicas del arroz y el

estado del campo (*e.g.*, madurez del arroz, hidroperiodo), mostrando también que el rendimiento del cultivo se estima mejor durante el período de floración del arroz (r = - 0,8). Por último, para evaluar los efectos de las tormentas con S2, se definió e implementó un método combinado de monitorización de la calidad del agua e inundaciones, reafirmando la capacidad de S2 para representar los diferentes grados de resiliencia de los entornos terrestres y acuáticos.

Esta investigación se ha aplicado a la estimación de la biomasa de fitoplancton en bahías costeras (acuicultura), a la generación de información sobre la dinámica y gestión de los cultivos (agricultura), a la evaluación de las alteraciones de la escorrentía agrícola en el medio marino (vigilancia ambiental) y a la caracterización de los efectos de las tormentas en los ecosistemas terrestres y acuáticos (riesgos naturales). Un trabajo que acerca las aplicaciones del procesamiento de imágenes satelitales a científicos, ingenieros, gestores costeros y partes interesadas, proporcionando resultados que demuestran la utilidad de estas técnicas viables y de bajo coste para la monitorización costera de alta calidad.

Resum

Les zones costaneres alberguen importants ecosistemes de gran valor ecològic, que donen lloc a innumerables recursos cada cop més explotats per l'ésser humà. Per això, és necessari comprendre els processos que ocorren tant en els ecosistemes terrestres com en els aquàtics, així com les seves interaccions mútues i amb les activitats antròpiques. En aquesta línia, la nova generació de satèl·lits multiespectrals Sentinel d'alta resolució (Sentinel-2; S2) amplia les capacitats per a la monitorització integrada de les zones costaneres gràcies a les seves resolucions temporals i espacials millorades (fins 10 m i 5 dies). Tanmateix, els problemes/limitacions globals de la teledetecció (*e.g.,* triatge de núvols, barreja espectral, correcció atmosfèrica) i les característiques específiques de cada regió (*e.g.,* ecosistemes implicats, teixit econòmic del lloc, interrelacions), composen reptes de diversa naturalesa. En aquest sentit, la base de la investigació presentada en aquesta tesi és explorar el potencial de S2 per a la monitorització de zones costaneres, i les qüestions tècniques i científiques associades. El treball es centra en el processat d'imatges S2 per a la caracterització d'aspectes costaners al Delta de l'Ebre (Espanya) i la seva dinàmica, involucrant l'aqüicultura, l'agricultura, la planificació espacial, el seguiment mediambiental, i la preparació front a riscos naturals. Des de la correcció atmosfèrica i el pre-processat de les imatges (primers passos) fins el modelat i l'anàlisi de les dades (últims passos), s'han abordat diferents reptes tècnics i científics.

En aigües costaneres, s'han utilitzat diferents nivells de correcció atmosfèrica, processadors, combinacions espectrals i models estadístics per a cartografiar la qualitat de l'aigua (*i.e.,* clorofil·la-*a*, profunditat del disc de Secchi) i els macròfits (*i.e.,* praderes marines, macroalgues). Per estimar la clorofil·la-*a* (indicador de biomassa fitoplanctònica), els millors resultats es van obtenir utilitzant ratis simples entre les bandes visibles i/o del marge vermell aplicats a imatges corregides per Rayleigh o amb correcció atmosfèrica complerta, amb un ajust linial o polinomial de 2n grau ($MAE \sim 0{,}6$ mg/m^3), obtenint series temporals que van permetre relacionar la distribució del fitoplàncton amb el forçament ambiental i antròpic. La relació entre la profunditat del disc de Secchi i els productes d'atenuació de la llum ($r > 0.75$) va demostrar la viabilitat de la monitorització de la claredat de l'aigua amb S2. En quan a l'estimació de la cobertura de macròfits, la classificació supervisada per aprenentatge automàtic de composicions de bandes VIS-NIR de S2 va ser útil per avaluar la cobertura espacial de las comunitats de praderes marines i macroalgues en aigües poc profundes, revelant un impacte negatiu de l'escorrentia agrícola en comunitats de macròfits. A l'interior, es va desenvolupar un mètode automàtic basat en la identificació de punts clau en els perfils temporals combinats de tres índex comuns de vegetació i aigua superficial de la terra per a la extracció de mètriques fenològiques de l'arròs, la gestió de la irrigació i l'aproximació al rendiment dels cultius. Els resultats van proporcionar informació significativa sobre les etapes fenològiques de l'arròs i l'estat del camp (*e.g.,* maduresa de l'arròs, hidroperíode), mostrant també que el rendiment del cultiu s'estima millor durant el període de

floració de l'arròs (r = - 0.8). Per últim, per avaluar els efectes de les tempestes amb S2, es va definir e implementar un mètode combinat de monitorització de la qualitat de l'aigua i les inundacions, reafirmant les grans capacitats de S2 per a representar els diferents graus de resiliència dels entorns terrestres i aquàtics.

Aquesta investigació s'ha aplicat a l'estimació de la biomassa del fitoplàncton en badies costaneres (aqüicultura), a la generació d'informació sobre la dinàmica i gestió dels cultius (agricultura), a l'avaluació de les alteracions de l'escorrentia agrícola en el medi marí (vigilància ambiental) i a la caracterització dels efectes de les tempestes en ecosistemes terrestres i aquàtics (riscos naturals). Un treball que apropa les aplicacions del processat d' imatges de satèl·lit a científics, enginyers, gestors costaners i parts interessades, proporcionant resultats que demostren la utilitat d'aquestes tècniques viables i de baix cost per a la monitorització costanera d'alta qualitat.

Chapter 1

INTRODUCTION

1.1. BACKGROUND AND RESEARCH JUSTIFICATION

Coastal areas support highly dynamic and productive ecosystems of great ecological and economic value (Ramírez-Pérez et al., 2017). They are key sites for human development since more than 40 % of the world's population inhabit them, including 60 % of the world's major cities (Nicholls et al., 2007). Anthropic and natural processes coexist and interact between them mediated by environmental fluctuations. Understanding the relationship and the interaction among overlapping land uses (*e.g.,* urban areas, tourism, agri-food industry, ecosystem services) is essential information for decision-making and the development of an Integrated Coastal Zone Management (ICZM) program at local, regional, and global scale (Fabbri, 1998). ICZM must include the protection of the coastal environment, preserving its integrity and functioning, and leading to the sustainable management of the natural resources (European Comission, 2002).

The development and implementation of ICZM impose the prerequisite of understanding inland and aquatic processes, as well as their interactions and their relationship with human activities. The high spatiotemporal variability of the environment is a challenge for observing systems and monitoring programs (surveying methods), and the complex interlinkages with human activities trends make it difficult to understand when the system is responding to natural or human-mediated changes. Consequently, ICZM needs to integrate multiscale observing systems, high-frequency information, and complete geographic coverage (Hinton, 1996; Ramírez-Pérez et al., 2017).

Satellite remote sensing imagery is increasingly able to satisfy these data needs, mainly because of its unique capability for regular and repeated observation of specific regions at different spatial scales (Dean and Populus, 2013). In remote sensing, the image acquired is related to electromagnetic properties of the Earth and, under different conditions, it can be related to real-world parameters (Bakker et al., 2001). A broad variety of sensing methods exist, using different sources of radiation (active and passive sensors) and handling various wavelengths from ultraviolet (UV) to infrared (IR) and microwave regions, thus defining the limits of the electromagnetic spectrum in which remote sensing operates.

Among the different sensing methods, multispectral sensors (optical domain) including the visible (VIS), near-infrared (NIR), and shortwave infrared (SWIR) regions of the spectrum are of particular interest for comprehensive monitoring of coastal areas. These sensors have been successfully applied to assess the state and evolution of land cover, land use, and land inundation (Pekel *et al.*, 2014; Phiri *et al.*, 2019), ground and aquatic vegetation (Van Niel and McVicar, 2004; Hossain *et al.*, 2015), water quality (Matthews, 2011; Gholizadeh *et al.*, 2016), and submerged and emerged coastal morphology (Lyzenga *et al.*, 2006; Sánchez-García *et al.*, 2020). Therefore, multispectral remote sensing can tackle coastal monitoring as a whole,

with an important contribution to the management of critical terrestrial and aquatic ecosystem assets and services (Ustin, 2004), natural hazards preparedness and response (Klemas, 2013), and the surveillance and planning of human-made activities such as agriculture (Boschetti *et al.*, 2017), aquaculture (Gernez *et al.*, 2017), and dredging operations (Caballero *et al.*, 2018a).

Since 2014, the Sentinel satellite products of the European Spatial Agency have opened new opportunities for remote sensing in coastal areas. The primary purpose of the Sentinel satellite constellation series is to support the needs of the Global Monitoring for Environmental Security (GMES) program (Berger *et al.*, 2012). Sentinel long-term data (>20 years) meets the rigorous requirements of operational programs, being free, systematic (Malenovský *et al.*, 2012), and available online at the same sensing date. Because of the increase in readiness, coverage, and radiometric, spatial and temporal resolutions, Sentinel's data support a number of operational services related to the monitoring of both the aquatic and terrestrial ecosystems, being a key tool for the development of ICZM systems. The S2 mission comprises a constellation of two polar-orbiting satellites placed in the same sun-synchronous orbit (S2-A and S2-B), that is planned to be extended with S2-C in 2024 and S2-D in 2025. Its wide swath (290 km), high-resolution (10-20-60 m) MultiSpectral Imagery sensor (MSI - Figure 1), and high revisit frequency - 5 days at least and up to 2 days where multiple orbits overlap – (ESA, 2017), allow the monitoring of environmental changes at the same, or similar, time frame in which they occur.

Despite the advances in satellite platforms and sensors, there are some limitations in the use of multispectral remote sensing. Optical sensors are restricted to day-time and cloud-free conditions, since they rely on solar reflectance from the Earth's surface (Matgen *et al.*, 2020). Optical remote sensing cannot penetrate clouds, even in partially clear sky conditions, and cloud screening may be a difficult task. Cloud coverage significantly reduces the timeliness and consistency of the observations, emphasizing the importance of the native temporal resolution of the satellite platforms. Clouds also lead to large uncertainties in many applications due to Earth's Surface shadowing (Zhang *et al.*, 2013). Pixels affected by cloud shadows present reduced radiances in reflective bands, and usually are spectrally confused with water surface (Wang *et al.*, 2019). Consequently, coastal areas represent a complex scenario by including different land and water types, such as agriculture, urban areas, lagoons, and wetlands.

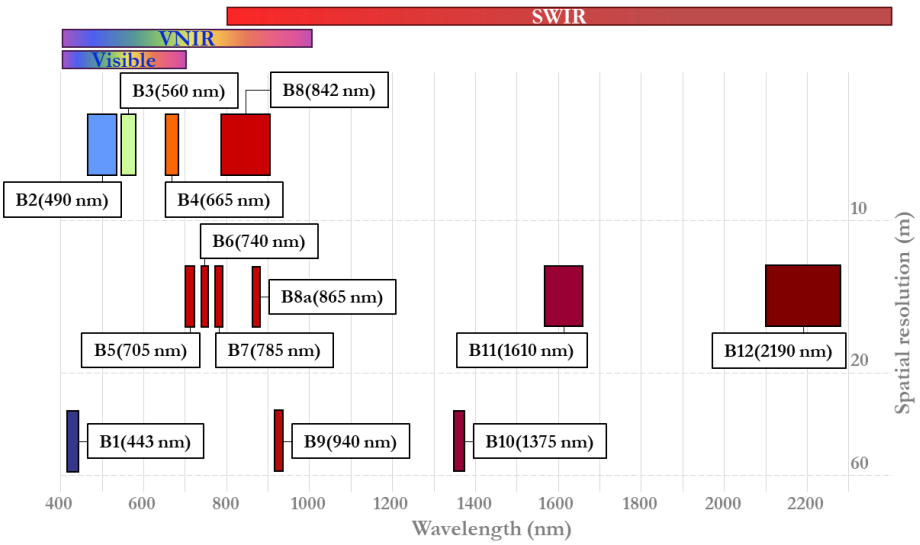

Figure 1. S2 spectral bands. Bandwidth (rectangles) ranges from 15 nm to 180 nm. Adapted from (ESA, 2017).

Another constraint common to different satellite platforms is the spectral mixture problem, associated with the spatial resolution of the sensors. Since a sensor measures the intensity of radiant flux of electromagnetic energy of portions of the Earth's surface (pixel size), the radiation flux originated is a mixture of different fluxes of radiation (*i.e.* from different features), resulting in a single measure of intensity by pixel in each spectral region in which the sensor operates (Shimabukuro *et al.*, 2017). This is a critical issue for varied remote sensing applications such as landcover classification or submerged vegetation monitoring, particularly in coastal areas with high spatial heterogeneity. Thus, misclassification may occur when a pixel contains two or more classes, producing a spectral response that does not match the characteristics of any of them (Ranson, 1975). This highlights the importance of the sensor's spatial resolution, with S2-MSI being one of the best open-data satellite solutions.

A major issue in the use of multispectral remote sensing data is the removal of the atmospheric effects in the signal received at the satellite sensor (the top of the atmosphere - TOA). Electromagnetic energy travelling through the atmosphere is absorbed, transmitted and/or scattered by the molecules and particles present, depending on the atmospheric composition and the wavelength (Baker *et al.*, 2001). Thus, atmospheric correction is necessary for the accurate and consistent retrieval of surface reflectance at the bottom of the atmosphere (BOA). The fundamental philosophy of atmospheric correction is to determine the optical characteristics of the atmosphere and apply this to correct imagery data. Atmospheric correction over land is the simplest case, with official and standardized processes for most of the multispectral satellites, S2 included (Main-Knor *et al.*, 2017). Compared to vegetation

or soil, water has lower reflectance - only reflects 10 % of the incoming radiation between the VIS and the NIR in oceanic waters (IOCCG, 2010) -, making atmospheric correction more difficult. Complexity increases in the land-water interaction zone. In coastal areas such as deltas, land runoff propitiates a more heterogeneous aquatic environment, where inorganic and/or organic sediments may make a dominant contribution to the optical properties (Prieur and Sathyendranath, 1981), requiring more accurate and precise atmospheric correction algorithms. Despite different methods have been proposed, atmospheric correction over coastal waters has not been totally solved yet.

Although remote sensing data can be processed and interpreted without other information, the use of ground (or surface) truth data is crucial for the development and adjustment of algorithms, and for assessing estimates' uncertainty (Baker *et al.*, 2001). The synchronization of ground-based survey data and remotely sensed data effectively ensures that the temporal dynamics of the observed variable are considered (Liu *et al.*, 2003). Representative field surveys should include data collected over all possible scenarios (*e.g.,* seasonal, atmospheric, optical, and site-specific conditions), which is costly and time-consuming, particularly in coastal areas due to the environmental heterogeneity, both in time and space, and the great number of parameters to consider (*e.g.*, turbidity, chlorophyll, and vegetation).

Despite it is still necessary to address scientific and technical questions, because of all the above-mentioned features, the S2 constellation has the potential to contribute to ICZM planning strategies. In order to fill the gaps, it is recommended to focus on a study site with an independent assessment of the considered issues. In this sense, the coastal region of the Ebro Delta is an excellent study area.

The Ebro Delta (NE Iberian Peninsula), with an extension of *ca.* 32,500 ha, is one of the largest deltas in the northwestern Mediterranean Basin (Figure 2). The climate is Mediterranean temperate with warm dry summers and cool wet winters, annual mean temperature ranges between 5 and 33 °C, and annual precipitation from 500 to 600 mm, with a maximum in autumn and a minimum in summer. The Ebro Delta is a low-lying coastal area (*ca.* 50 % of the delta surface is below +0.5 m above mean sea level) with sandy, silty, and clay supplied by the Ebro River. River flow and sediment transport are modulated by the presence of *ca.* 200 large dams, mainly built for hydroelectricity and irrigation purposes. In the lower section, the construction of two large dams in the 60's (about 100 km upstream from the river mouth) has reduced *ca.* 99 % of the sediment transport (Rovira *et al.*, 2012; Ibañez *et al.*, 2019). Thus, the delta has reversed the growing trend both seaward and vertically (Sánchez-García *et al.*, 2019). Currently, the Ebro Delta presents a wave-dominated coast with strong reshaping processes (Sayol and Marcos, 2018), highly exposed to storms and extreme events, and subjected to massive flooding, beach erosion, and overwash episodes (Jiménez et al., 2020). The delta contains a number of natural ecosystems (*e.g.,* wetlands, coastal lagoons, sand spits, and freshwater springs) that provide suitable habitats for diverse and abundant fauna and flora. Given the high ecological

value, the Ebro Delta is protected by the Natura 2000 network of the European Union, as Natural Park, and cataloged as UNESCO Biosphere Reserve.

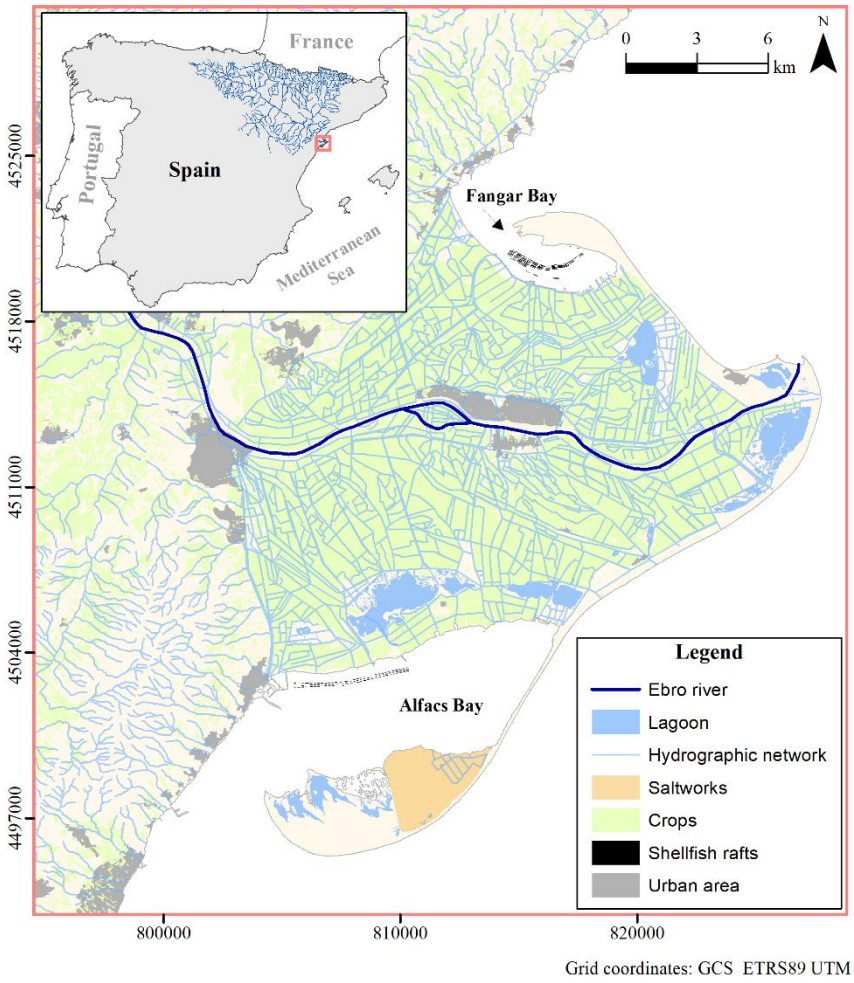

Figure 2. The Ebro Delta (NW Mediterranean, Spain).

Freshwater and nutrient inputs from the Ebro River allow the development of prosperous fishery, aquaculture, and agriculture activities. Agriculture is one of the main economic activities in the area, with *ca.* 65 % of the delta surface devoted to rice production (Genua-Olmedo *et al.*, 2016), in addition to the production of bivalves (shellfish aquaculture), and fishery, albeit saltworks are also part of the economic fabric of the region (Figure 2). The management of the different economic activities has direct implications for themselves, on others, and for the sustainability of the surrounding environment. For instance, the discharge from the rice paddies to Alfacs and Fangar bays influences the spatial and temporal dynamics of both physicochemical and biological water parameters (*e.g.,* salinity, temperature,

hydrodynamics, nutrient load, sediment), with significant implications for macrophytes development and shellfish aquaculture (Soriano-González *et al.*, 2019 and 2020). Shellfish farming generates organic matter (*i.e.*, faeces), increasing dissolved oxygen demand, and modifying seabed characteristics, the biotope, and the biocenosis (*i.e.*, the ecosystem), which can be interfering with fishery.

Because of the high ecological and economic value of the Ebro Delta, and their relationship, it is necessary to implement an ICZM system. It is essential to monitor intra- and inter-annual dynamics, particularly at small scales, both in space and time. Consequently, Sentinel-2 capabilities to monitor coastal areas and their environments need to be assessed, as well as scientific and technical limitations and potentialities discussed.

1.2. OBJECTIVES

The general objective of this thesis is to evaluate the application of S2 imagery for coastal monitoring with an integrated approach. With this aim, different strategies were combined, focused on covering several scientific and technical gaps in the use of S2 in coastal areas (global scale), and site-specific monitoring requirements and applications (regional scale). The specific objectives are:

Chapter 2:

(i) Explore the potential of coupling S2 imagery, different atmospheric correction levels, spectral indexes and ground truth measurements for chl-*a* estimates, and its possible contribution to aquaculture management.

(ii) Define a preliminary procedure and its constraints for time series mapping of phytoplankton biomass at Alfacs and Fangar bays.

(iii) Identify the main sources of uncertainty and error, and derive further research lines.

Chapter 3:

(iv) Evaluate a method for the identification and differentiation of macroalgae and seagrass at 20 m spatial resolution.

(v) Conduct a generalized analysis of rice crop dynamics and management and seek the potential relationship with the macrophytes' spatiotemporal dynamics in Alfacs bay.

(vi) Identify the remaining technical/scientific challenges to be tackled in further research.

Chapter 4:

(vii) Exploit a cloud computing platform and implement improved methodologies for generating cloud-free time series of S2 imagery.

(viii) Develop a method for the automatic extraction of key phenological features and management practices at field-scale by combining different S2-derived spectral indexes.

(ix) Analyze the identified rice crop dynamics and yield along consecutive years in the Ebro Delta, and discuss the potential of the method for evolving to pixel-scale and its possible applications/contributions.

(x) Provide ideas for further research aiming at the improvement of the proposed method and at the refinement of the overall image processing chain.

Chapter 5:

(xi) Assess and compare the performance of the three currently available Case 2 Regional Coast Colour (C2RCC) atmospheric correction processors for the retrieval of water reflectance in inland and coastal waters.

(xii) Validate the water quality products generated automatically by the different atmospheric correction processors with *in situ* chl-*a*, Total Suspended Matter (TSM), and Secchi Disk depth measurements.

(xiii) Define potential use cases and the main limitations of the C2RCC processors for the operational monitoring of water quality.

(xiv) Identify gaps of knowledge and propose further research lines addressing them.

Chapter 6:

(xv) Develop and implement a new procedure for chl-*a* estimation from S2 imagery, ensuring the temporal consistency of the results by applying a full atmospheric correction.

(xvi) Devise and test a new semi-supervised method for the rapid mapping of inundation for storm periods involving short temporal scales.

(xvii) Contribute to the definition of requirements (further improvements and needed research in the short-mid term) for a workflow for rapid mapping and continuous monitoring of storm emergencies in the Ebro Delta and similar deltaic areas.

1.3. DOCUMENT OVERVIEW

This document is divided into eight chapters, and together with the introduction, the general discussion, and the conclusions, it includes the edited versions of three

international peer-reviewed publications and two peer-reviewed international conference papers. Each chapter starts with a preface that links it with the other ones. The structure of the chapters and the chronological diagram of the research is summarized in Figure 3.

Briefly, the research started with the retrieval of water quality (*i.e.,* chl-*a)* for the estimation of phytoplankton biomass and its potential applications to aquaculture (Chapter 2). Macrophytes and atmospheric correction uncertainty in coastal waters appeared among the most important external factors for the accurate retrieval of chl-*a*. This led to study the macrophytes detection with S2 and their potential as sentinel species (Chapter 3), and to conduct an in-deep exploration of the atmospheric correction processors (Chapter 5). The drainage of the rice paddies canals also had significant importance in the modulation of the phytoplankton and macrophytes dynamics in coastal waters, motivating the study of rice paddies management and development (Chapter 4). In this last study, one of the topics was related to the identification of flooded and dry rice fields. The findings regarding the capabilities of S2 and the methods for surface water discrimination (Chapter 4), together with the evolution of the procedure for chl-*a* estimation (Chapters 2 and 5), were used for assessing storm effects in terms of land inundation and coastal water quality (Chapter 6). In Chapter 7, a general discussion of the thesis and different lines of further research derived from the work carried out are presented. Chapter 8 summarizes the overall conclusions of all the research conducted.

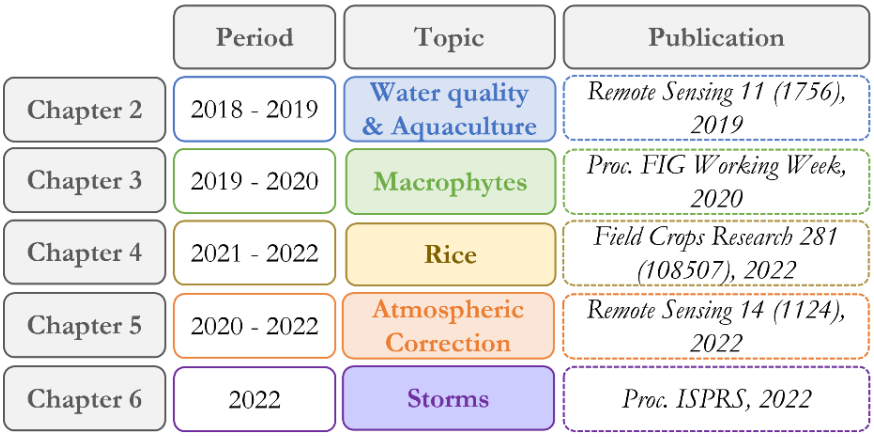

Figure 3. Chronological diagram of the research activity.

Chapter 2

SENTINEL-2 FOR AQUACULTURE

FIRST RESULTS ON PHYTOPLANKTON DYNAMICS IN EBRO DELTA BAYS

An edited version of:

Soriano-González, J., Angelats, E., Fernández-Tejedor, M.; Diogene, J., Alcaraz, C. First Results of Phytoplankton Spatial Dynamics in Two NW-Mediterranean Bays from Chlorophyll-a Estimates Using Sentinel 2: Potential Implications for Aquaculture. *Remote Sensing*. 2019, 11, 1756.

This chapter evaluates the potential application of Sentinel-2 (S2) imagery within the aquaculture industry, discussed from the water quality monitoring point of view in a shellfish farming area. A preliminary method for the monitoring of chlorophyll-*a* (chl-*a*) as a proxy for phytoplankton biomass from S2 data is developed, addressing the methods used for *in situ* samplings, chl-*a* quantification, the processing of S2 imagery, and data post-processing including model development and performance of chl-*a* estimates at different levels of atmospheric correction. Both the potential and limitations of the proposed methodology are discussed, highlighting the main applications and the constraints to be considered in further research for improving the methodology and enabling the evolution to a more integrated approach.

2.1. INTRODUCTION

Shellfish are filter-feeding organisms that feed on different types of suspended particles in the water column, thus their production is mainly related to phytoplankton availability (Duarte *et al.*, 2012). Spain is the leading producer and consumer of bivalves in Europe, Catalonia being the most important producer area in the Spanish Mediterranean, with most of the production concentrated in the Ebro Delta (Figure 4). The most important species for aquaculture are the Mediterranean mussel (*Mytilus galloprovincialis*) and the Pacific oyster (*Crassostrea gigas*), but other bivalves such as clams (*e.g., Ruditapes philippinarum*) and cockles (*e.g., Venus verrucosa*) are also harvested. Bivalve culture is mainly developed inside its two bays, Alfacs and Fangar, representing 1.8% and 6.5% of their respective surfaces (Ramón *et al*, 2005). Since 1990, an official monitoring program carried out by the Regional Government of Catalonia establishes a weekly analysis of the phytoplankton community and water physicochemical parameters at different locations of both bays (12 samples per week). However, the sampling procedure is temporally and spatially limited, so global extrapolations are subject to large uncertainties.

Temporal phytoplankton dynamics are highly influenced by the nutrient input from rice fields through the irrigation network (Prat *et al.*, 1988). Furthermore, freshwater inputs have a great physicochemical impact in both bays, increasing water column stratification and dominating over wind on a seasonal scale (Llebot *et al.*, 2014). Therefore, freshwater input imposes a double-layer circulation system like typical estuarine circulation patterns. However, when channels are closed (from October to April), the water renewal time of the bays increases, forming retention areas that can become accumulation zones. Both scenarios may favor phytoplankton growth. On shorter time scales (days to weeks), the wind is the main controlling factor of water mixing (Artigas *et al.*, 2014) by breaking the vertical stratification. Therefore, water circulation patterns, and hence phytoplankton temporal and spatial variability, depend on freshwater inputs, meteorology, and coastal geomorphology (Camp and Delgado, 1987).

Remote sensing allows obtaining information on marine and continental processes at different spatiotemporal scales (Forget *et al.*, 2009). Chlorophyll-a (chl-*a*) is the main photosynthetic pigment present in algae and an optically active seawater constituent; thus, it is commonly used as an indicator of phytoplankton biomass and has significant implications on remote sensing (Gregor *et al.*, 2004; García *et al.*, 2012; Del López-Rodríguez, 2016; Kutser *et al.*, 2016). The estimation of chl-*a* concentration from remotely sensed data requires the development of algorithms with a maximal sensitivity to chl-*a* and minimal to the rest of the constituents present in the water (Gurlin *et al.*, 2011). Different authors have proposed several methodologies to estimate chl-*a* from satellite remote sensing imagery (see a review in Matthews, 2011; Blondeau-Patissier *et al.*, 2014; Gholizadeh *et al.*, 2016); for instance, a classical approach is developing relationships between band-ratios (namely color indices) or their combinations (Matthews, 2011). Several ratio-based and 3-band combination algorithms have been proposed, including the common Blue to Green ratios, the Ocean Color-based algorithms (Campbell and O'Reilly, 2006; Volpe *et al.*, 2007), and those including the red-edge (Gitelson *et al.*, 1996a; Gitelson *et al.*, 2008; Odermatt *et al.*, 2012; Le *et al.*, 2013), which take advantage of pigment's absorption maxima (*i.e.*, at 665 nm) (Gitelson and Kondratyev, 1991; Oliveira *et al.*, 2016). Other approximations are based on spectral band difference by using band triplets from the Red and Near Infrared (NIR), such as the Fluorescence Line Height (FLH) (Gower *et al.*, 1999), the Maximum Chlorophyll Index (MCI) (Gower *et al.*, 1999), and the Maximum Peak Height (MPH) (Matthews *et al.*, 2012). The properties of coastal waters, however, are controlled by complex interactions and fluxes of material between land, ocean, and atmosphere, which makes challenging to achieve reasonable estimates of water-leaving radiance (removing atmospheric contributions from a signal received at the TOA), and to obtain a robust relationship between water quality and satellite-based parameters (Joshi *et al.*, 2017) integrating the remote sensing and *in situ* measurements. Although a large amount of satellite data is available for remote sensing of chl-*a* (*e.g.,* SeaWiFS, MODIS, MERIS), the fast dynamics of phytoplankton in coastal areas, both temporally and spatially, cannot be fully resolved because of either their coarse spectral, spatial and/or temporal resolution. Currently, the increased frequency (up to five days under ideal conditions) and higher spatial resolution (10 to 60 m) of Sentinel-2 (S2) together with its spectral band configuration has opened a new potential to remote sensing of chl-*a* in coastal zones of small geographical extension, and hence as an alternative for phytoplankton monitoring in coastal areas.

The overall purpose of this study was to analyze the potential of S2 multispectral imagery (MSI) data as a support tool for the future management of shellfish cultures through the monitoring of phytoplankton biomass in the Ebro Delta bays. Thus, this work is a first attempt to assess chl-*a* in a shallow coastal environment with Sentinel 2 imagery data, a free public resource. The objectives of this study were to:

· Generate 20 m resolution chl-*a* maps from S2 MSI imagery covering the whole system;

· Understand the spatiotemporal phytoplankton biomass dynamics by using the derived chl-*a* maps and relating them to environmental variables and the rice farming year;

· Assess the applicability of the results to shellfish aquaculture management in the area.

2.2. MATERIALS AND METHODS

2.2.1. Study sites and *in situ* data

The study area is located in the two bays of the Ebro Delta (Figure 4). Fangar Bay, with an area of 12 km², is connected to the sea by a narrow mouth (*ca.* 1 km wide) that is currently closing. The maximum depth is *ca.* 4 m, which makes it very sensitive to environmental variations. Water temperature ranges between 6.5 and 32 °C, salinity varies from 9 to 37 PSU (Practical Salinity Unit) and renewal time is about four days when channels are open (Camp and Delgado, 1987). Alfacs Bay, covering an area of 56 km² and connected to the sea by a channel of 2.5 km wide, has an average depth of 3.13 m (maximum depth is 7 m). Water temperature ranges between 8 and 32 °C, the salinity varies from 26 to 37 PSU, and the renewal time is about 15 days with open channels (Camp and Delgado, 1987).

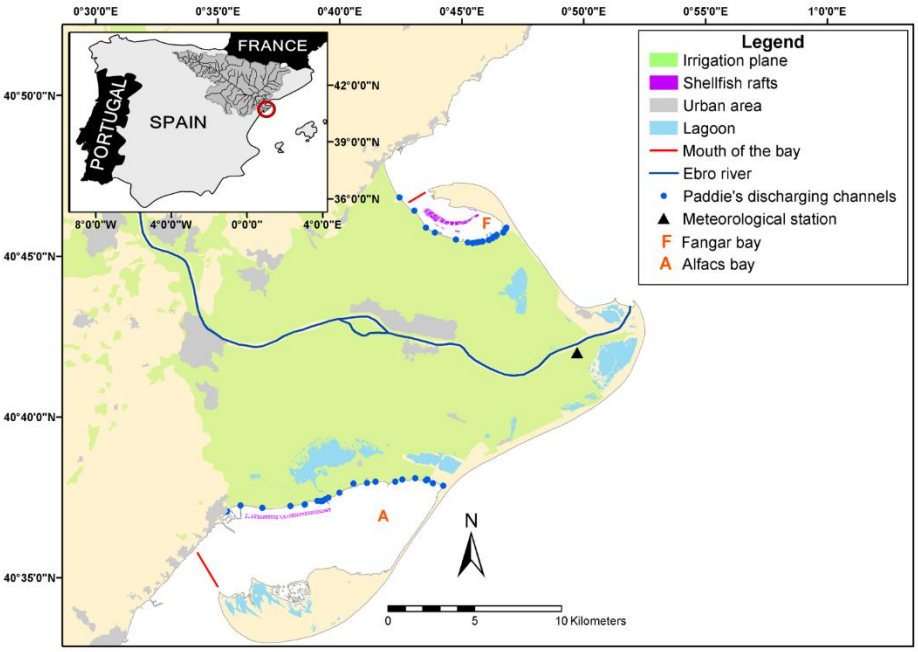

Figure 4. Location of the study bays, meteorological station, mussel rafts, coastal lagoons, irrigation fields, and the discharging channels in Ebro Delta.

Eight water samplings campaigns were carried out from April 2016 to August 2017 coinciding with the S2A satellite pass (Table 1).

Table 1. Summary of chl-a samples coinciding with S2A pass. Grid 1: routine sampling for the official water-quality monitoring program (see orange dots in Figure 5a-b). Grid 2: specific sampling grid designed for ground truth of S2 images (green dots in Figure 5a-2b). Grid 3: sampling grid of the project "Model of water circulation in Fangar Bay from the European Maritime and Fisheries Fund (EMFF)" (white dots in Figure 5b).

Date	Sampling Grid	Bay	Number of Samples per Method		
			in vivo	Fluorimeter	Spectrophoto.
11 Apr 2016	1	Fangar	5	1	0
20 Jun 2016	1	Alfacs	7	1	0
		Fangar	5	1	0
16 Jan 2017	1	Alfacs	7	1	1
17 Mar 2017	1	Alfacs	7	7	7
		Fangar	5	5	5
6 Apr 2017	1	Alfacs	7	7	7
		Fangar	5	5	5
26 May 2017	2	Alfacs	6	6	6
		Fangar	6	6	6
15 June 2017	2	Alfacs	6	6	6
25 Jul 2017	3	Fangar	40[a]	6	0
4 Aug 2017	3	Fangar	40[a]	6	0

[a]: 20 integrated water column samples, and 20 surface water samples at the same locations.

Different sampling grids were used (Figure 5) for different days, and not both of the bays were sampled every day. Integrated water samples were collected using the Lindahl methodology (Sutherland *et al.*, 1992) (N = 106). In addition, on 25 July 2017 and 4 August 2017, surface water samples were collected (N = 40) with polypropylene bottles. Seawater samples were kept in a portable cool box until arrival at the laboratory. In the laboratory, three different methods were used to measure chl-*a* concentration, *in vivo* fluorimetry (Lorenzen, 1996) - hereafter *in vivo* - , and after acetone extraction both in a fluorometer (corrected chl-*a*) - hereafter FL - (Yentsch and Menzel, 1963), and in a spectrophotometer (chl-*a*) - hereafter SP - (Jeffrey and Humphrey, 1975). For all samples (N = 106), chl-*a* was estimated *in vivo*, and in 58 of them, chl-*a* was measured after acetone extraction. Briefly, water samples (550–1000 ml) were filtered using fiberglass filters (GF/F), and filters were submerged in 10 ml of acetone inside 15 ml labeled conical centrifuge tubes. After 24 hours in the fridge (4 °C), they were sonicated for 5 minutes (ultrasonic processor) and centrifuged for 10 minutes at 4000 rpm at 4 °C. The chl-*a*

concentration was then measured in a SHIMADZU UV-1800 spectrophotometer (Shimadzu Corporation, Kyoto, Japan) and/or in a TURNER Trilogy ® fluorometer (Turner Designs, San Jose, California) (Table 1). The datasets generated during the current study are available from margarita.fernandez@irta.cat on reasonable request.

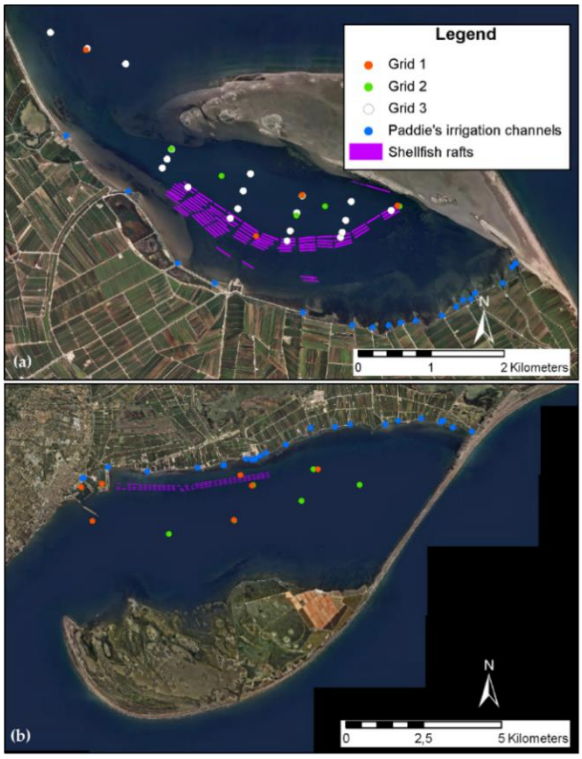

Figure 5. Official water-quality monitoring program sampling grid (Grid 1), specific sampling grid (Grid 2), and European Maritime and Fisheries Fund (EMFF) project sampling grid (Grid 3) at Fangar (a) and Alfacs (b) bays.

2.2.2. Sentinel-2 data

A set of 47 cloud-free S2A L1C images were downloaded from Copernicus Open Acces Hub (https://scihub.copernicus.eu/). Thirteen of them (six from Alfacs and seven from Fangar) within the period April 2016–August 2017 were selected for calibration and validation purposes (Figure 6). The remaining images between January 2017 and January 2018 (Table 1), 18 from Alfacs and 16 from Fangar, were used for time series estimation (Figure 6). Although the calibration/validation (CalVal) image sets covered mainly spring and summer, the time series was estimated for a full year in order to include the full rice-growing season. Additional meteorological data, including daily air temperature (°C), wind direction (°), wind speed (m/s), and precipitation (mm), were obtained from the Illa de Buda meteorological station (Station Id. 11043, located at 1 m above sea level) of the Catalan Meteorological Service, http://www.meteo.cat (Figure 4).

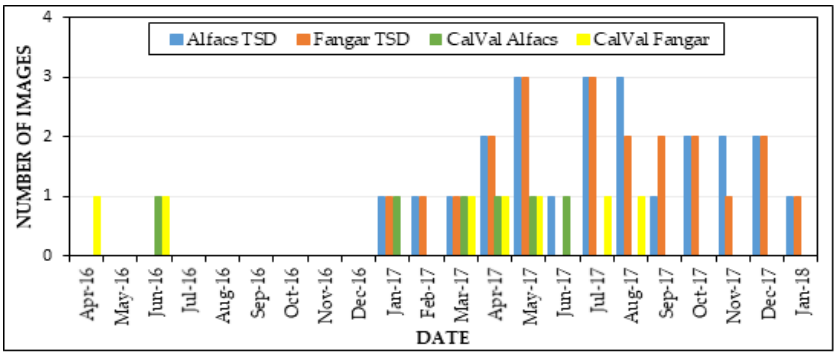

Figure 6. Temporal distribution of S2 images used in this study for calibration and validation and time series development (TSD) at Alfacs and Fangar bays.

2.2.3. Atmospheric Correction: ACOLITE

S2A L1C imagery were atmospherically corrected with ACOLITE processor. It bundles the atmospheric correction algorithms and processing software developed by the Royal Belgian Institute of Natural Sciences (RBINS) for aquatic applications of Landsat (5/7/8) and S2 (A/B) satellite data. The Dark Spectrum Fitting (DSF) (Vanhellemont and Ruddick, 2018), used here, computes the atmospheric path radiance based on multiple targets in the scene or sub-scene, with no a priori dark band, allowing an aerosol correction. ACOLITE includes a sun glint correction, which uses the shortwave infrared (SWIR) bands to estimate a glint signal (Harmel *et al.*, 2018) and to establish the threshold to determine which pixels need to be corrected (0.05 by default). S2A B11 and B12 bands (SWIR at 1604 nm and 2202 nm) were used for sun glint correction. The thresholds were set manually image-by-image after a SWIR analysis that was carried out considering the response of Sentinel 2A B11 over water pixels compared to non-water pixels. For each day and bay, land/water mask and sun-glint correction thresholds were defined, ranging between 0.0215 and 0.1. Therefore, the atmospheric correction procedure output included, for each image, uncorrected (a), partially corrected (b), and fully corrected atmosphere (c and d) reflectance data.

(a)Rhot: top of atmosphere reflectance (TOA) derived from the original input file.

(b)Rhorc: Rayleigh corrected reflectance. This is the Rhot with removed and corrected reflectance for two-way Rayleigh transmittance. An additional pre-processing step was made to avoid high reflectance pixels by fixing a maximum threshold (Rhorc reflectance at 492 nm or 560 nm $\geq$ 0.11) above which pixels were assigned as invalids.

(c)Rrs: remote sensing reflectance (sr^{-1}) for water pixels (Rrs = Rhow/π).

(d)Rhow: surface reflectance for water pixels.

2.2.4. Chlorophyll-a estimation algorithms

Seven different spectral algorithms band-ratio and band-combination based, were applied to each product resulting of ACOLITE processing (Rhot, Rhorc, Rrs and Rhow). Briefly,

BG: The Ratio between Blue and Green spectra uses the reflectance at 490 nm (blue) and 560 nm (green). At 490 nm carotenoids absorb light strongly, while at 560 nm the absorption of all photosynthetic pigments is minimal (*i.e.*, green reflection). This algorithm was initially proposed by (Morel and Prieur, 1977). *R* stands for Rhot, Rhorc, Rrs, or Rhow reflectance.

$$[\text{chl}-a] \propto \frac{R(490)}{R(560)} \quad (1)$$

BR: The Blue–Red ratio is based on the two chl-*a* maximal absorption peaks.

$$[\text{chl}-a] \propto \frac{R(490)}{R(665)} \quad (2)$$

RG: The Green–Red ratio is based on the minimal and maximal absorption peaks of chl-*a*, thus avoiding the use of the blue bands (Gitelson *et al.*, 1986; Gitelson *et al.*, 1986; Oliveira *et al.*, 2016).

$$[\text{chl}-a] \propto \frac{R(665)}{R(560)} \quad (3)$$

NR: The ratio between Red and NIR assumes that the absorption by non-algal particles, yellow substances and the backscattering are insignificant when compared to chl-*a* absorption at red wavelengths - 665 nm - (Lins *et al.*, 2017). Between 700 and 720 nm, the absorption due to water constituents is minimal.

$$[\text{chl}-a] \propto \frac{R(705)}{R(665)} \quad (4)$$

NDCI: The Normal Difference Chlorophyll Index developed by Mishra *et al.* (Mishra and Mishra, 2012) for turbid productive waters uses the information of the reflectance peak centered at 700 nm, which is maximally sensitive to variations in chl-*a* concentration in water. Furthermore, a wide spectral absorption peak between 665 nm and 675 nm is generally associated to the absorption by chl-*a* pigments. The normalization through the NDCI eliminates uncertainties in the estimation of the remote sensing reflectance, seasonal solar azimuth differences, and atmospheric contributions.

$$[\text{chl}-a] \propto \frac{[R(705)-R(665)]}{[R(705)+R(665)]} \quad (5)$$

DO5: Dall'Olmo and Gitelson (2005) presented a three-band model using Red and NIR bands. It assumes that (i) the absorption by coloured dissolved organic matter (CDOM) and total suspended matter (TSM) beyond 700 nm is approximately equal to that at 665–675 nm and the difference between them can be neglected; (ii) total chlorophyll, CDOM, and TSM absorption beyond 730 nm is almost 0; and (iii) backscattering coefficient of chl-*a* is spectrally invariant (Mishra and Mishra, 2012; Dall'Olmo and Gitelson, 2005).

$$[\text{chl}-a] \propto \left[\frac{1}{R(665)} - \frac{1}{R(705)}\right] \times R(740) \quad (6)$$

MCI: The Maximum Chlorophyll Index allows the detection of red tides and aquatic vegetation (Gower *et al.*, 1999). For S2, it uses the band 5 (705 nm), perfectly located to detect high biomass water bodies against the baselines of the bands 4 and 6 (665 and 740 nm). In equation 7, k is the thin cloud correction factor fixed at 1.005 for thin clouds.

$$[\text{chl}-a] \propto R(705) - k \times \left(R(665) + \left(R(740) - R(665)\right) \times \frac{705-665}{740-665}\right) \quad (7)$$

2.2.5. Model Calibration and Validation

S2A (Level 1C and 2A) images and all *in situ* chl-*a* of coinciding days were used for model calibration and validation. In order to reduce the effect of noise from the sensor and the time difference between the image (20 m resolution) and water samples acquisition, the reflectance was averaged over a 3 × 3 pixel-box centered at the *in situ* measurements. However, not all of the nine pixels per *in situ* sampling location could be used as there might be outliers coming from different sources such as bottom contamination, different affection of sun glint and adjacency or infrastructures as rafts or harbor jetties interfering in some pixels. For this reason, a pre-processing step was carried out on each spectral band used and for all atmospheric correction levels. For each day and bay, considering together all *in situ* sampling locations, outliers were detected and removed by Tukey's fences method (Boxplot). The criteria flagged as invalid a pixel if in one of the five spectral bands (see Equations 1–7) the reflectance value was classified as outlier. A second step to clean the remaining outliers was carried out applying the same methodology to each 3 × 3 pixel-box centered at *in situ* sampling sites, individually. To ensure the possibility of using the averaged reflectance of 2–9 pixels, without corrupting the methodology, standard deviation (*SD*) of the average at each sampling location was computed against the number of pixels used for the average.

After outlier deletion, the seven algorithms were computed using the averaged reflectance at each chl-*a* sampling location. Model calibration was done with 70% of the data (with ordinary least of squares fitting, OLS) and the remaining 30% was used for model validation. Models were calibrated and validated in two different ways: (i) using only those samples where *in situ* chl-*a* was measured by the three methodologies (*i.e.*, *in vivo*, FL, SP) and (ii) for each methodology including all the available data. In both cases, model development was carried out considering all possible combinations of ACOLITE-derived imagery together with two different scenarios (individually or both bays together).

Model performance was assessed graphically by plotting observed and predicted values, and efficiency was measured with the Akaike Information Criterion (*AIC*), the Averaged Percentage Difference (*APD*), and the Mean Absolute Error (*MAE*). *AIC* combines fit and parsimony (number of parameters) of models, with the best fitting model having the lowest *AIC*. *MAE* and *APD* were applied following the

criteria of Seegers *et al.* (2018), who suggested that these metrics account better for the accuracy of the models over non-Gaussian distributions by not amplifying outliers and precisely reflecting the error magnitude. Models with the lowest *AIC*, *MAE*, and *APD*, in this order, were considered better. Although the coefficient of determination (*i.e.*, R^2) and Normalized Root Mean Squared Error (*RMSE*) are widely used goodness-of-fit measures, they are not recommended for non-Gaussian distributions (Seegers *et al.*, 2018). Thus, both measures were only included to allow the comparison with previous works.

2.2.6. Time series estimation

The best model was selected to construct chl-*a* time series maps with the available S2A images in 2017. Pixel-stability was assessed by using an unsupervised classification cluster analysis (2 classes) based on the inter-pixel slope of the averaged time series chl-*a* and the coefficient of variation (*CV*; Equation 8) of chl-*a* of the same set of images.

$$CV = \frac{\sigma}{\bar{x}} \tag{8}$$

where σ stands for standard deviation (*SD*) and $\bar{x}$ for the average.

2.2.7. Workflow

The proposed workflow (Figure 7) started with the selection and download of S2A L1C images. The images were processed with ACOLITE after the SWIR analysis, including a resampling of all bands to 20 m, image cropping to the region of interest (Ebro Delta bays), and the atmospheric correction to derive Rhorc, Rrs, and Rhow reflectance (see section 2.2.5). After ACOLITE processing, for the spectral bands of interest, outliers were detected and removed. Then, for each image of the calibration set, the spectral algorithms were computed, and the resulting values were extracted at each chl-*a* sampling location. Models were calibrated and validated with Rhot, Rhorc, Rrs, and Rhow imagery together with ground truth data. The best algorithm and methodology were selected, applied to all the available images in 2017, and the pixel-stability analysis was carried out. Finally, the resulting time series was used to analyze spatiotemporal patterns of chl-*a* (as indicator of phytoplankton biomass dynamics), covering different seasons and the full rice farming cycle.

All statistical analyses were performed with R version 3.5.2; the packages foreign 0.8.71, xlsx 0.6.1, xlsxjars 0.6.1, ncdf 1.16.1, and raster 2.8.19 were used to load external data with different formats. Packages rgdal 1.4.3, spatstat 1.59.0, and maptools 0.9.5 were used to work with geospatial data (create masks, band math calculator, and pixel extraction). Packages FSA 0.8.24, NCStats 0.4.7, nlstools 1.0.2, and minipack.lm 1.2.1 were used to evaluate the model performance (*ROC* curves and associated statistical parameters).

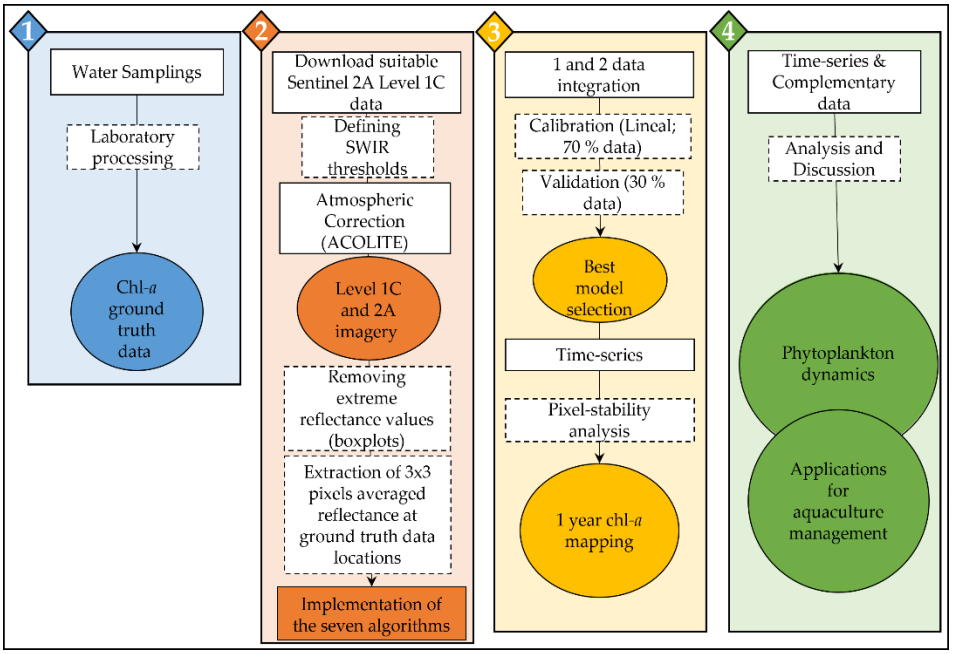

Figure 7. Workflow to derive chl-*a* time series from S2A multispectral imagery (MSI) data at Ebro Delta bays for aquaculture management purposes.

2.3. RESULTS

2.3.1. *In situ* data: chl-*a*

Overall, chlorophyll-*a* concentration varied among seasons and sites, with different spatial distribution patterns in both bays. In Alfacs Bay, chl-*a* showed a spatial gradient trend defined generally by higher concentrations from the central zone with higher concentration values, to the inner area, with minimum chl-*a* concentrations in the shellfish rafts (Figure 4). In Fangar Bay, maximum chl-*a* concentrations were found in the mouth and minimum concentrations in the inner part of the bay, which showed similar values to those in the shellfish rafts. Table 2 summarize chl-*a* results per bay. In general, Alfacs Bay showed higher chl-*a* concentrations.

Among the different laboratory methodologies used to measure chl-*a* concentration, *in vivo* results showed moderate correlation values with both FL (Pearson's $r = 0.60$, $N = 55$, $P < 0.001$) and SP ($r = 0.62$, $N = 43$, $P < 0.001$), while these two methods (FL and SP) were highly correlated ($r = 0.93$, $N = 43$, $P < 0.001$). The average percentage difference (*APD*) between methodologies was 98% between *in vivo* and FL, 56% between *in vivo* and SP and 20% between FL and SP. Surface and integrated water column (sampled in Fangar Bay on both 25 July and 17 August) *in vivo* chl-*a* concentrations were strongly correlated ($r = 0.80$, $N = 40$, $P < 0.001$), with an *APD* of 7.6%.

Table 2. Descriptive statistics of chl-*a* concentration (mg/m^3) per bay and measuring method, during the study period. FL = Fluorometer; SP = Spectrophotometer. *N* is the number of samples, *SD* is the Standard Deviation, and *CV* is the Coefficient of Variation.

Bay	Method	*N*	Min	Max	Median	Mean	*SD*	*CV*
Fangar	*In vivo*	66	0.512	6.553	2.719	2.716	1.497	0.551
	FL	30	0.170	4.992	1.365	1.836	1.278	0.696
	SP	16	0.222	2.597	1.604	1.501	0.732	0.487
Alfacs	*In vivo*	40	0.774	8.880	2.807	3.197	1.867	0.584
	FL	28	1.010	4.750	1.705	2.206	1.131	0.513
	SP	27	1.373	5.596	2.613	2.988	1.291	0.432

2.3.2. Atmospheric Correction and Outlier Removal

The averaged reflectance at the sampling locations for the different atmospheric correction products (*i.e.*, Rhot, Rhorc, Rhow, and Rrs) for each CalVal date and bay (Figure 8), and at each S2A band, showed less reflectance from uncorrected to full corrected levels, this being more pronounced for shorter wavelengths. Fangar Bay showed higher averaged reflectance than Alfacs, when comparing the same day, and for all different Level products.

Averaged reflectance of a 3 × 3–pixel box centered at the *in situ* sampling points was used as the reflectance at each location; however, outlier pixels were removed. After outlier detection, 18 sampling points were completely removed and were not used in the CalVal process. Sixteen of the 18 removed points corresponded to Fangar Bay and were mostly located within the shellfish rafts, the mouth of the bay, and the inner area. Two points were removed from Alfacs Bay, both located in the harbor on 20 June 2016. The final available chl-*a* data are summarized in Table 3. In order to evaluate the impact of outlier pixels on the reflectance estimation, it was assessed the reflectance *SD* relative to the number of valid pixels (2 to 9), at each sampling site, for types of S2A products and all the bands used in algorithm calculation. Pearson's correlation coefficient, in absolute value, ranged between $6.11 \cdot 10^{-03}$ and 0.23, thus, reflectance values were similar, independent of the size of the pixel-box around the sampling point (from 2 to 9), and outliers can be removed without introducing significant errors.

2.3.3. Model Calibration and Validation

All variable combinations resulted in 252 models; chl-*a* methodology (*in vivo*, FL, and SP) × bay (Alfacs, Fangar, and both bays together) × S2A images (Rhot, Rhorc, Rrs and Rhow) × spectral algorithm (BG, BR, RG, NR, NDCI, DO5, MCI). Overall, considering all the possible models, the algorithms performed better when applied to Rhorc images, although Red-to-Green (RG) and, especially MCI, showed less

sensibility to the atmospheric correction and similar results were achieved with Rhot, Rhorc, Rrs, or Rhow reflectance.

Table 3. Summary of *in situ* chl-*a* data set used in the calibration and validation process of the S2 derived data.

Date	Sampling Grid	Bay	Number of Samples per Method		
			in vivo	FL	SP
11 Apr 2016	1	Fangar	5	1	0
20 Jun 2016	1	Alfacs	5	1	0
		Fangar	4	1	0
16 Jan 2017	1	Alfacs	7	1	1
17 Mar 2017	1	Alfacs	7	7	7
		Fangar	4	4	4
6 Apr 2017	1	Alfacs	7	7	7
		Fangar	3	3	3
26 May 2017	2	Alfacs	6	6	6
		Fangar	6	6	6
15 Jun 2017	2	Alfacs	6	6	6
25 Jul 2017	3	Fangar	12	5	0
4 Aug 2017	3	Fangar	16	5	0

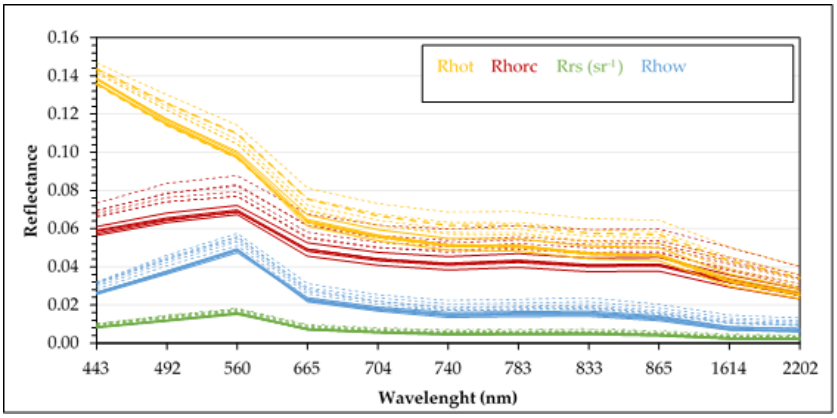

Figure 8. Daily averaged reflectance spectra per bay for each band of S2 L1C and 2A products on Calibration and Validation dates. Alfacs Bay: solid line. Fangar Bay: dashed line.

The best results were obtained combining Rhorc images with spectrophotometer chl-*a* measures (SP). Within the "Rhorc_SP" models, the best performing algorithms were BG (Blue-to-Green ratio) for Alfacs Bay and for both bays together, and the

NDCI (Normal Difference Chlorophyll Index) algorithm returned the best results for Fangar Bay (Table 4). Close results to BG were achieved in Alfacs Bay and both bays together with RG (Red-to-Green) band ratio, while worse results in both cases were obtained with Maximum Chlorophyll Index (MCI). In Fangar Bay, despite differences among the performance of the different algorithms were smaller than in Alfacs Bay, NIR-to-Red (NR) band ratio and MCI performed similar to NDCI, while BG performed worse.

Chlorophyll-*a* was not measured by the three methodologies (*in vivo*, FL, and SP) in all the samples; thus, models had different sample sizes. In order to avoid the influence of sample size on results, the models were also fitted using only those chl-*a* samples measured by the three methodologies. There were not significant changes associated with *N*, but changes in model performance were more related to the range of chl-*a* covered by the samples (*e.g.,* the lower variability of chl-*a* in Fangar Bay).

Table 4. Summary of the best performing models per bay for the calibration dataset. "Algorithm" refers to the spectral algorithm applied to Rhorc images and calibrated with chl-*a* spectrophotometer (SP).

Bay	Algorithm	Min chl-*a*	Max chl-*a*	Intercept	Slope	*N*	*MAE*	*APD*	R^2	AIC
Fangar	NDCI	0.46	2.39	0.56	–12.80	9	0.41	0.27	0.43	17.12
Alfacs	BG	1.83	5.12	13.88	–12.24	18	0.71	3.30	0.61	49.54
Both	BG	1.37	5.60	13.93	–12.50	27	0.63	5.58	0.58	72.17

Different algorithms performed better in Alfacs and Fangar Bay. The low number of available SP data and the good results obtained calibrating and validating the model including both bays together suggest the use of "Rhorc_SP" configuration (Figure 9) until more data are available. Despite BG performance in Fangar Bay being worse than that achieved with other algorithms (*i.e.*, NDCI, NR, and MCI), it was probably due to the lack of variability towards higher concentrations and the weight of few extreme values over a small dataset. In fact, the linear distribution of chl-*a* SP in Fangar fit with the trend of Alfacs (Figure 10). Also, the trend line using data from both bays or using data only from Alfacs Bay was almost equal, denoting that Fangar samples were in agreement with the global trend described (Figure 10). These results support the idea of using both bays together and reinforce the assumptions for applying the same model to both bays.

2.3.4. Chlorophyll-a Timeseries

According to previous results, chl-*a* time series was generated from the Blue-to-Green ratio (BG) model using partially corrected images (Rhorc) for both bays together, and chl-*a* measured by spectrophotometer (SP). Two pre-processing steps were applied to reduce the sources of error on the bottom of Rayleigh corrected

reflectance. First, although images were selected according to cloud absence, in two of them, small areas at the extremes of Alfacs Bay were contaminated by clouds. There, the threshold applied to the Rhorc images removed pixels associated with thick clouds (Figure 11), but the thinnest clouds were not successfully detected, and the ground information was not restored in either case.

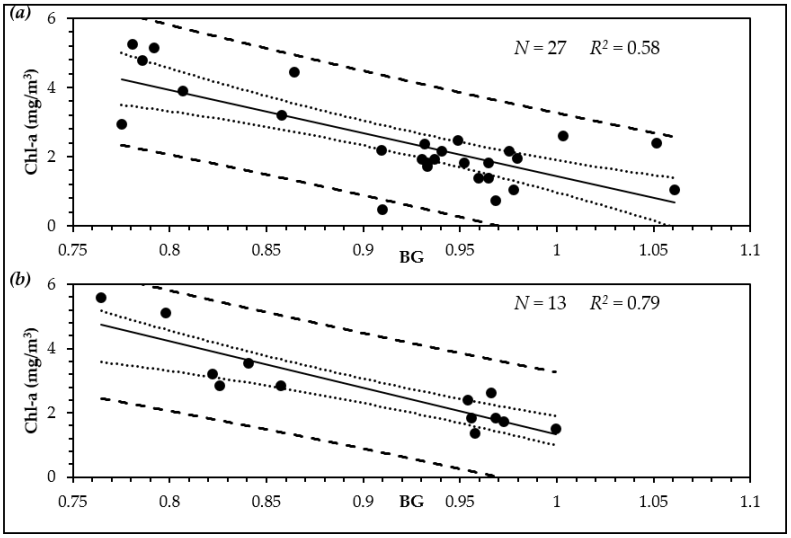

Figure 9. Calibration (a) and Validation (b) results of the Blue-to-Green ratio (BG) algorithm, chl-*a* SP, and both bays together over the set of Rhorc images. The 95% prediction (dashed line) and the 95% confidence interval (dotted line) are also shown.

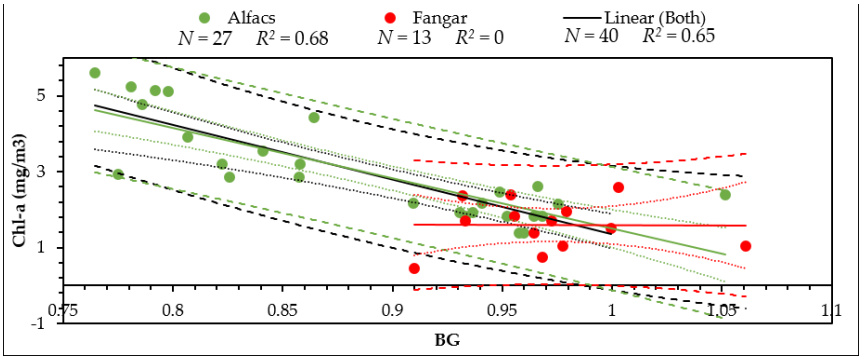

Figure 10. Linear relationship between all available chl-a SP and BG per bay. The 95% prediction (dashed line) and the 95% confidence interval (dotted line) are also shown.

The second pre-processing step consisted on the generation of a mask to avoid areas where BG did not respond only to chl-*a*, but to other sources such as bottom reflectance or macrophytes (Figure 12). The clustering used to make the mask highlighted the boundaries where maximum changes occurred, namely, shallow

waters with bottom or seagrass contribution, hard structures such as rafts, and semi-static objects like the ships in the Alfacs Bay harbor. Finally, before chl-*a* time series estimation, a 20 m buffer (*i.e.*, 1 pixel) was applied, around each raft, created in order to delete mixed border pixels.

Figure 11. Masking Rhorc high reflectance over blue and green bands (threshold = 0.11). Exempla of cloud presence in Alfacs Bay on 22 November.

Both for Fangar and Alfacs bays, one-year chl-*a* time series were processed (Figure 13). Overall, during winter and early spring, higher concentrations of chl-*a* were observed in Alfacs Bay. From April to October, chl-*a* concentrations were comparable between bays; after, in Fangar Bay, chl-*a* concentrations decreased more sharply. Despite the differences in chl-*a* concentration, the general trend was similar in both bays almost all the year, but chl-*a* peaks differed. In Alfacs Bay, chl-*a* peaked during February–April and October–November, achieving maximum concentrations in March. In Fangar Bay, chl-*a* peaked in May and September–October, being the most productive of the year in this last period. Minimum chl-*a* concentrations were found in winter in both bays, January and November for Alfacs and Fangar Bay, respectively. The coefficient of variation (*CV*) of chl-*a* (Figure 14 a-b) along the year showed, in general, higher *CV* in Fangar than in Alfacs Bay. In Fangar, higher variability was observed in the mouth of the bay, associated with higher chl-*a* concentrations, while lower *CV* values were found in the inner area and within the shellfish rafts, where the lowest values of chl-a were found. Conversely, in Alfacs Bay, higher *CV* was observed in the eastern half of the bay, especially in the inner area and the eastern half of the rafts polygon, with a lower average chl-*a* concentration. The harbor area and its surroundings, including the western half of rafts and the mouth of the bay, showed lower values of *CV*, related to higher concentrations of chl-*a*.

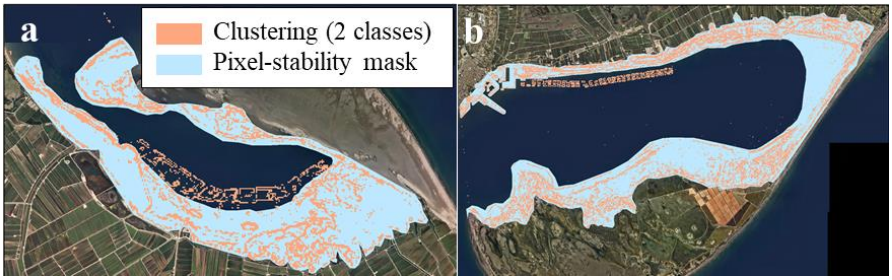

Figure 12. Time series pixel-stability mask. (a) Fangar Bay; (b) Alfacs Bay.

The time series (Figure 13) was revised according to the four different rice-paddies irrigation network scenarios (*i.e.*, Closed channels in winter, semi-closed channels in spring, opened channels in summer, and semi-opened channels in autumn) and aquaculture production. The closure of the discharging channels (closed, semi-closed, and semi-opened) propitiated a more eutrophic environment, reaching higher chl-*a* concentrations than during the opened channels stage, this phenomenon being more evident in Alfacs Bay. During the closed and semi-closed stage (from January to April), chl-*a* tended to increase in both bays, but the increment was much more pronounced and long-lasting in Alfacs. During these months rice paddies are dry and so, the supply of water from the channels is minimum. Regarding the chl-*a* within the shellfish rafts, while Fangar Bay showed similar chl-*a* concentrations inside and outside the rafts (more homogeneous bay), in Alfacs Bay, lower concentrations of chl-*a* were observed inside the rafts' polygon. During the opened channels stage (from April to September), chl-*a* concentration decreased in Alfacs and remained the same in Fangar Bay, compared with the prior period. However, from late July, both bays showed an increase in chl-*a* concentration that lasted until the end of September, when chl-a dropped sharply, achieving values close to 0 mg/m^3 in both bays. The opened channels stage is characterized by high freshwater inputs with the maximum occurring in September–October. Despite shellfish filtering more actively during the warm months, no significant differences in chl-*a* were observed between the rafts and their surroundings in neither of the two bays. Finally, the semi-opened channel's stage (from October to December) started with a strong increase of chl-*a* at both bays in October, which lasted until late November, when chl-*a* concentrations dropped close to 0 at both bays. During December, Alfacs Bay recovered chl-*a* concentrations similar to those of the opened channels stage, but Fangar Bay kept low chl-*a* values. The semi-opened channels stage implies that water is still being discharged in the bay, but contributions decrease with time. Most of the shellfish are harvested during summer, so the bivalve grazing pressure is reduced during the last months of the year. Although similar chl-*a* concentrations were found between the rafts and the rest of the bays, lower values of chl-*a* tended to aggregate in the middle area of the Alfacs rafts' polygon, and the Northern rafts of Fangar Bay.

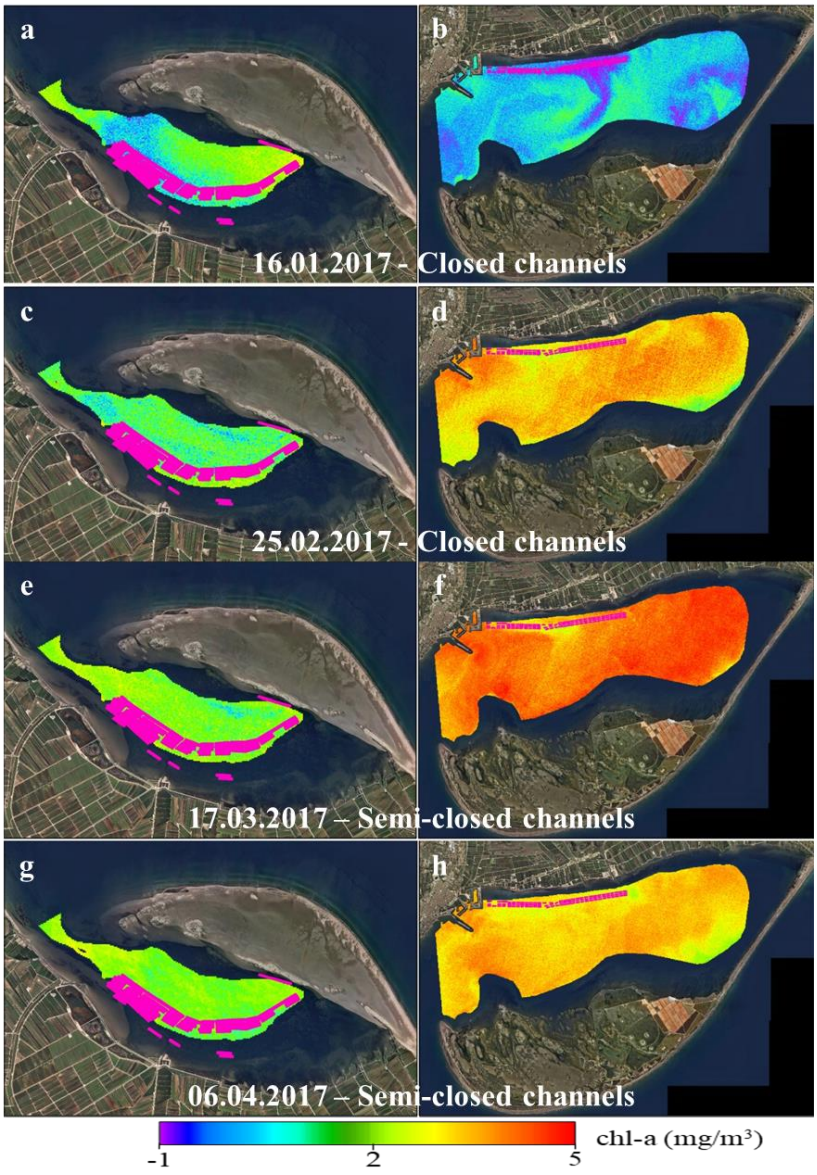
a
b
16.01.2017 - Closed channels
c
d
25.02.2017 - Closed channels
e
f
17.03.2017 – Semi-closed channels
g
h
06.04.2017 – Semi-closed channels
-1
2
5
chl-a (mg/m³)

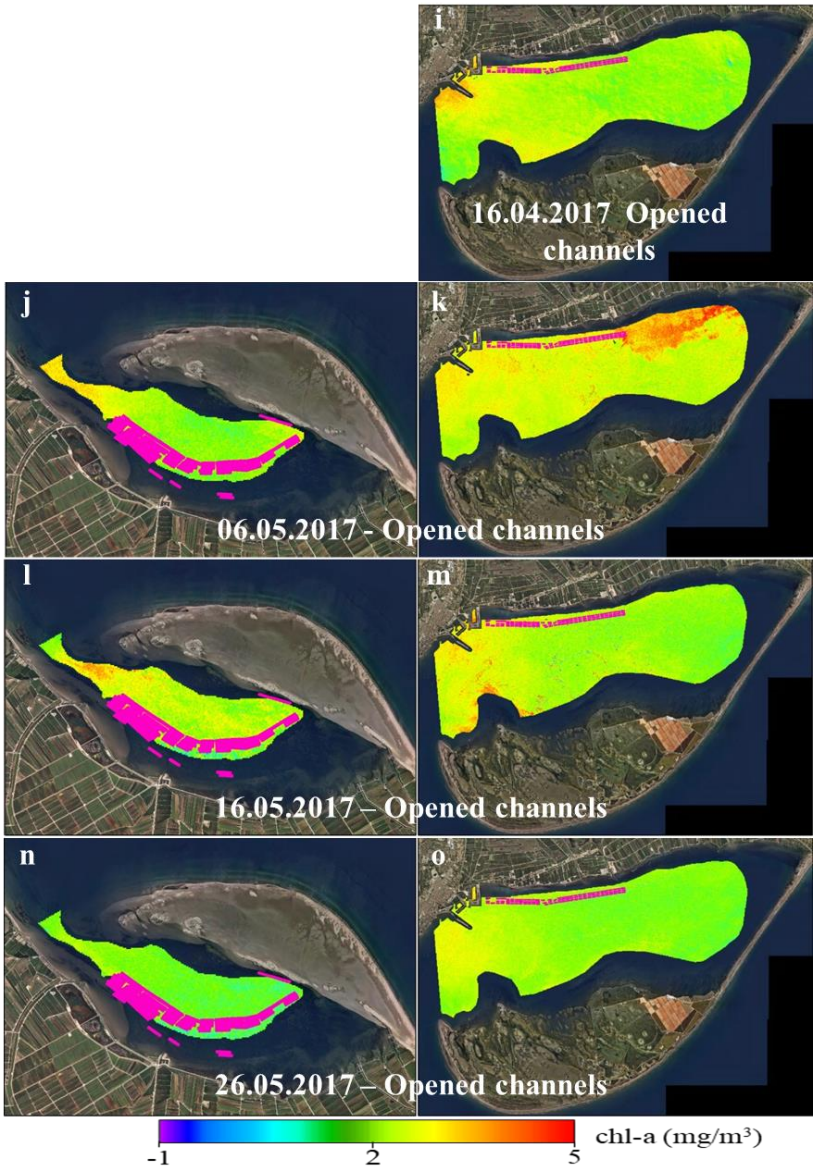
i
16.04.2017 Opened channels
j
k
06.05.2017 - Opened channels
l
m
16.05.2017 – Opened channels
n
o
26.05.2017 – Opened channels
chl-a (mg/m³)
-1
2
5

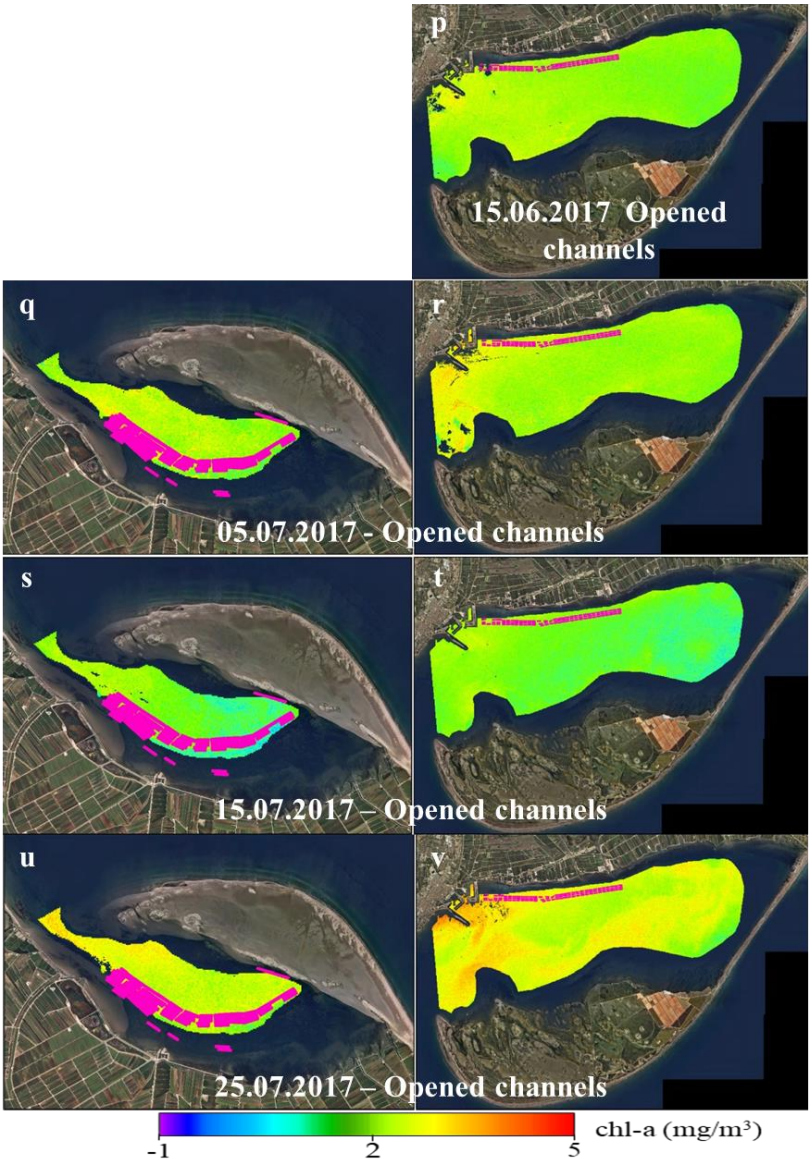
p
15.06.2017 Opened channels
q
r
05.07.2017 - Opened channels
s
t
15.07.2017 – Opened channels
u
v
25.07.2017 – Opened channels
-1
2
5
chl-a (mg/m³)

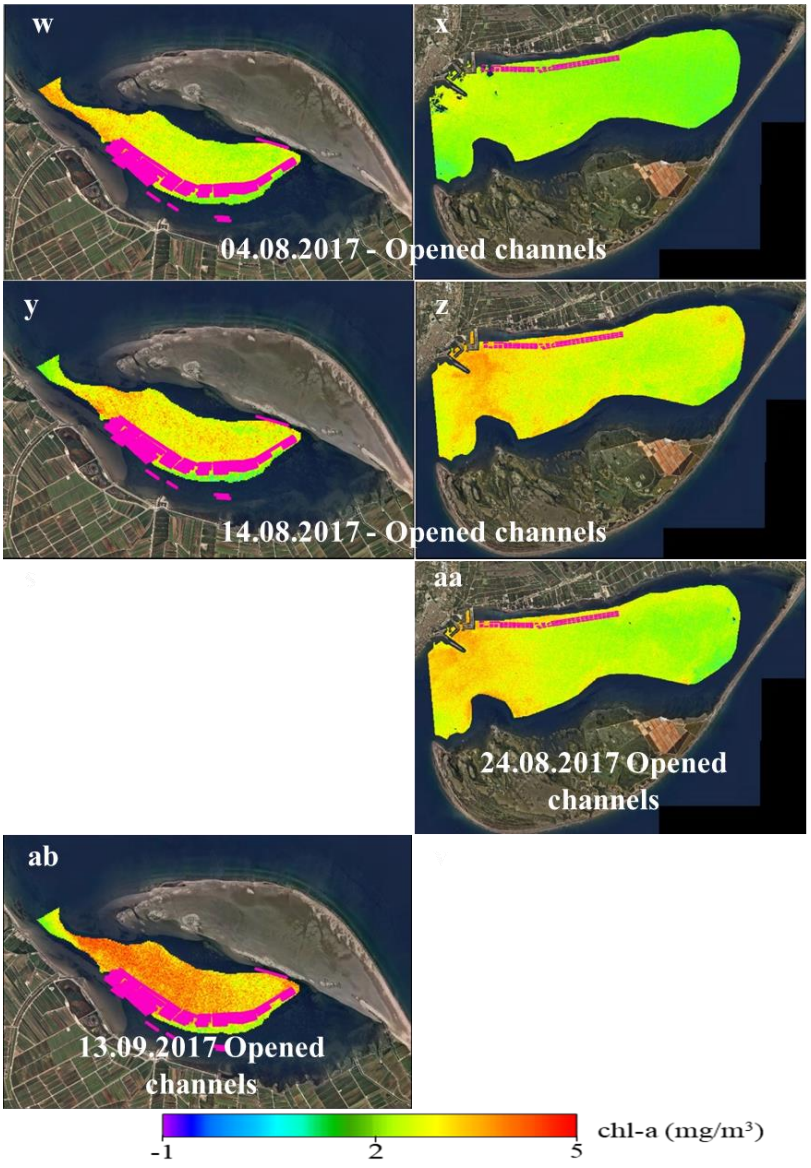
w
x
04.08.2017 - Opened channels
y
z
14.08.2017 - Opened channels
aa
24.08.2017 Opened channels
ab
13.09.2017 Opened channels
chl-a (mg/m³)
-1
2
5

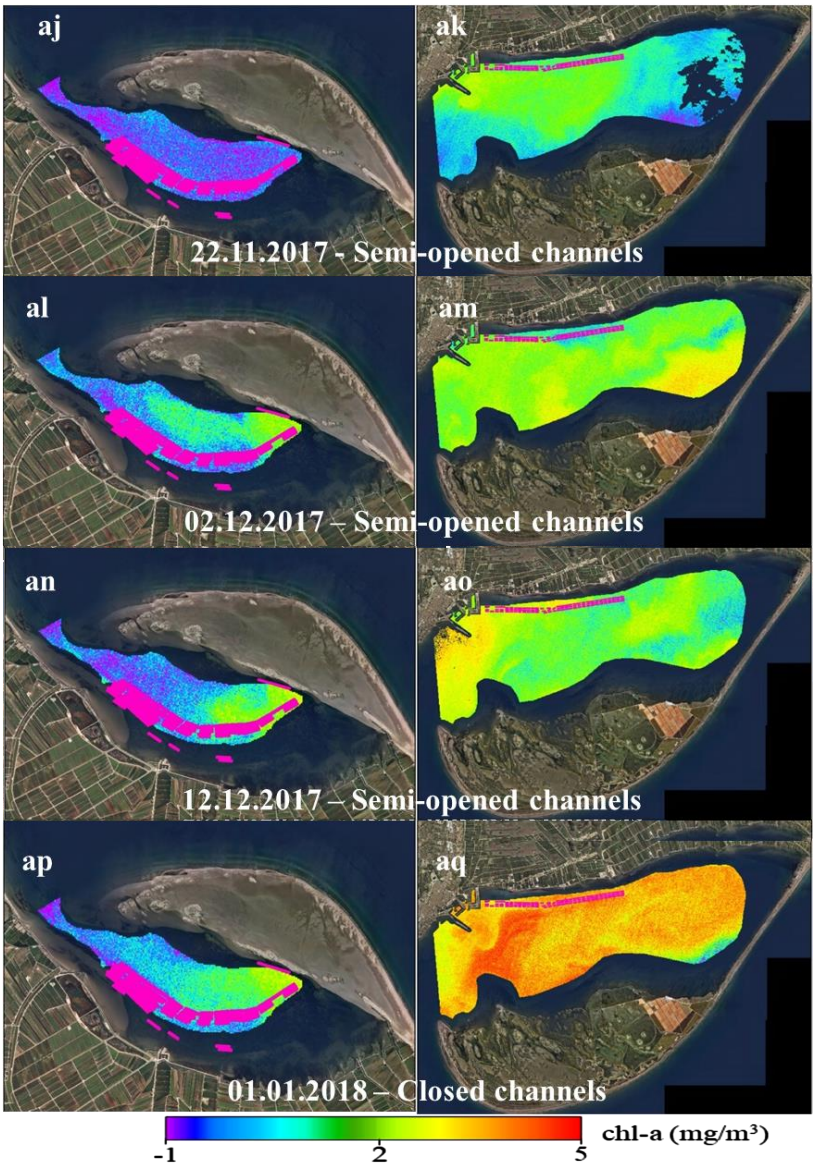

Figure 13. Time series of chl-*a* maps for the year 2017 (a-aq).

2.4. DISCUSSION

2.4.1. *In situ* data: chl-*a*

Three different laboratory methods for chl-*a* quantification from water samples were compared. Chlorophyll-*a* concentration measured by spectrophotometer (SP) after acetone extraction was better correlated with satellite data. The *in vivo* method is only used as a fast qualitative proxy of chl-*a* due to its sensibility to errors with unknown uncertainty (*i.e.*, overestimation due to non-phytoplanktonic contribution), while extracting the pigment with a solvent (*i.e.*, alcohol-based or acetone) and measuring it with the fluorometer or spectrophotometer is the common procedure in remote sensing of chl-*a* (Cannizzaro and Carder, 2006; Gitelson *et al.*, 2008; Gons *et al.*, 2008). Regarding the use of surface or integrated water samples for ground truth chl-*a* quantification, the vertical distribution of the phytoplankton biomass might have a significant impact on the remote sensing signal. In Fangar Bay, significant differences were not found between surface and integrated water column chl-*a* concentrations. This finding is in agreement with Ramón *et al.* (2007) who found homogeneous chl-*a* concentration by depth in 10-month study (1 sample per month) in the same bay. These results suggest the use of an integrated water column chl-*a* for remote sensing model calibration and validation in coastal shallow waters, but further research should include data of both bays under different scenarios to prove the validity of this assumption during the year.

2.4.2. Atmospheric Correction and chl-a Estimation Algorithms

ACOLITE was used for atmospheric correction of Sentinel 2A L1C images using the Dark Spectrum Fitting (DSF) based on the SWIR bands. The results showed that TOA contributed over 50% for all MSI over surface reflectance of water pixels (Rhow). This might be related to non-negligible water reflectance in the SWIR band. According to (Dogliotti and Ruddick, 2011), the invalidity of the SWIR black pixel assumption could lead to an overcorrection of the reflectance (SWIR reflectance for water pixels was up to 10 times larger when solar zenith $< 42^{\circ}$; *i.e.*, spring and summer). In this study, it was not possible to validate the atmospheric correction with field radiometric measurements, but the drop of reflectance of Rhow images compared to Rhot in the blue bands was noticeable. However, a strong reflectance peak was observed in the green part, independent of the level of atmospheric correction applied. Similar results were obtained by Caballero *et al.* (2018b) using ACOLITE without sun glint correction in an estuarine area, and they also found higher water reflectance in all bands in areas with a higher concentration of total suspended matter. In the Ebro Delta, Fangar Bay always showed larger reflectance at all spectrum compared to Alfacs Bay. Fangar is shallower and thus is more susceptible to wind-driven mixing and sediment resuspension. However, the increased reflectance of Fangar Bay might be also related to bottom reflectance or contamination due to adjacency effects. As suggested by other authors (Novoa *et al.*, 2017; Sei, 2015), adjacency effects have a significant impact in coastal waters due to

typical lower reflectance in relation to their neighbourhood surfaces (*i.e.*, sand beaches and rice paddies), increasing the apparent brightness. This effect might be more pronounced in Fangar Bay due to its geomorphological characteristics (smaller, shallower, and more closed).

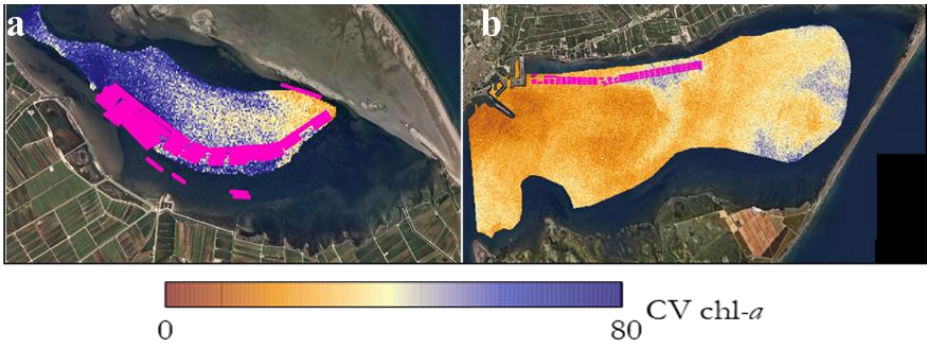

Figure 14. Time series coefficient of variation (*CV*) of chl-*a*. (a) Fangar; (b) Alfacs.

The simplified atmospheric correction procedure, which normalizes the TOA signal for Rayleigh effects, was preferred in favor of a full aerosol atmospheric correction given the large uncertainties associated with water leaving reflectance over turbid waters. Vanhellemont and Ruddick (2018) found a similar performance between the median spectra derived for full atmospheric correction and only Rayleigh correction. Our models showed better performance using Rhorc images instead of Rhow. For both bays together, the best performing algorithm was the BG ratio. Common ocean color algorithms based on the ratio of blue and green bands do not perform well in optically complex coastal waters due to less sensitivity to chl-*a* concentration changes (Gons *et al.*, 2002; Mishra and Mishra, 2012; Le *et al.*, 2013; Oliveira *et al.*, 2016). However, Gons *et al.* (2002) suggested that, in case 2 oligotrophic waters ([chl-*a*] < 4 mg/m^3), the use of blue and green wavelengths is more appropriate. In the present study, averaged chl-*a* concentrations (measured *in situ*) were 1.50 and 2.99 mg/m^3, with maximums of 2.60 and 5.60 mg/m^3, for Fangar and Alfacs Bays, respectively, and the results achieved were in agreement with (Busch, 2013; Gernez *et al.*, 2017). The chl-*a* estimates were reasonably well derived (*MAE* = 0.63 and *APD* < 10%) using the BG ratio.

2.4.3. Model Calibration and Validation

In order to reduce noise and minimize temporal gap effects, ground truth chl-*a* data were averaged over a 3 × 3–pixel box, centered on the sampling point. Despite the averaged reflectance is commonly used, it might be a poor measure of central tendency if the set of pixels used for its calculation contains outliers. Here, outliers were removed before averaging the 3 × 3 pixel box. Although the number of valid pixels differed among locations and dates, the number of valid pixels (between 2 and 9) was not correlated with the mean standard deviation, thus demonstrating the

suitability of the results. After model selection, the BG applied over Rhorc images was preferred and used to make a "pixel-stability mask" to identify and reject those areas where the values obtained with the integration of the remote sensing and the model were not responding to the changes of chl-*a*. Based on *k*-means clustering, the applied methodology allowed us to distinguish the boundaries where maximum changes occurred, thus defining the edges for the delimitation of the mask. In Alfacs Bay, better results were achieved, able to differentiate each raft individually (rafts more separated than in Fangar) and masking the shallow waters (confined only to the margins of the bay).

The applied model was based on algorithms specifically tuned for Alfacs and Fangar bays. Despite the good results achieved for the CalVal dates, the suitability of the model depends on the ratio between the range of remote sensing and the range of the available ground data and its representativeness along with different seasons or scenarios. In our study, not many samples were available, but their spatial distribution covered a wide range of in-day scenarios at each bay. However, most of the samples for CalVal purposes included only the seasons of summer and spring so the application of the models over winter and autumn was subjected to higher uncertainty. Indeed, the range of chl-*a* measured *in situ* included low number of samples with concentrations under 1 mg/m^3, which are highly representative of the winter season. This fact coupled with the linearity of the developed models, increases the error related to low chl-*a* concentrations, tending more rapidly to negative numbers (*e.g.,* Figure 13 b).

2.4.4. Spatiotemporal chl-*a* Dynamics

The time series of chl-*a* covered all year 2017, including the different channel stages at both Fangar and Alfacs bays. Overall, the temperature increased from winter (Tmean ~ 14.4 °C) to summer (Tmean ~ 27.7 °C), and in autumn, the temperature (Tmean ~ 22.5 °C) was similar, even higher, than in spring (Tmean ~ 20.1 °C). The most frequent winds during the year came from the NW sector, predominantly in the morning, with a strong influence of southern winds (spring and summer), switching to SSE (winter and summer) and to SSW (spring and autumn) from noon onward. Within the dates included in this study, the highest intensities were registered in March and December, both related to directions of 300–360° (NW and NNW). The rainiest month of the year was January (72.4 mm in seven days), followed by March (36.5 mm in 14 days), and within the days included in the time series, it rained on 4 August between 4:30 and 5:00 am (accumulated precipitation of 0.1 mm) and on 23 September from 4:30–6:30 am (accumulated precipitation of 0.3 mm).

Regarding the variability of chl-*a* inside each bay (in terms of *CV*), Fangar Bay showed higher heterogeneity along time, but more homogeneity along space than Alfacs Bay. Fangar Bay is smaller and shallower, which makes it more susceptible to environmental variations, making the changes faster and affecting more of the bay's

area. In this study, it has been observed that in Fangar maximum variations were related to more energetic areas with more chl-*a* (mouth), while in Alfacs, higher variabilities were associated with less energetic areas where chl-*a* dynamics depend largely on the wind-driven mixing (inner NE area). These findings are related to the renewal time of the bays (higher in Alfacs) and linked to the capacity for developing larger phytoplankton populations (higher chl-*a* concentrations). In this sense, Alfacs Bay characteristics (larger and deeper bay more perpendicular to NW and N winds with higher water residence times) allow nutrients to sink and get stored in the sediment of the bay and, at the same time, allow them to be released and suspended during more time (increased nutrient availability for phytoplankton). Conversely, quicker changes in Fangar Bay make chl-*a* being diluted faster by the Mediterranean water inputs (less productive waters).

In relation to chl-*a* concentrations, besides the seasonal temperature-driven dynamics, wind was the environmental parameter more related to the maximum variations of chl-*a* inside the bays. In terms of temporal dynamics, overall, chl-*a* increased more with prolonged NW and N strong winds episodes occurred on 17 March both bays (Figure 13 e-f), 25 July both bays (Figure 13 u-v), 13 September Fangar Bay (Figure 13 a-b), 23 October both bays (Figure 13 ag-ah), and 12 November Alfacs Bay (Figure 13 ai). The highest accumulations of chl-*a* at both bays occurred on March (Figure 13 e-f), October (Figure 13 ae-ah), and early November (Figure 13 ai), when channels were closed or semi-closed. Conversely, weaker winds from southern components were related to decreases in chl-*a* concentrations as happened on 15 July both bays (Figure 13 s-t), 23 September both bays (Figure 13 ac-ad), and 22 November both bays (Figure 13 aj-ak). The reduction of chl-*a* concentration in both bays was enhanced after rainy events as those of 23 September (Figure 13 ac-ad) and 22 November (Figure 13 aj-ak). These results suggest that wind plays a major role in the nutrient load of the water column. On one hand, mixing the water re-suspending the sediment, thus making the nutrients available (wind-induced turbulence). On the other, enhancing water renewal which increases the flushing cells ratio and does not allow time enough for the development of large phytoplankton populations (Llebot *et al.*, 2011) - wind-enhanced circulation -. Therefore, higher chl-*a* concentrations are expected to occur when the estuarine circulation is weakened and the turbulence increases. This effect might be enhanced at the end or after drainage of the irrigation channels stage (August–November) which increases the nutrients stored in the bays. In the time series presented in this study, this occurred in August at both bays (Figure 13 w-aa) and 23 October at both bays (Figure 13 ag-ah), especially when winds blow from land (NW and N). In general, the observed trend was in agreement with previous studies (Llebot *et al.*, 2011), which found high chl-*a* concentrations in October in Alfacs Bay and from July to November in Fangar Bay.

In terms of spatial dynamics (in-day scenarios), high chl-*a* concentrations were related more frequently to the mouth area of both bays. There, the exchange with the Mediterranean Sea leads to a more unstable scenario in which, despite water

renewal might be higher, increased turbulence favors phytoplankton growth prevailing over the wind's regime. High concentrations in the mouth of Fangar Bay were related with more chl-*a* within the central channel of the bay (northern face of rafts), while in Alfacs Bay there was not so clear relation. In this bay, the highest chl-*a* concentrations were also found in the inner area (NE), which is more retentive and concentrates more nutrients (Artigas *et al.*, 2014).

Because of all the aforementioned, shellfish aquaculture in the bays benefits from increased chl-*a* concentrations compared to the open sea. However, the retentiveness that characterizes the bays becomes a double-edged sword due to the high temperatures that water reaches during summer (>30 °C), which negatively affects the feeding rate of shellfish, becoming lethal when temperatures above 28 °C are maintained for days (Ramón *et al.*, 2007). In order to develop a feasible method for aquaculture management by means of remote sensing monitoring, temperature must be included as one of the main factors, together with chl-*a*, controlling shellfish growth and conditioning the sustainability of the cultures.

In this work, the first results have been presented, and measures to enhance aquaculture can be proposed. However, the feasibility of implementing them is subjected to the availability of bio-geophysical models considering longer time series, which would allow making a more integrated and robust approach. Including more data (parameters considered, increased number of data, wider dynamic range) and integrating them into the models would lead to carrying out studies in line with (Grant *et al.*, 2009; Gernez *et al.*, 2017), which coupled remote sensed chl-*a* with other environmental parameters to establish shellfish farming suitability index, to determinate the load capacity of the bays, and to rezoning the rafts' locations.

2.5. CONCLUSION

High spatial resolution (10–60 m) Sentinel-2 (S2) imagery offers a new opportunity for remote sensing of water quality in small coastal geographic areas. In the Ebro Delta bays, the main Spanish Mediterranean shellfish production site, S2 imagery has demonstrated the potential to become a suitable tool for resolving the fast dynamics of phytoplankton in the area (in terms of chl-*a* concentration), within short space and time-frames. The monitoring using satellite remote sensing improves the standard *in situ* sampling-based methodology, allowing moving from punctual to full coverage, thus enabling holistic analyses (time series) to enhance coastal management (*e.g.,* aquaculture).

After testing different levels of atmospheric correction, it is not feasible to use uncorrected atmosphere images (TOA), but the full correction of the atmosphere is still highly uncertain. The results obtained suggest the use of Rayleight corrected S2 imagery together with a simple Blue-to-Green ratio for chl-*a* estimation until a full correction is completely solved/validated. With this configuration, credible chl-*a* maps of the bays were derived, including the preservation of some information within the rafts polygons.

Despite the aforementioned success, remote sensing of small complex coastal geographic areas still faces several challenges. The main limitations found in this study were (i) full atmospheric correction accounting for aerosol, Rayleigh, sun glint, and adjacency effects and (ii) uncertainties associated with shallower areas contaminated by bottom reflectance, contributions of seagrasses to the total chl-*a* concentration, and validity of the results out the range of derivation of the model (location of ground truth data, wider range of chl-a concentrations, and seasonality). Further research should be directed to solve these shortcomings by improving the atmospheric correction and gathering more field data covering a higher number of scenarios. With these, a sensitivity test should be conducted for algorithm bounding, and, ideally, specific tunned models should be developed for each scenario (bay/season/water optical properties).

Chapter 3

IMPACT OF AGRICULTURE RUNOFF ON COASTAL WATERS

MACROPHYTE'S DYNAMICS AS BIOINDICATOR OF RICE FARMING DISTURBANCE

An edited version of:

Soriano-González, J., Angelats, E., Martínez-Eixarch, M., Alcaraz, C. Rice farming and macrophyte dynamics monitoring through Sentinel-2 MSI as a proxy of disturbance of agricultural practices over an enclosed bay. *Proceedings of FIG Working Week 2020, 10-14 May. 2020.*

One of the main limitations in mapping phytoplankton biomass in coastal areas using multispectral satellite data is related to the presence of macrophytes in shallow waters. The different spectral indices applied in Chapter 2 showed that macrophytes overlap phytoplankton in terms of chl-*a* spectral response, thus leading to an overestimation and uncertainty in the retrieval of phytoplankton biomass in presence of macrophytes. In this chapter, a methodology focused on the classification of shallow seabed cover (*i.e.* macrophyte presence) is implemented in Alfacs Bay. Using a supervised machine learning classification approach, trained with a small set of *in situ* data and a subset of S2 spectral bands, a time series of seabed cover maps (*i.e.*, macroalgae and seagrass) is presented, and the first insights on macrophytes dynamics are shown. In addition, the response of macrophytes in relation to rice crop dynamics is explored. The results highlight the potential for the assessment of agriculture impact on coastal processes through biological proxies derived from S2.

3.1. INTRODUCTION

Coastal regions are highly dynamic and productive ecosystems with high ecological and economical value. They are subjected to considerable anthropogenic pressures such as urban and industrial development, pollution, tourism, aquaculture, and agriculture (Ramírez-Pérez *et al.*, 2017). Hence, to ensure their conservation, sustainable development, and the protection of their resources, it is necessary to implement Integrated Coastal Management (ICM) programs (European Comission, 2002). Agriculture is a good example of a system not only with economic interests but also with ecological benefits and social elements, although these components are not generally considered together (Fulton 1993). For instance, the impacts of agriculture on aquatic ecosystems include both direct and indirect effects. Direct effects include habitat loss due to channelization and wetlands conversion, and indirect effects involve water quality (*e.g.,* salinity and temperature) and habitat impacts of sediment, nutrients, and other pollutants in agricultural runoff, as well as hydrologic alteration (*i.e.,* volume and timing). Thus, leading to changes in aquatic habitats, nutrient cycle, oxygen availability, and faunal composition (Blann *et al.*, 2009). Understanding these relations and determining the underlying mechanisms is essential information for integrated management planning (Fabbri, 1998). However, because of the range of potential interactions and effects with and on the environment, it is necessary to use a proxy for measuring the overall impact. In this sense, within the macrophyte community, seagrass composition, distribution and abundance are often used as a measure of ecosystem health and functioning, although they are often not considered in management decisions (Nordlund *et al.*, 2016). Seagrasses are marine flowering plants forming extensive meadows in shallow coastal waters by providing many important ecosystem services such as coastal protection, nursery habitats, carbon sequestration, and sediment trapping and stabilization (Hemminga and Duarte, 2000; Green and Short, 2003). The location of most seagrass ecosystems (*i.e.,* coastal shallow habitats) expose them to both

terrestrial and marine-based threats and could serve as a sentinel community for agriculture impacts (Knudby and Nordlund, 2011).

In the Ebro Delta the monitoring of rice crop and macrophyte community (*i.e.,* seagrass and macroalgae), may provide useful information on the interaction between systems and support both environmentally and economically responsible decision-making by policy-makers. Because of the spatiotemporal variability and coverage of both ecosystems, remote sensing supposes an improvement of conventional monitoring programs by reducing cost, increasing the frequency of data acquisition, and covering the whole system (Dekker *et al.*, 2006; Petus *et al.*, 2014). Multispectral satellites including the visible (VIS) and NIR regions of the spectrum allow monitoring of land and aquatic vegetation (Van Niel and McVicar, 2004; Hossain *et al.*, 2015). From this perspective, Sentinel-2 Multispectral imager (S2-MSI) is a suitable tool for monitoring the spatiotemporal dynamics of the whole system. The spectral indexes most commonly used for assessing rice crops are the Normalized Difference Vegetation Index (NDVI), based on photosynthetic activity (Huete *et al.*, 2002), and the Normalized Difference Water Index (NDWI), which combined with NDVI is used to detect harvest period and hydroperiod (Tornos *et al.*, 2015). Remote mapping of macrophytes includes the use of vegetation indexes based on green, red and/or NIR spectral bands, in addition to traditional classification procedures based on fieldwork sampling (Gullström *et al.*, 2006; Knudby and Nordlund, 2011; Pu *et al.*, 2012). Thus, the main objectives of this study were to analyze rice crop, seagrass, and macroalgae spatiotemporal dynamics by using S2-MSI imagery, to assess the potential relationships between them, and to discuss the usefulness of S2-MSI imagery for coastal monitoring.

3.2. MATERIALS AND METHODS

3.2.1. Study Area

The study area is centered in Alfacs Bay (Figure 15), which receives the freshwater inputs from the southern delta irrigation network.

Inland, rice is grown from late April to September and left fallow during the rest of the year (Figure 16). In the growing season, water management consists of permanent flooding from sowing time (late April-early May) to two weeks before harvest (September). During the vegetative and early reproductive stages, short periods of drainage can take place as a requirement for the application of herbicides. After harvest, fields are re-inundated for the incorporation of rice straw into the soil. Thereafter fields are either flooded (from October to December) or left to progressively drain, according to the farmers' preferences. From January to March rice fields are left dry for soil labour operations (harrowing and fertilizer application) and re-flooded in Mid-April, at the beginning of the next cultivation period. Standard mineral fertilization is applied with average N doses ranging from 170 to 200 kg N· ha^{-1}. Consequently, Alfacs Bay receives the water drained from *ca.* 115 km^2 of

cultivated rice fields from April to late December (Tornos *et al.*, 2015; Martínez-Eixarch *et al.*, 2018).

As seen in previous chapters, Alfacs Bay ecology and hydrology are mediated by freshwater, nutrient and organic matter inputs from the irrigation network. Irrigation inputs impose a double layer flow, like a typical estuarine circulation pattern (Cerralbo *et al.*, 2019). Macrophyte communities, mainly dominated by *Cymodocea nodosa* (seagrass) and *Caulerpa prolifera* (macroalgae), are distributed in shallow areas (0 – 2 m depth) along the inner shoreline (Pérez and Camp, 1986; Mascaró *et al.*, 2014). Bottom in the northern shore is silty and it is highly influenced by nutrient and organic matter inputs from rice crop discharges. The southern shore is sandy, and it is influenced by marine waters from the open sea (Sanmartí *et al.*, 2018) and, consequently, the zone is oligotrophic, similar to Mediterranean waters.

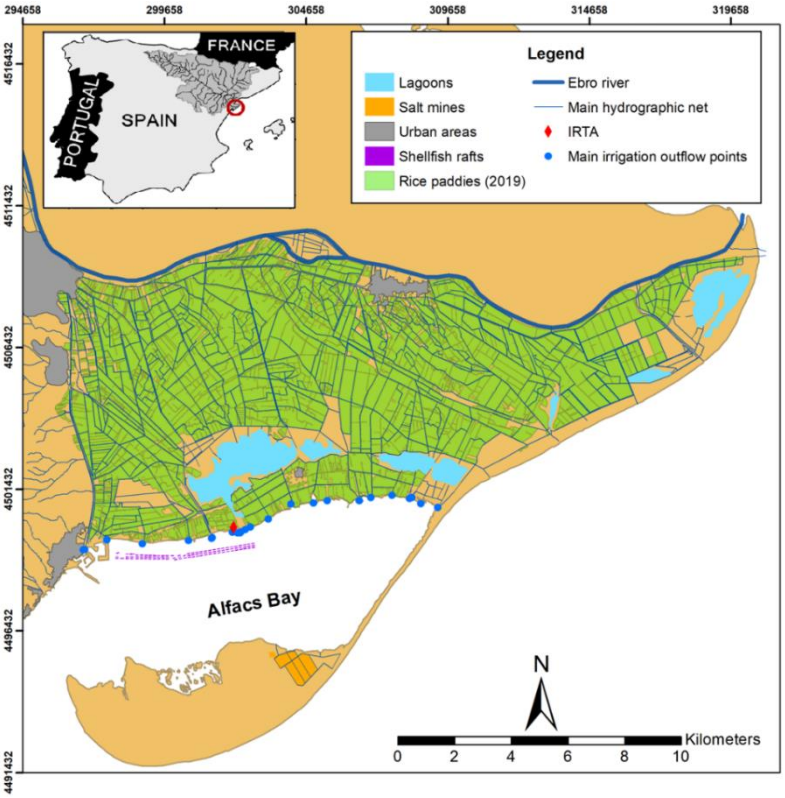

Figure 15. Southern Ebro delta plain and Alfacs bay (NW Mediterranean, Spain).

3.2.2. Sentinel-2 Data

Different data sets were used for analyzing rice crop variation and macrophyte communities (Figure 17). A set of 621 S2 (A and B) L2A images (*i.e.,* cloud cover < 30 %) were used as input in Google Earth Engine for monitoring rice paddies. Google Earth Engine (GEE) is a cloud-based platform, which can be used to

execute large-scale and long-term geospatial analysis (Gorelick *et al.*, 2017). GEE allows direct access to different levels of S2-MSI images, the possibility of filtering satellite imagery (*e.g.,* region of interest, date, cloud cover), and cloud computing band maths generating spectral indexes maps. The level 2A (L2A) official products available on the Copernicus Open Access Hub provide atmospherically corrected images applying Sen2cor processor (Müller-Wilm, 2016). In addition, a set of 56 S2 (A and B) L1C images (*i.e.,* not cloud covered) were downloaded from Copernicus Open Access Hub (https://scihub.copernicus.eu/) and atmospherically corrected with POLYMER v4.12. The polynomial-based algorithm applied to MERIS (POLYMER), applicable to S2-MSI, is an atmospheric correction algorithm specifically designed for processing of oceanic waters with and without the presence of sun-glint (Steinmetz *et al.*, 2011) outputting water surface reflectance images, resampled to 20 m. Note that for rice paddies monitoring, images from different orbits were used, while for macrophytes classification only orbit 51 images were selected (differences in number of images; Figure 17).

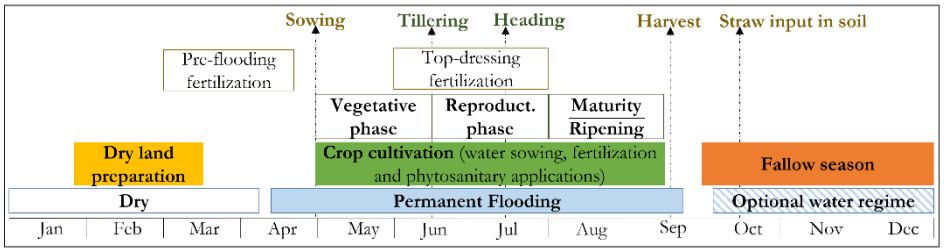

Figure 16. Rice farming calendar in the Ebro Delta. Adapted from (Martínez-Eixarch et al., 2018).

3.2.3. Reference Data

Two sources of ground truth data were used in this study. Rice farming practices and water management including rice sowing, fertilization, and harvesting, were obtained from farmers. Macrophyte field data were gathered from two field campaigns (23.05.19 and 27.12.19) carried out within a time-window of 3 and 0 days with respect to the satellite pass. This data consisted in a set of 52 points (locations within Alfacs Bay), located with Global Navigation Satellite System (GNSS) receiver, where seabed typology was characterized within polygons accounting for five different categories (turbid, seagrass at high and low densities, algae and 'deep' water). It is important to note that there was no differentiation between epiphyted and epiphyte-free macrophyte meadows.

3.2.4. Monitoring of Rice paddies

Four spectral indexes were computed, the Normalized Difference Vegetation Index (NDVI; eq.9) and three different Normalized Difference Water Indexes (NDWI1, NDWI2, and NDWI3; eq.10-12) were computed. Monthly averaged spectral indexes

were calculated with GEE (Figure 17). The Resulting products were 96 images (2 years × 12 months × 4 spectral indexes) at 20 m spatial resolution.

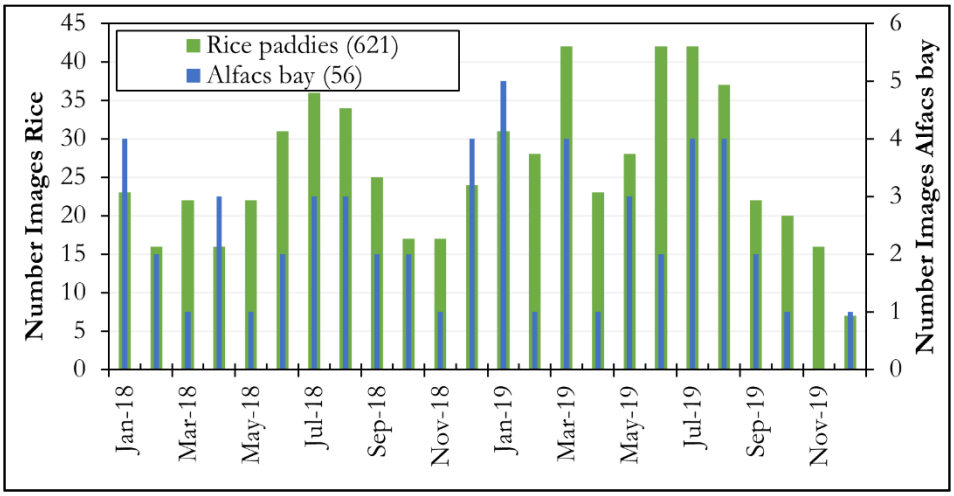

Figure 17. Temporal distribution of S2-MSI images used in this study for rice paddies (green) and macrophytes (blue) time series development.

$$NDVI = \frac{(R842 - R665)}{(R842 + R665)} \quad (9)$$

$$NDWI1 = \frac{(R842 - R1600)}{(R842 + R1600)} \quad (10)$$

$$NDWI2 = \frac{(R842 - R2200)}{(R842 + R2200)} \quad (11)$$

$$NDWI3 = \frac{(R560 - R842)}{(R560 + R842)} \quad (12)$$

NDVI is a good indicator of vegetation growth and has been widely used to assess phenological information (Wang *et al.*, 2012) such as the heading date, and it is also related with culture hydroperiod (Tornos *et al.*, 2015). NDWI is sensitive to leaf water content and soil moisture, describing surfaces of water and vegetation with water content or land of scarce humidity areas. Thus, NDWI may help to define harvest date and to assess changes in flooding stages (Tornos *et al.*, 2015). NDWI maximizes the vegetation reflectance and minimizes the reflectance of water. The common form of NDWI (here, NDWI3) uses NIR bands as the longest, but in this study, SWIR bands were used too to exaggerate the response of the spectral index in flood-based agriculture. Modified NDWI using SWIR bands (here, NDWI1 and NDWI2) are known as Land Surface Water Index (Xiao *et al.*, 2005). The summarized workflow is presented in figure 18.

3.2.5. Macrophytes' monitoring

After atmospheric correction was conducted with POLYMER, images of water reflectance at 20 m spatial resolution were processed in R 3.6 and QGIS 3.4. The processing followed five main steps. (i) the building of a merged composite of bands B3 (560 nm), B4 (665, nm) and B7 (783 nm); (ii) the computation of green NDVI (GNDVI; eq. 13); (iii) the supervised classification using ground truth data for Support Vector Machine technic (SVM); (iv) time series of seabed type; and (v) monthly averaged seabed-class coverage per bay shore (northern and southern).

The GNDVI is related to the leaf area index (Yang and Yang, 2009) and due to the use of the NIR band (eq. 13) it is very sensible to bottom reflectance. Thus, GNDVI has been used to differentiate shallow waters with a higher probability to harbour macrophytes than deep waters.

$$GNDVI = \frac{(R842 - R560)}{(R842 + R560)} \quad (13)$$

Bands B3, B4, and B7 include wavelengths from the green to the NIR edges, which are sensitive to seagrass coverage and biomass. These were merged into a single composite as the main input for seabed-type classification. Support Vector Machine (SVM) was used as the classification method of the seabed cover. SVM is implemented with Orfeo ToolBox (Grizonnet *et al.*, 2017) in QGIS. SVM is based on a supervised machine learning algorithm that uses a linear model for data classification. The algorithm creates a hyperplane that separates data into classes. The data used as input for the SVM consisted in the polygons for which seabed-type was defined (truth data) and the related pre-processed and merged composites of S2-MSI images (23/05/19 and 27/12/19). The ratio of training and validation polygons was set to 50 %, and kernel type model was selected because of the non-linearity of the data. Finally, we obtained an image of classified seabed accounting for the 5 classes defined (*i.e.,* Seagrass high and low density, algae, water, and turbid environments) per date. The summarized workflow is presented in Figure 18.

3.2.6. Coupling of rice paddies development and seabed-cover

In order to simplify the analysis of the results, monthly data of rice paddies stages and macrophyte coverage were used. For rice paddies, the similarity of the curves described by each index at each pixel was checked with a *k*-means clustering. Finally, spectral indexes were averaged per pixel within each category and month. Regarding seagrass dynamics, the area of the 5 different classes (in percentage) was computed for each date and then monthly averaged. Three months (March 2018, November 2018, and April 2018) were not included in the analyses because of the high water turbidity and the uncertainty associated. Finally, spatiotemporal trends of spectral index of rice paddies and seabed-type and coverage were coupled. The summarized workflow of both land and water monitoring is presented in Figure 18.

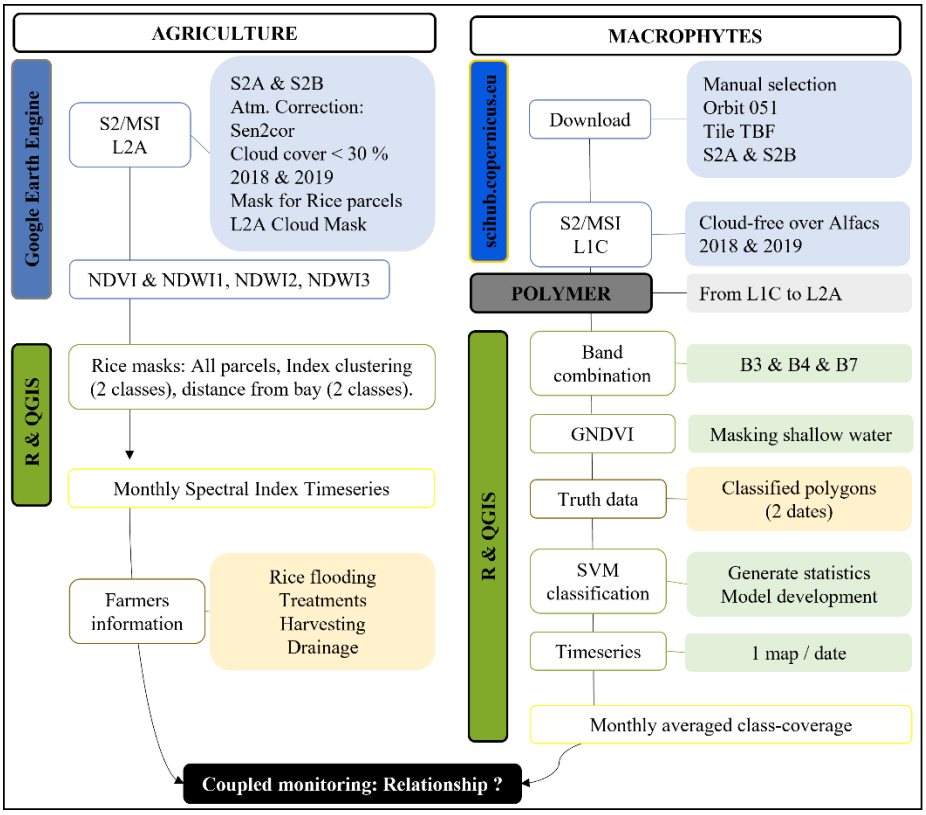

Figure 18. Workflow chart to assess induced-agricultural disturbance over macrophyte communities in Alfacs Bay.

3.3. RESULTS

3.3.1. Water management and crop phenology

All the considered spectral indexes (*i.e.,* NDVI and NDWs) did not show significant differences among the five categories identified in the cluster analysis (Figure 19).

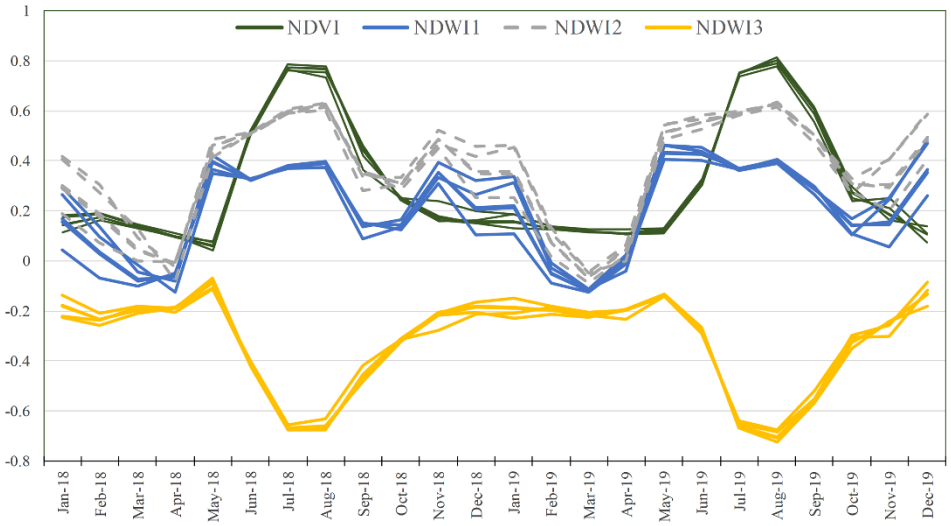

Figure 19. Monthly average of the spectral index for the 5 different clusters.

Land surface water indexes (NDWI1 and NDWI2) were more variable, especially in autumn and winter (October-January), but differences were not so large. Both NDWI1 and NDWI2 showed a similar pattern, but NDWI3 presented a different pattern completely opposite to NDVI. Thus, according to NDVI and NDWI1 temporal patterns, different key farming stages were identified regarding hydroperiod (farming practices) and crop phenology (rice growth). Consequently, flooding, drying, heading, and harvest dates could be properly identified (Figure 20) by following the scheme in Table 5. Despite similar trends in NDVI and NDWI1 in 2018 and 2019, some differences were observed between years. For instance, in 2018 changes in both NDVI and NDWI1 occurred faster (sharper shapes) than in 2019, thus, in 2018, the first flooding and harvesting were finished in one month compared to the two months observed in 2019. In addition, when comparing both annual cycles, a delay of one month in heading date (July 2018 vs August 2019) was observed.

Table 5. Agricultural practices, crop stage and hydroperiod detected by using NDVI and NDWI1 of rice paddies in southern Ebro Delta along single year.

	NDVI	NDWI1
Absolute Maximum	Heading date	1st Flooding
Absolute Minimum	1st Flooding	Dry fields
Relative minimum I	-	End of Flooding - Harvest

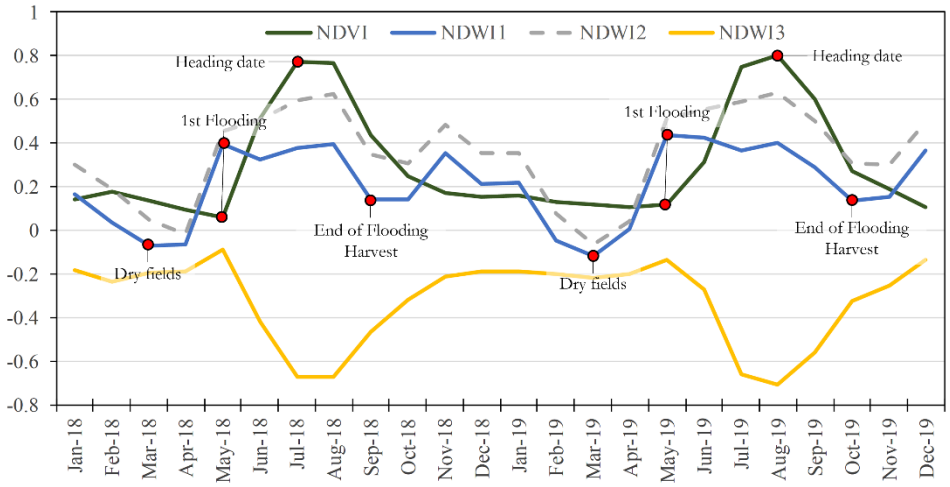

Figure 20. Rice spectral index monthly averaged within whole study area (left axis). Farming practices derived from scheme in Table 5. Macrophytes coverage at the whole bay (right axis).

3.3.2. Classification of seabed cover

Overall, macrophyte cover showed a seasonal pattern in both northern and southern shores, increasing their surface area during warm months (August-October) and decreasing during cold periods (December-February). Macrophyte coverage ranged between *ca.* 30 and 80 % of the shallow area along the sampling period (years 2018 and 2019), with higher coverage in 2019.

Macrophyte cover also showed significant differences between shores (Figure 21). The northern shore was dominated by green macroalgae, with higher coverage in summer (from June to August), and minimum in winter (December and January), and the peak in seagrass coverage occurred in September-October, following the maximum in macroalgae. However, seagrass cover was higher and dominated the southern shore of Alfacs Bay. The most abundant class was 'low density', and seagrass maximum coverage was observed in September and minimum between April and May. In the southern shore, green macroalgae coverage showed a

maximum in February and a minimum in October and December in 2018 and 2019, respectively.

Water depth (*i.e.,* distance to the shoreline) was also an important factor affecting macrophyte seasonal dynamics. In winter, seagrass was more abundant in deeper waters (*i.e.,* distant from the shoreline) with algae on the surface. In early spring, the increase in water turbidity led to the almost disappearance of macrophytes (both algae and seagrass), with seagrasses recovering in mid-late spring, the recovery being faster in shallow waters for 'low density' meadows and in deep waters for 'high density' seagrass. In summer, algae overgrown on the northern shore, with seagrass abundance limited to the margins of algal mats (Figure 22). In the southern shore, seagrass spread all over the bottom, with lower densities present in shallower areas and higher densities in deeper areas distant from the coast. Finally, in autumn, both seagrass and algae coverage decreased. Interestingly, seabed coverage showed large variability in 2018 than in 2019. Algae density varied more in the northern shore, while seagrass presented more variations in the southern shore (Figure 21).

3.4. DISCUSSION AND CONCLUSIONS

Our results support the feasibility to characterize different aspects related to agricultural practices, crop phenology, and hydroperiod characteristics by monitoring the NDVI and NDWI, useful in rice farming monitoring. These results are in agreement with those reported by (Tornos *et al.*, 2015), the only previous similar study in the area. The multi-temporal S2-MSI dataset covering the southern Ebro delta for 2018-2019 includes more than 600 images based on the availability of clear-sky conditions and low-glint contamination risk. S2-MSI produces more accurate estimates due to its enhanced channel configuration, and its increased combined spatial (20 m) and temporal (5 days) resolution than other multispectral satellites, such as Landsat or MERIS. Thus, allowing precise determination of both inter and intra-annual crop dynamics. Among the tested spectral indices (*i.e.,* NDVI, NDWI1, NDWI2, and NDWI3), the combination of NDVI and NDWI1 provided the most useful values, with each index showing different possibilities along the crop cycle. According to both indexes, the Ebro Delta was homogeneous in terms of rice farming practices and crop development during the study period. However, 2019 showed a delayed crop calendar of *ca.* ~1 month when compared to 2018, these differences between years could be due to climatic conditions such as temperature (2018 was warmer than 2019) or rain. For instance, at the start of the growing season, in May, rainfall was 10.4 and 31.3 mm in 2018 and 2019, respectively. Consequently, in order to improve our results, further work should include climatic data. Furthermore, we used monthly averages of spectral indexes, which probably do not fit crop practices, thus further improvement should allow including more detailed crop practices and management information (*e.g.,* start of flooding, fertilizers application, harvest) by reducing temporal averages of spectral indexes.

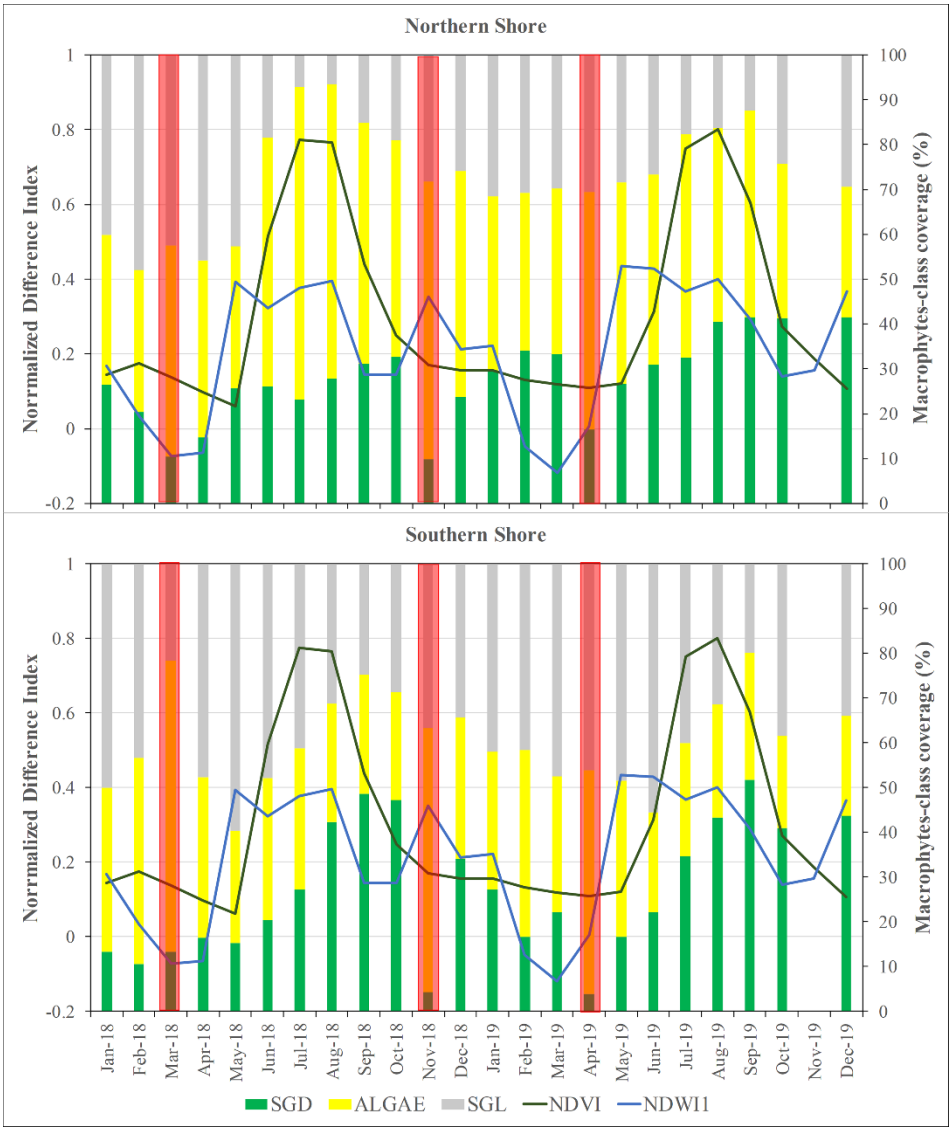

Figure 21. Rice spectral indexes (NDVI and NDWI1) and averaged per cent macrophyte-class. SGD: Seagrass dense, SGL: Seagrass low density and Algae) along the study period. In red, months not considered in the analysis due to higher water turbidity.

In relation to seabed classification, the proposed methodology (*i.e.,* S2-MSI merged composites and SVM-based classification) is effective in classifying macrophyte groups (algae and seagrass), as well as in identifying bare, sparse, and dense vegetation zones. Overall, our results were coherent with the literature. For instance, Sanmartí *et al.*, (2018) found that following the overgrowth of opportunistic macroalgae, seagrasses are displaced to deeper-water areas, thus explaining the replacement dynamic observed between seagrass and algae in the northern shore of

Alfacs Bay (Figure 22). However, some aspects need to be improved in order to improve the vegetation classification. For instance, given the similar spectral response, the class turbidity may include turbid-waters environments, sandy bottoms, and sparse macrophyte areas. In addition, epiphytes (organisms growing on the surface of plants) and water depth may increase the uncertainty of seabed classification by modifying the spectral reflectance response of seagrass and algae (Hwang *et al.*, 2019). It is needed to improve truth data classification (*i.e.,* get more field data and increase the number of classes).

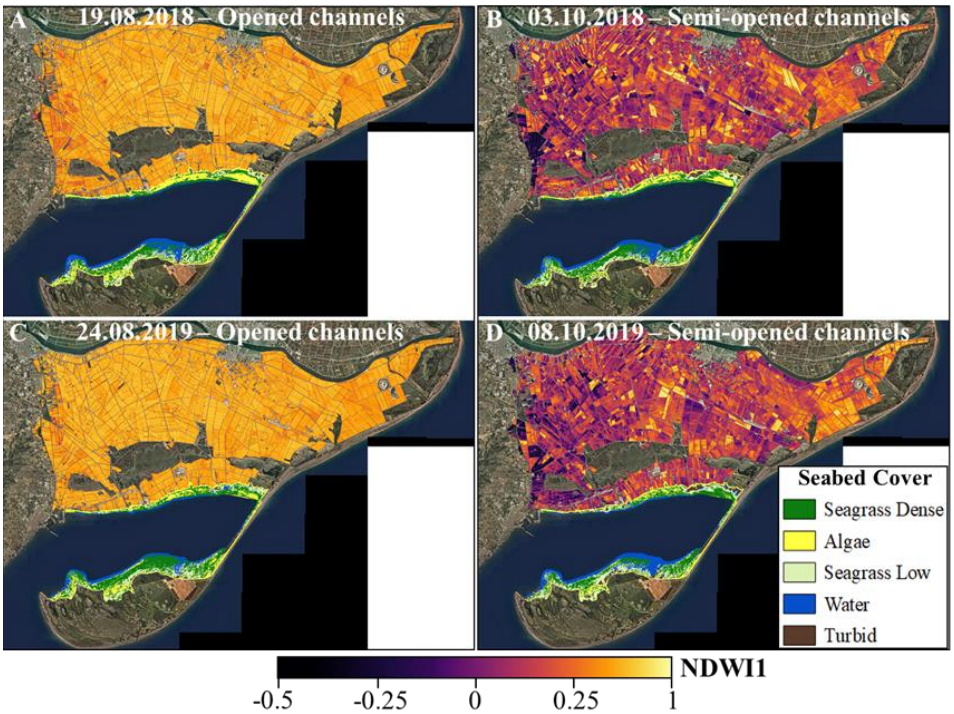

Figure 22. Examples of summer (A, C) and autumn (B, D) scenarios of flooding on the southern side of Ebro Delta and macrophytes in Alfacs bay.

Chapter 4

SENTINEL-2 FOR AGRICULTURAL MONITORING

RICE CROPS DYNAMICS AND YIELD ESTIMATION

An edited version of:

Soriano-González, J., Angelats, E., Martínez-Eixarch, M., Alcaraz, C. Monitoring rice crop and yield estimation with Sentinel-2 data. *Field Crops Research, 281, 2022.*

In the Ebro Delta, rice farming is the main economic activity and provides important ecosystem services, but it is also a major mediator of the environmental conditions in the coastal bays (see Chapters 2 and 3). This shows the need of an integrated monitoring of the Ebro Delta considering the interaction among environment and human activities. In this chapter, an automatic method for accurately defining crop dynamics (*i.e.*, phenology monitoring), agricultural practices (irrigation management), and indicators of crop yield from regional to field scale is developed. By combining different spectral indices computed in Google Earth Engine and S2 imagery, under a rule-based extraction scheme, different key dates and metrics are derived for two consecutive years. This study improves the limitations found in Chapter 3 in terms of rice monitoring, with key implications for further research based on the integrated approach for characterizing the evolution of the coastal system. The results presented can be useful for decision-making and the management of rice paddies.

4.1. INTRODUCTION

Rice provides food for more than half of the world's population, occupying more than 12 % of the world crop area, providing important ecosystems services such as habitat for fauna, prevention of saline intrusion and soil erosion, subsidence mitigation, and nutrient cycling (Tornos *et al.*, 2015). Accurate information on crop practices (*e.g.,* water management, hydroperiod, crop performance) along space and time is crucial for planning agricultural and environmental policies (Mosleh *et al.*, 2015). However, vegetation dynamics and hence rice yield, vary temporally and spatially due to several factors such as differences in soil properties, climatology, and management practices (Casanova, 1998; Bradley *et al.*, 2007). Thus increasing the difficulty to assess the spatial variability of the agricultural practices through field surveys, which is also costly and time-consuming. Sometimes, the only available information comes from farmers' declarations (Courault *et al.*, 2020). With the rapid development of geospatial technology in the last years, the acquisition of high-quality spatial and temporal data has become cost-effective and efficient, offering opportunities for land monitoring and management. In particular, multispectral satellite remote sensing has proved its usefulness in monitoring rice crops, water regime, and estimating yield production (Mosleh *et al.*, 2015; Dong and Xiao, 2016). Usually, spectral indices (SI) are used as a proxy for vegetation, flooding regime, and crop efficiency because they integrate the information of two or more spectral bands which are sensitive to different plant or soil characteristics (*e.g.,* plant pigments or water content) (Zeng *et al.*, 2020). Coarse-resolution sensors such as MODIS, AVHRR, SPOT-VEGETATION, and MERIS have been widely used since high-quality datasets are readily available and easier to process (Bolton *et al.*, 2020, Zhu *et al.*, 2019). However, because of their coarse spatial resolutions (from 250 m), it is difficult to differentiate management practices at single-field level (Liu *et al.*, 2020). Therefore, remote sensing data with better spatial resolution is preferred; for

instance, Landsat is able to provide images up to 30 m but at low temporal resolution (16 days) which is still an important constraint (Fernández-Beltrán *et al.*, 2021).

The Sentinel-2 (S2) satellites constellation provides accurate, timely, and easily accessible information of the land surface, with improved capabilities for vegetation mapping and monitoring, and phenology estimation (reviewed in Misra *et al.*, 2020). However, the use of S2 still presents some limitations related to time series development, including noise and data gaps (*e.g.,* atmospheric correction errors, decreased reflectance by shadows, cloud presence). In this sense, a common practice with multispectral remote sensing data is the usage of multi-temporal images composites derived from the combination of best quality pixels from images within a defined period (Sakamoto *et al.*, 2005; Wang *et al.*, 2012; Tornos *et al.*, 2015). Nevertheless, finding noise-free values may be complicated for short periods of time, and increasing the compositing period may lead to the loss of information (Zeng *et al.*, 2020). In some cases, there is insufficient cloud-free information present in the multi-temporal data to compose a cloud-free image (Schmitt *et al.*, 2019), and it is necessary to smooth data by filter-based methods or function fitting methods to fill temporal gaps and minimize the residual noise (Bradley *et al.*, 2007; Geng *et al.*, 2014). A complementary approach is the integration of data from different platforms (*e.g.,* Landsat, Sentinel-2), to reduce temporal gaps in multi-temporal composites (Liu *et al.*, 2020). However, data-fusion complexities (*i.e.,* temporal gaps, spectral harmonization, heterogeneity in cloud-masking methods, and spatial registration) make the possibility of using single-platform remote sensing data very attractive.

After completing the spectral index (SI) time series, the analysis of vegetation phenology, irrigation regime, and crop yield estimation will depend on the ability to characterize intra- and inter-annual dynamics at optimal scales. For the monitoring of rice-growing areas, it is crucial to differentiate key phenological stages (*e.g.,* heading date, maturity) and management practices (*e.g.,* flooding, harvest), both in space and time, particularly at small spatial scales. The main aim of this study is to assess the capability of Sentinel-2 to monitor rice crops in a Mediterranean growing area. Specific objectives are

(i) to generate cloud-free spatiotemporal time series of four SI (NDVI, $NDWI_{MF}$, $NDWI_{GAO}$, and BSI) along two consecutive crop seasons (2018 and 2019);

(ii) to automatically identify the main phenological stages and management practices at different scales (from regional to field);

(iii) to provide estimates of rice yield.

4.2. MATERIALS AND METHODS

4.2.1. Study area

As shown in Chapter 1, the 65% of Ebro Delta area (21,125 ha) is devoted to rice farming (Figure 23), constituting the main economic activity in the region and providing important ecosystem services. Rice is grown from late April to September and left fallow during the rest of the year (Figure 24). The cultivars grown in the Ebro Delta, are japonica-type with medium grain size and growth cycle of *ca.* 120 to 140 days from sowing to maturity. In general, the variability of cultivars grown in the area within a year is low, *ca.* 5 different rice cultivars cover most of the cultivation area.

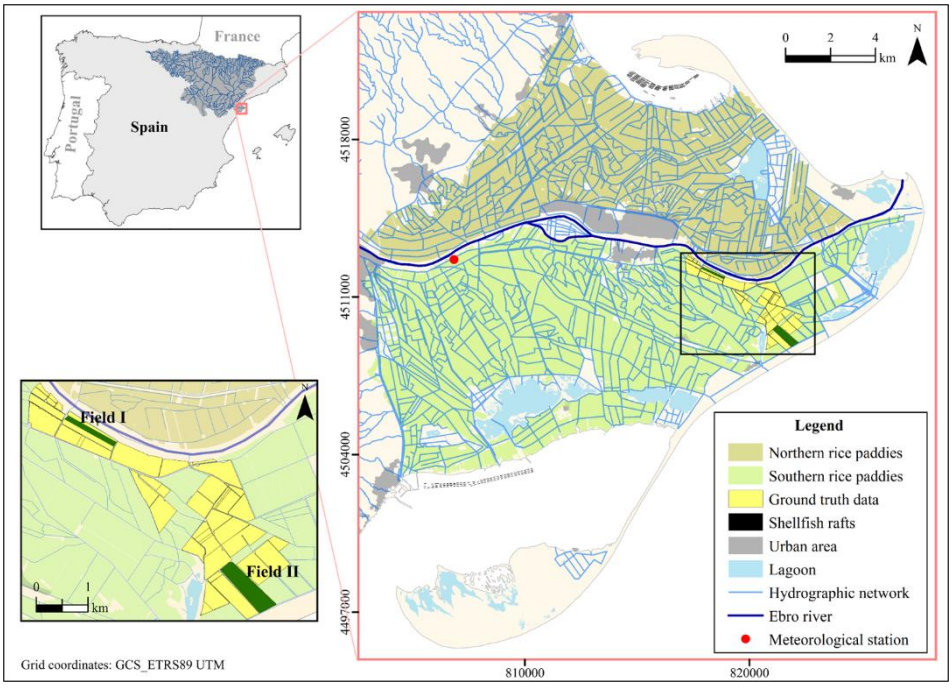

Figure 23. Location of the Ebro Delta and coverage of rice paddies under study. Fields I and II are used in support of sections 4.3 and 4.4.

4.2.2. Study design

The study was carried out over two consecutive years (2018-2019). Annual cadastral data of all rice parcels were obtained from the Department of Agriculture, Livestock, fisheries, and food of the regional government (http://agricultura.gencat.cat). Four scenarios, considering different spatial scales, were analyzed: Scenario 'A' included all rice fields in the Ebro Delta; Scenario 'B' and 'C' considered all paddies in the northern and southern hemidelta, respectively; and in Scenario 'D' 67 subsets of rice fields were analyzed (Figure 23) for which field and crop information, including at

least cultivar, agricultural practices (*i.e.,* sowing, harvesting dates), or yield (kg·ha^{-1}), were obtained from the owner. In Scenario 'D', Field I and Field II (Figure 23) were chosen as an example to facilitate results interpretation. Field I (10.8 ha) is close to the Ebro River (Figure 23) and seeded with Mare cultivar in both 2018 and 2019. Field II is the largest field in scenario 'D' (37.4 ha), Bomba and Sirio cultivars were grown in 2018 and 2019, respectively.

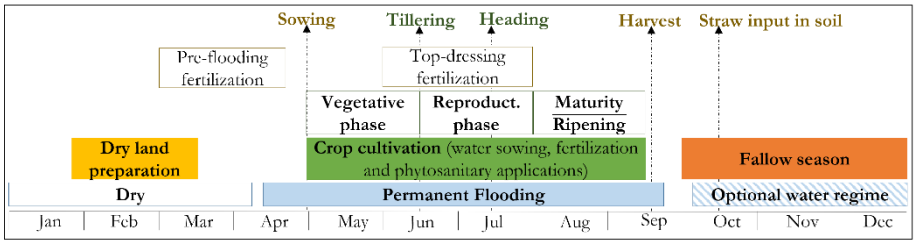

Figure 24. Rice farming calendar in the Ebro Delta. Adapted from (Martínez-Eixarch *et al.*, 2018).

4.2.3. Satellite data

Google Earth Engine (GEE), a cloud-based platform for long-term geospatial analysis (Gorelick *et al.*, 2017), was used for data access, clouds and clouds shadows detection, image pre-processing (*i.e.,* image subset, mosaicking of tiles, and image resampling), and spectral index calculation. In GEE, image collections of both Sentinel-2 A/B (S2) top of atmosphere (L1C, TOA) and atmospherically corrected for surface reflectance (L2A, BOA) from 1st of January 2018 to the 31st of December 2019 were used. All images were obtained from the same orbit (051) and tiles (TCF31 and TBF31) to homogenize remote sensing measurements and ensure the full coverage of the study area. First, all available BOA images within the study period were loaded (N_{images} = 138); then, TOA images were selected based on the available BOA dates. TOA images were needed as the base of the method used for masking clouds and cloud shadows (adapted from Schmitt *et al.*, 2019). Water masking was not applied to avoid interferences with flooded rice paddies and, only the second module of the Schmitt *et al.* (2019) method was used (*i.e.,* image quality score module). This generates a pixel scoring for each independent TOA image and date by combining the probabilities of cloud presence given different assumptions about brightness, moisture, and snow. Cloud masks were derived with a threshold of 0.3 on the pixel score. Then, the cloud masks, in conjunction with the TOA images metadata (sun azimuth and zenith) and a range of possible cloud heights (from 200 m to 10000 m) were used to generate shadow scores images and shadow masks. The threshold on the sum of infrared bands to include as possible shadows was lowered from 0.3 (default) to 0.1 for reducing the miss-classification of flooded paddies. For more detailed information on the cloud and shadow masking method see Schmitt el al. (2019).

The computed masks for TOA images were applied to the BOA collection, and after clouds and clouds shadows masking, S2 BOA images were cropped to the region of interest (Figure 23), daily mosaicked (merging of same-date tiles), and resampled to 20 m spatial resolution. For each scenario images were filtered according to cloud and shadow mask percent coverage over rice fields. Only those images with at least 80 % of valid pixels per scenario were included in the posterior analysis and, for each valid S2 image (Figure 25) SI were computed (see section 4.2.4) at pixel level (*i.e.,* 20 m x 20 m) and then averaged at different scenarios scales.

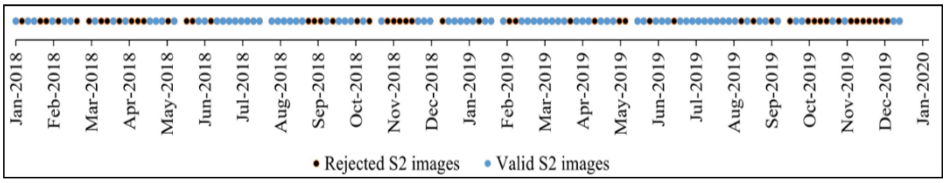

Figure 25. Valid and rejected S2 images.

4.2.4. Spectral indices

Four SI were calculated according to their utility in estimating rice development, water management, or production (Table 6). These two and three-band normalized difference indices are dimensionless, range between -1 and 1, and exploit the VIS, NIR, and SWIR regions of the spectrum (Table 6). The Normalized Difference Vegetation Index (NDVI) exploits the chlorophyll light absorption in the VIS-red region of the spectrum and the high reflectance of vegetation in the NIR (Rouse *et al.*, 1974). The Normalized Difference Water Index proposed by McFeeters (1996), here referred to as $NDWI_{MF}$, was developed for delineating open water bodies by making use of the NIR and VIS-green light. The Normalized Difference Water Index by Gao (1996), here referred to as $NDWI_{GAO}$, was developed for the remote sensing of vegetation liquid water by using the NIR and SWIR channels. The Bare Soil Index (BSI) is used to identify bare soil areas and fallow lands, by combining information from the VIS-blue, VIS-red, NIR, and SWIR channels (Rikimaru *et al.*, 2002).

4.2.5. Data smoothing

For each S2 valid image and considered scenario, SI data were smoothed with a cubic spline fitting method, thus estimating daily data at different scenario scales, and reducing multi-factorial noise in the original data (*e.g.,* atmospheric correction or cloud/shadows miss-detection derived errors). Cubic spline fitting is based on the minimization of quadratic errors with curvature type regularization by joining piecewise polynomials smoothly at selected knots from the original data points (Wang, 2011). Thus, the fit is not limited by any method-constrained shape, but phenological shape is driven entirely by the data (Bradley *et al.*, 2007). The cubic spline smoothing was done in R version 3.6 (R Core Team, 2017) by using the smooth.spline function; all data were included as possible knots and the spar smoothing parameter was fixed to 0.65.

Table 6. SI used in this study. The R(λ) in equations stands for Surface Reflectance at S2 band with centered wavelength λ in nm.

Spectral Index	Equation
Normalized Difference Vegetation Index NDVI (Rouse *et al.* 1974)	$\frac{R(842) - R(665)}{R(842) + R(665)}$
Normalized Difference Water Index $NDWI_{GAO}$ (Gao *et al.*, 1996)	$\frac{R(842) - R(1610)}{R(842) + R(1610)}$
Normalized Difference Water Index $NDWI_{MF}$ (McFeeters *et al.*, 1996)	$\frac{R(560) - R(842)}{R(560) + R(842)}$
Bare soil index BSI (Rikimaru *et al.*, 2002)	$\frac{(R(1610) + R(665)) - (R(842) + R(490))}{(R(1610) + R(665)) + ((842) + R(490))}$

4.2.6. Rice phenology, hydroperiod and yield

Smoothed NDVI and $NDWI_{GAO}$ time series were combined to assess rice phenology, crop evolution, and flooding practices. The BSI was computed as an additional state indicator complementing the analysis of NDVI and $NDWI_{GAO}$, but it was not included in the feature extraction system. The $NDWI_{MF}$ was only used for crop yield estimates. The method for automatic extraction of key features consisted on the assumption that the presence of local maximums, minimums, and critical points (inflection points) in spectral index trends is related to changes in soil, flooding, or vegetation stages (Zheng *et al.*, 2016; Liu *et al.*, 2017). For the different scenarios considered, SI time series were smoothed, and all minimums and maximums were identified from the first derivative analysis; and all possible inflection points were identified for NDVI, $NDWI_{GAO}$ and BSI. Then, local and critical points of interest were selected (Table 7).

First, the absolute maximum NDVI was associated with the middle heading date (HD) of each growing season as proposed in (Wang *et al.*, 2014; Tornos *et al.*, 2015; Zhang *et al.*, 2019). From the HD, other key features were derived for each year following the identification steps and order presented (Table 7 and Figure 26). The order was based on the expected occurrence of events (*e.g.,* Active tillering occurs before HD; End of flooding of one growing season occurs before flooding of the following one), allowing to automatize the process by avoiding unwanted minimum/maximum and inflection points. Key features related with rice status were extracted first from NDVI, and then $NDWI_{GAO}$ was used to assess water management (Table 7 and Figure 26).

For scenario 'D', Pearson's correlation coefficient (*r*) was used for assessing the relationship with available ground truth data of i) Sowing date and $NDWI_{GAO}$-derived flooding (F), ii) Harvest date and NDVI-derived maturity (M) and, iii)

Annual rice production (kg·ha^{-1}) and the value of the four SI at all dates within the study period.

Table 7. Key phenological and field-status features identified in this study.

Acronym	Key feature	Description	Identification
HD	Heading Date	Phenology: Vegetative development of rice is maximum.	Absolute maximum NDVI
T	Tillering	Phenology: Active tillering. The number of leaves increases rapidly	1st inflection point of NDVI before HD
M	Maturity	Phenology and Management: Close to end of maturation stage	1st inflection point of NDVI after HD
F	Flooding	Management: Flooding of rice fields have started	1st inflection point of $NDWI_{GAO}$ before T & after minimum $NDWI_{GAO}$
EF	End of Flooding	Management: Water in fields is emptied before the land preparation	1st inflection point of $NDWI_{GAO}$ before minimum $NDWI_{GAO}$ of 2nd year
RF	Re-Flooding	Management: Optional re-flooding of fields during the fallow season.	Inflection point of $NDWI_{GAO}$ after M and before EF.
VP	Vegetative Phase	Phenological phase: From germination to panicle initiation	Period between F and T
RP	Reproductive Phase	Phenological phase: From panicle initiation, till flowering	Period between T and HD
MRP	Maturity-Ripening Phase	Phenological phase: From flowering and ripening till M	Period between HD and M
PF	Permanent Flooding	Management: Fields are always flooded but level of water may vary due to punctual drainages.	Period between F and EF.
DLP	Dry Land Preparation	Management: rice fields are dry and land is being prepared	Period between EF and F. Related to minimum $NDWI_{GAO}$ and maximum BSI

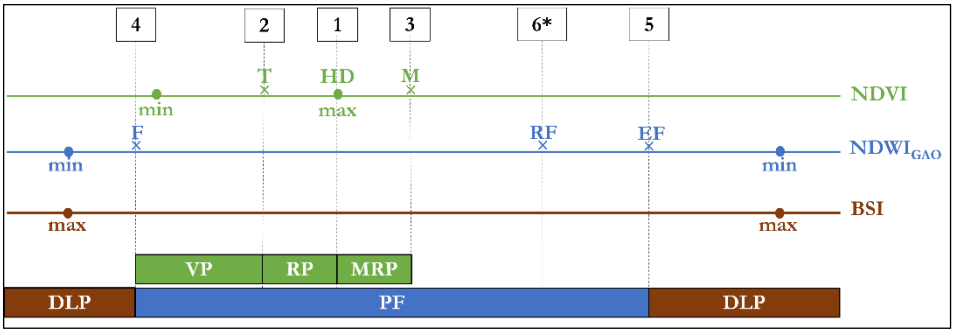

Figure 26. Extraction scheme of phenology and irrigation management practices from combined NDVI and NDWI$_{GAO}$ dynamics. Numbers stand for the order of identification of key features, × Inflection Points, ● Local Points. List of acronyms in Table 7.

4.3. RESULTS

4.3.1. Cloud and shadow masking

We did not conduct a systematic validation of cloud and shadows masking, but it was visually observed that the adaptation of the Schmitt *et al.* (2019) method improved the default Quality Assessment (QA) cloud mask of S2 L2A imagery (QA60 band), particularly in the presence of disperse or patched clouds (Figure 27). However, in this situation, problems related to the detection of smallest, thinner clouds and shadows were also observed. These limitations were not addressed from an image processing perspective. In such cases (*e.g.,* Figure 27), the study relied on second filtering (80% of valid pixels within each scenario which include only pixels covering rice paddies), the averaging of pixels and the smoothing of the time series to decrease the impact from the misclassification of clouds and shadows.

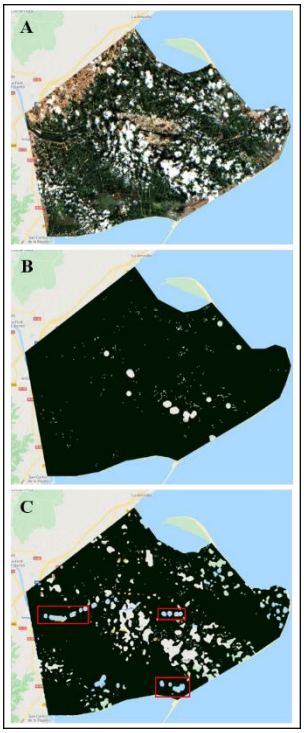

Figure 27. The S2 BOA Image clipped to the area of study on 30th July 2019 as viewed in GEE. A) RGB, B) QA60 band-based method, C) Adapted method. Black pixels correspond to not-masked areas. Red squares: Examples of possible overestimation of shadows over water.

Overall, 53 of 138 images (*ca.* 38.5 %) had more than 20 % of pixels affected by clouds or shadows and were discarded; most of them within the period October-December, after the rice growing cycle (Figure 25).

4.3.2. Spectral indices time series

The cubic spline smoothing filled gaps for fitting time series with daily information of each spectral index derived from S2 imagery at different scenarios scales. The metrics of the spline fitting (*i.e.,* Pearson's *r* and Root Mean Squared Error, *RMSE*), and thus the relationship between observed (*i.e.,* satellite-derived) and predicted values, differed among SI. Considering all the scenarios, the weaker correlations were found for $NDWI_{GAO}$ ($0.77 < r < 0.94$, $0.12 > RMSE > 0.05$), and the strongest correlations were for BSI ($0.84 < r < 0.98$, $0.073 > RMSE > 0.032$), $NDWI_{MF}$ ($0.93 < r < 0.99$, $0.08 > RMSE > 0.04$), and NDVI ($0.95 < r < 0.99$, $0.09 > RMSE > 0.04$). These differences were particularly evident during the rice-growing season, and particularly, the variability of $NDWI_{GAO}$ at the beginning of the growing season was not totally retained by the smoothing (Figure 28C).

At spatial scale, the number of valid images was lower for smaller scenarios (*i.e.,* scenario 'D'), and at temporal scale, the number of available images was lower during the post-harvest season, in the autumn-winter period (Figure 25 and Figure 28), thus affecting the accuracy of the smoothing. To reduce the uncertainty in these extremes of the smoothed time series, the phenology and hydroperiod phases (see section 4.3.3) were only classified from the 2018 flooding to the 2019 mature-ripening stage, excluding the initial pre-flooding and final post-harvest periods (Figure 29). SI showed common patterns among the different scenarios considered, and significant differences were not observed among Scenarios 'A', 'B' and 'C'. Scenario 'D' showed higher variability, mainly due to differences among individual paddy fields, but with common characteristics among them (Figure 29).

Overall, both NDVI and $NDWI_{GAO}$ minimum values were observed between the winter and the middle-spring period, coinciding with maximum BSI. The maximum rate of increase of $NDWI_{GAO}$, associated with flooding, occurred around April-May. Along the growing season, the NDVI reached its maximum in July-August, with the BSI showing an inverse pattern (Figure 29). After the growing season (autumn and winter) the differences among fields (Scenario 'D') were more evident, and three main SI trends were found: NDVI stabilization with an increase in $NDWI_{GAO}$ and a decrease in BSI; a reduction in both NDVI and $NDWI_{GAO}$ (Field I) with BSI increasing (Figure 29A); and an increase in both NDVI and $NDWI_{GAO}$ (Field II) associated to a marked decrease in BSI (Figure 29B).

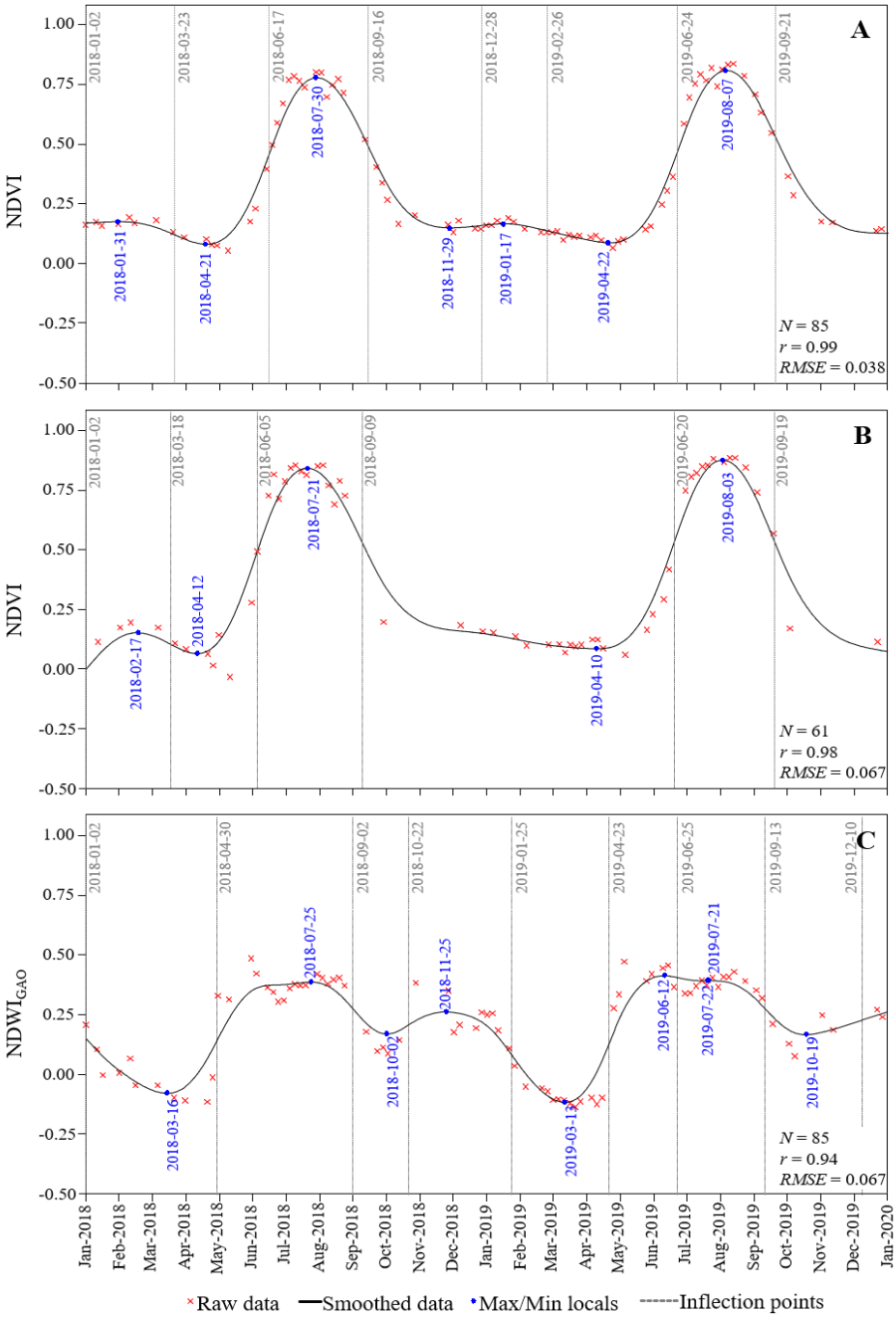

Figure 28. Spline smoothing of SI at different spatial scales. A) Mean NDVI in Scenario 'A'; B) Mean NDVI in Field I of Scenario 'D'; C) Mean $NDWI_{GAO}$ in Scenario 'A'. Root Mean Squared Error (*RMSE*), number of data points (*N*) and Pearson's *r* are provided.

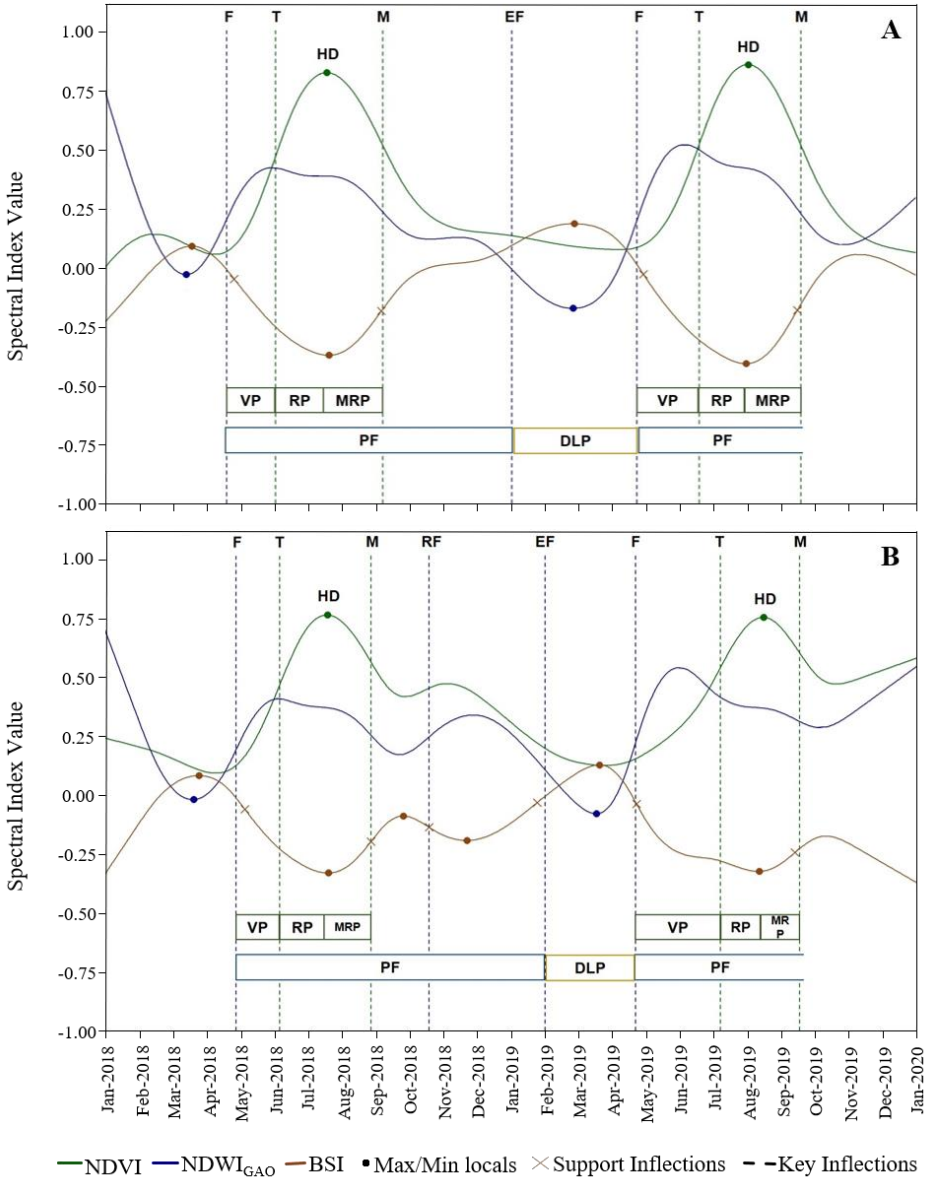

Figure 29. Rice phenology and hydroperiod at two different sub-scenarios in the Ebro Delta derived from NDVI and $NDWI_{GAO}$. The BSI trend is shown as supporting information. A) Field I; B) Field II (Figure 23).

4.3.3. Phenology and hydroperiod detection

A selection of maximum/minimum and inflection points in NDVI and $NDWI_{GAO}$ time series were used to extract phenology and hydroperiod dynamics for the different scenarios considered (Table 7 and Figure 26). Flooding (F), active Tillering

(T), Heading Date (HD), Maturity (M), End of Flooding (EF), Vegetative Phase (VP), Reproductive Phase (RP), Mature-Ripening Phase (MRP), Permanent Flooding (PF), Re-Flooding (RF), Dry Land and Land Preparation (DLP) crop phases were identified. Comparing the global trends in 2018 and 2019 at different scenarios scales, HD was delayed in 2019 and MRP was shorter in 2019. The temporal variation of NDVI and $NDWI_{GAO}$ indexes were more related to factors such as water management, type of sowing, field characteristics or climate, than to rice cultivar. See for instance Field II (Figure 29B), where different rice cultivars were sowed in 2018 and 2019.

The consistency of the results was achieved when only fields with more than 40 valid Sentinel-2 images (during the two years) were included in the analysis (Table 8). On average, Flooding was detected 9 and 12 days before the ground truth sowing date (late April to late May), and Maturity was observed 6 and 8 days before the ground truth harvest date (late August to early October), in 2018 and 2019 respectively. Despite the larger variability observed between flooding and sowing occurrence, the relationship was > 0.6 (Pearson's *r*) for all evaluated fields with more than 40 Sentinel-2 images (Table 8).

Table 8. Relationship between estimated flooding date (F) and ground truth sowing and between estimated maturity date (M) and ground truth harvest data by year. Only fields with more than 40 valid Sentinel-2 images were included.

Year	N_{images} (min-max)	Key feature	Ground data	N_{fields}	Mean difference (days)	Standard deviation (days)	*r*
2018	60 - 82	Flooding	Sowing	19	-12.26	3.57	0.79
2018	60 - 82	Maturity	Harvest	19	-8.37	7.75	0.61
2019	41 - 82	Flooding	Sowing	23	-9.04	11.68	0.66
2019	41 - 82	Maturity	Harvest	23	-6.57	3.42	0.93

4.3.4. Rice yield estimates

In Scenario 'D', SI were correlated (Pearson's *r*) with yield production ($kg \cdot ha^{-1}$). The strongest correlations were found in the growing season, mainly between July and middle-August (Figure 30), with rice yield significantly correlated with all SI. The best correlations observed in 2018 and 2019, respectively, were $r = 0.69$ and $r = 0.74$ with NDVI, 0.82 and 0.66 with $NDWI_{GAO}$, -0.84 and -0.86 with $NDWI_{MF}$, and -0.81 and -0.71 with BSI. Along the summer season, the most consistent relationships with yield production were obtained with $NDWI_{MF}$ and NDVI (Figure 30).

For this reason, the study focused on the relationships between rice yield and the annual NDVI maximum (at the HD), and the annual $NDWI_{MF}$ minimum (closest local point to HD). Best results (Figure 31) were obtained when considering only rice fields with mean NDVI > 0.4 ($r = 0.72$) or $NDWI_{MF} < -0.4$ ($r = -0.80$).

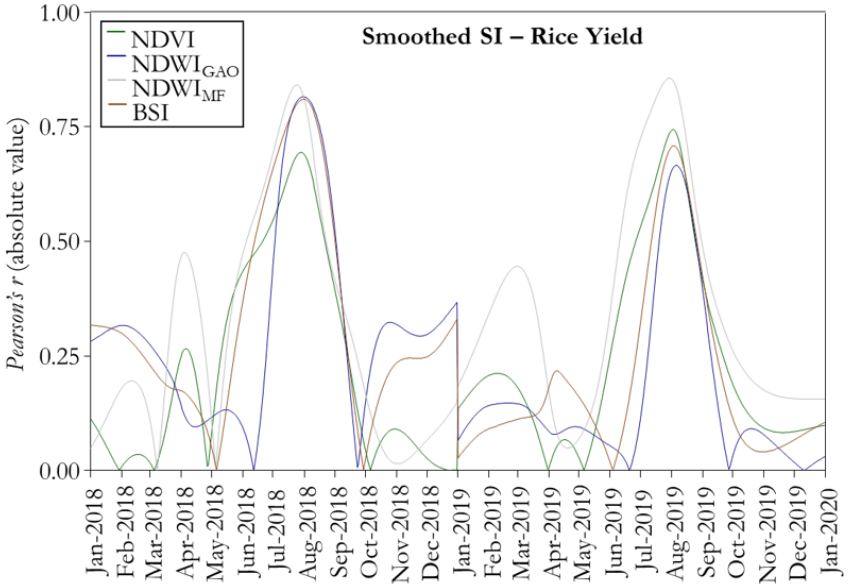

Figure 30. Absolute Pearson's correlation (*r*) between parcels production (Kg·ha^{-1}) and SI daily values along the period studied.

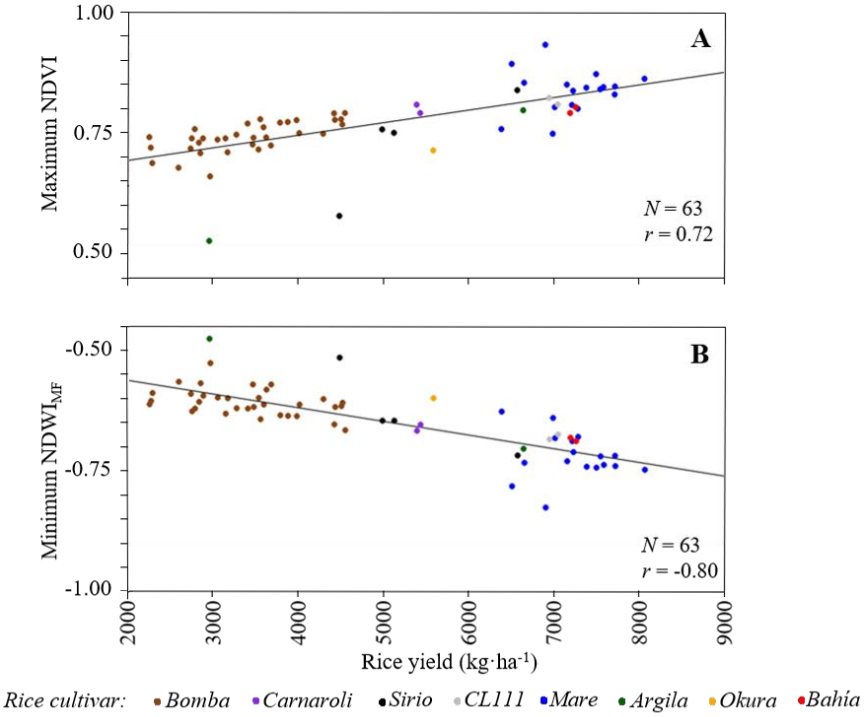

Figure 31. Scatter plot and Pearson's correlation (*r*) between yearly production by sub-scenarios in 'D' and; A) Maximum yearly NDVI for the corresponding parcels; B) Minimum yearly NDWI$_{MF}$ for the corresponding parcels.

4.4. DISCUSSION

4.4.1. Methodological requirements and limitations

The study has been conducted on a small homogeneous area were rice is the dominant crop. Cadastral information is annually updated from farmers' official declarations. Furthermore, for the assessment on individual fields (Scenario 'D'), ground truth data included yearly information of rice parcels, with single cultivar and crop management in each one. This information was used to conduct a retrospective analysis based on a 'unit' approach (pixels averaged within fields under the same conditions) in a single-season and low-yielding system. The proposed methodology has not been tested in other types of rice systems and it is not intended for near real-time monitoring. Additional land cover classification is needed in absence of ancillary data, with particular importance under mixed crops scenarios, thus moving from 'unit-field' to 'pixel-based' approach and using, for instance, classification methods based on the detection of the particular practice of field flooding, for differentiating rice-growing areas/pixels (Boschetti *et al.*, 2014; Boschetti *et al.*, 2017). These, may be later aggregated by means of different criteria such as proximity (distance between pixels) or spectral trends' similarity.

In this study, the main limitation were satellite data gaps since 40 % of the available S2 images for the selected orbit and period had less than 80 % of valid pixels. The number of rejected images increased in smaller scenarios. Although the selection criterion discarded a large number of S2 images, it was necessary for reducing the uncertainty related to cloud and cloud shadow miss-detection and reducing the noise of final mean SI values. Cloud presence and cloud shadow masking is a key issue in optical remote sensing, and the default operational Sentinel-2 QA60 has been shown to commit high errors in presence of thin or patched clouds (Coluzzi *et al.*, 2018). Thus, we preferred the adapted masking method of Schmitt *et al.* (2019), which has the advantage that can be easily tuned, making it suitable for a wide range of scenarios. The mean gap between consecutive images was 9 days, usually ranging between 5 (S2 temporal resolution) and 10 days, thus improving other similar platforms such as Landsat, with a best temporal resolution of 16 days. The largest gaps due to cloud presence were of 25 days (November 2019), 30 days (November 2018), and 40 days (December 2019), but in these months a lower variability in rice fields is expected (the growing season is from mid-April to early September) and a reduced temporal resolution during this period did not affect the results significantly. Increasing temporal resolution is more important in the growing season when changes occur within days or weeks. In this case, further research should consider improving the methodology for thin cloud and clouds shadows masking for reducing data gaps, particularly, at field scale. Although it can provide valuable information, our results indicate that Sentinel-2 alone is not enough for an accurate phenology monitoring for crop management. In this sense, it is suggested the use of multi-platform data. In the optical domain, the fusion of Sentinel-2 and Landsat-8 is recommended (Liu *et al.*, 2020; Boschetti *et al.*, 2018), since both platforms' pixel sizes are smaller than individual rice fields. A complementary approach is generating

cloud-free time series of synthetic high-resolution images (*e.g.,* Sentinel-2, Landsat-7/8) from moderate resolution data such as MODIS imagery (Wu *et al*., 2018, Gao *et al*., 2015). However, image processing of data from multiple satellites/sensors is challenging, for instance, due to differences in their orbital, spatial, spectral response functions, and image processing chains (Campos-Taberner *et al*., 2017).

4.4.2. Application of spectral indices

The NDVI and $NDWI_{GAO}$ were combined to estimate key cropping phases (*i.e.,* Flooding, Tillering, Harvest, Maturity, and Re-Flooding), and $NDWI_{MF}$ was related to crop yield.

NDVI was limited to the rice-growing season for assessing rice phenology, mainly Tillering, Heading Date, and Maturity. In previous studies, NDVI has been used for showing the transition from bare flooded soil to rice emergence (Tornos *et al*., 2015). In this study, this transition was not clearly identified since the canopy cover is scarce at the beginning of the cropping and soil-related factors may affect NDVI values (Zhang *et al*., 2019). In relation to the identification of the Tillering stage, the temporal gap between Flooding and Tillering agreed with the common rice farming calendar in the Ebro Delta (Figure 24). Although the proposed method differentiated small variability between nearby fields' dynamics (Scenario 'D'), no phenological field data were available for validating its accuracy. We used the NDVI inflection point before the Heading Date for defining the start of the active Tillering stage as previous works have reported that active Tillering is associated with the maximum increase rate of NDVI, related to the fast growth of rice plants during this stage (Zheng *et al*., 2016). The Heading Date has been related to the maximum in NDVI, which is associated with a peak in Leaf Area Index (LAI), showing an increase in plant biomass (Wang *et al*., 2014). The maturity date (M) is associated with a rapid decrease of NDVI at the end of this stage (Zheng *et al*., 2016) and it was significantly related to the harvest date ($r > 0.6$). The delay observed between the maturity date (S2-derived) and the harvest date (reference data) could be related to farmers' harvest practices, since harvest is mediated not only because the ripening state of rice but also considers other external factors (*e.g.,* weather, machinery availability). However, more ground truth data including also additional information (*e.g.,* HD, T) and covering a larger extension (ground truth data in this study was limited to a subset of spatially aggregated fields) is further needed for deeply assessing the accuracy on the identification of key phenology features through the proposed extraction scheme. $NDWI_{GAO}$ variations were associated with hydroperiod and can be applied as an indicator of flooding management in rice paddies (*i.e.,* Flooding, End of Flooding and Re-Flooding). Our results were similar to those reported in Tornos *et al.* (2015) in the Ebro Delta and Boschetti *et al.* (2014) in rice fields from Italy, both using data derived from MODIS. The $NDWI_{GAO}$ responds to water level fluctuations from flooding to rice tillering, and after the rice is harvested. However, with the increase in leaf coverage during the reproductive and rice ripening phases, $NDWI_{GAO}$ could be more associated with the canopy

structure and mediated by plant water content and metabolic activity (Serrano *et al.*, 2019; Zhang *et al.*, 2019). For the same reason, the identified Re-flooding (RF) should be carefully considered in presence of a second NDVI peak after harvest (*e.g.,* Figure29B). This peak may be related to the presence of weed or rice regrowth (Tornos *et al.* 2015) with an expected impact on the $NDWI_{GAO}$ dynamics. Consequently, $NDWI_{GAO}$ is useful for complementing NDVI-derived phenology and vegetation status in rice fields, but the index variability increases in the presence of vegetation, highlighting the need to improve data frequency. The $NDWI_{GAO}$ derived flooding results are a promising estimator of the sowing date ($r > 0.6$), with sowing occurring, on average, 9 to 12 days after flooding (Table 8). Despite these differences are in agreement with the general rice farming calendar in the Ebro Delta (Figure 24), high variability was observed (up to ±11 days). This variability may be explained by different types of sowing (*e.g.,* direct seeding, transplanting, dry-seeding) and farmer's decisions on sowing time, which increase the uncertainty in their relationship. These issues must be further tackled, but ground truth data regarding water management practices and sowing management are needed.

The BSI was mainly used as a reference for complementing the analysis of NDVI and $NDWI_{GAO}$ results, under the assumption that maximum BSI occurs when a rice field has no water and no vegetation. Applying the first and second derivatives analysis on BSI showed that minimum and maximum were related with HD and dry land, respectively; while inflection points in BSI were closer to the identified flooding and maturity-harvest (Figure 29). A further assessment of BSI capabilities within the proposed extraction scheme is planned, since it may combine important key features of both NDVI and $NDWI_{GAO}$ for the management of rice-growing areas.

Finally, $NDWI_{MF}$ temporal pattern was similar but inverse to NDVI, thus no additional information on crop cycle was obtained. However, minimum $NDWI_{MF}$ was highly correlated to crop yield in the Ebro Delta ($r = -0.80$), showing good agreement between fields with different yields and cultivars (Figure 31). $NDWI_{MF}$ includes the same spectral bands as the Green NDVI (Gitelson *et al.*, 1996a) which has been used before for crop yield estimates (Moreno-García *et al.*, 2018). In low-yielding rice systems (< 9000 $Kg \cdot ha^{-1}$), such as the Ebro Delta, two spectral bands SI are not affected by the saturation phenomenon due to low crop biomass (Xue *et al.*, 2014), thus explaining the strong relationship observed between $NDWI_{MF}$ and yield. Different from the relationship achieved for sowing and harvest, crop yield estimates were not strictly related to the number of valid satellite images of the study period. It is explained because the minimum $NDWI_{MF}$ used occurs close to the HD, in summer, when smaller data gaps are expected. Nevertheless, previous studies have shown that from tillering to harvest, different stages of rice are suitable for crop yield estimation (Xue *et al.*, 2014; Cao *et al.*, 2016; Moreno-García *et al.*, 2018), but these stages can be more complex to identify.

4.4.3. Ebro Delta Rice Development (2018-2019) and Management Implications

In terms of rice paddies dynamics, similar results were obtained in Scenarios 'A', 'B', 'C', and in most of the fields in Scenario 'D', thus showing the homogeneity of agricultural practices in the Ebro Delta along the study period (2018-2019). Those results are similar to those reported by Tornos *et al.* (2015) from 2001 to 2012, which suggested not only spatial but also temporal homogeneity in rice management in the Ebro Delta. Considering Scenarios 'A', 'B' and 'C', the main differences between both years related to rice development were a delay in heading date and a larger ripening phase in 2019, which might be mediated by climatologic factors. For instance, before the start of the growing season, the total precipitation in April varied between 40.5 mm in 2018 to 8.9 mm in 2019 (Meteorological Service of Catalonia, https://www.meteo.cat/wpweb/climatologia). Although different meteorological factors (*e.g.,* air, solar radiation) or soil features may affect the crop (Sánchez *et al.*, 2013; Zhao *et al.*, 2016), heavy rains increase fields' water level, which mitigates heat and salinity stress to the crop (Martínez-Eixarch *et al.*, 2018), contributing to modulate the length of the different phenological phases of the crop.

At small spatial scales, our study provides an insight into the potential of S2-derived SI for the characterization and assessment of the dynamics of rice fields and crop yield estimates in low-yielding rice farming systems. The proposed method allowed to capture small dynamics variations among fields (Scenario 'D'), automatically, with importance from a management/planning sight. For instance, yearly crop yield estimates at field-level or different field management practices after harvest (*e.g.,* re-flooding, progressive drying or rice regrowth) are key aspects for the development of agro-environmental policies and productive and sustainable wetlands. Further research will focus on increasing both satellite and ground truth data for addressing the main limitations found and being able to provide relevant information for authorities at a regional scale.

4.4.4. Basis for a pixel-wise approach: A first insight on method, potential and limitations

This subsection is beyond the edited version of the paper and is added to show the potential and applicability of the proposed method. Annual maps, as example of key dates and minimum $NDWI_{MF}$ as proxy for rice yield, have been generated at pixel scale (20 m). Annual cadastral data were used for masking rice fields. The method described in section 4.2.6 only produced results in a 'unit' base (*i.e.,* pixels averaged within field). Thus, metrics extraction can fail in pixels which spectral response is not only related to intensive rice farming (*e.g.,* mixing of pixels in field margins, cadastral errors). The proposed methodology will provide reliable estimations only under homogeneous crop conditions. In this context, it is needed to identify those pixels more likely to fit system requirements (classification of valid rice pixels), and then apply the extraction-scheme for those pixels, avoiding uncertainties. Thus, we

developed rule-based methods to identify a rice field when clear and unambiguous flood conditions are detected before consistent and rapid vegetation growth, among other assumptions on characteristic rice crop dynamics (Xiao *et al.*, 2005, Boschetti *et al.*, 2014; Boschetti *et al.*, 2017).

Adaptation of the extraction-scheme method to pixel resolution

Accounting for the requirements of the automatic extraction method presented, a preliminary flags' system has been applied for selecting valid rice pixels and extracting pixel-wise information on Tillering date (T), Heading Date (HD), Flooding date (F), and the minimum $NDWI_{MF}$. With them, the pixel-wise adaptation of the extraction method and the potential of the producible results are discussed. Including the constraints previously defined for the 'unit' base approach (see 4.3 and 4.4.1), six conditions have been fixed for simplifying the production of the example maps (Table 9). Each condition is a flag, excluding pixels from the automatic extraction of key dates and features. The flags increase the reliability of data smoothing by increasing the number of points, and enhance the performance of the automatic extraction method, allowing inter-annual comparisons of rice dynamics at pixel scale. In this context, the presence of inflection points related to T and F, as well as the thresholds of NDVI and $NDWI_{MF}$ (Table 9), reduce the probability that a pixel does not belong to the intensive low-yielding rice pixel class, for which the extraction scheme was initially developed. Other authors proposed similar approaches by either using different vegetation indexes such as the Enhanced Vegetation Index, with improved sensitivity in high biomass regions (Boschetti *et al.*, 2017), or by identifying the Heading period instead of HD, and other additional key information such as the NDVI trend just after the harvest period (Chen *et al.*, 2011).

Approximately 19 % of pixels inside the rice masks were flagged for 2018 and 2019 (Figure 32). Most of pixels were flagged due to the low number of valid images or dates along the two-years period (*ca.* 78 %). The 'wrong flooding trend' flag was the third most probable in both 2018 and 2019 (about 14 and 18 %, respectively). Overall, more than 80 % of the total number of pixels were accepted.

Table 9. Nomenclature and definition of flags for invalid pixels.

Flag	Meaning
< 40 images	Less than 40 valid dates of S2 imagery for the 2 years-period
1 year or IQR	S2 cloud-free data within the rice masks along the two years of the study was not available or the Interquartilic range of dates was negative
NDVI at the HD < 0.4	For each year, the NDVI at HD was lower than 0.4
Minimum $NDWI_{MF}$ > -0.4	For each year, the minimum $NDWI_{MF}$ was greater than -0.4
Wrong vegetation trend	Tillering was not found between minimum NDVI and HD
Wrong flooding trend	Flooding was not detected between minimum $NDWI_{GAO}$ and T

Potential of the pixel-based rice dynamics identification and mapping for Management

The produced maps (Figures 33-36) show the capabilities of the proposed approach for enhancing management decisions at the regional level, although validation is needed. Phenology-based maps such as the HD and the Tillering date (*e.g.,* Figures 34-35) are a valuable resource for evaluating the evolution of the rice system under the climate change scenario, as well as serving as indicator of the effects of both environment and management practices on the development of rice, in the short-mid term. These key dates and the length of the period between them may be of importance for cultivar classification purposes, increasing the potential of satellite-based studies for supporting decision-making at regional level, through observation-driven methods. The use of the minimum $NDWI_{MF}$ as proxy for crop yield estimates (Figure 36) offers information in crop efficiency, which is crucial in crop management, mainly under a climate change scenario and the loss of productivity due to sea level rise and soil salinity increase. The intensity or yield potential of the individual fields, or even pixels, might be crucial in decision-making related to the reclassification of land-use or agricultural adaptation to fast weather changes and soil characteristics due to both climate change and human impacts.

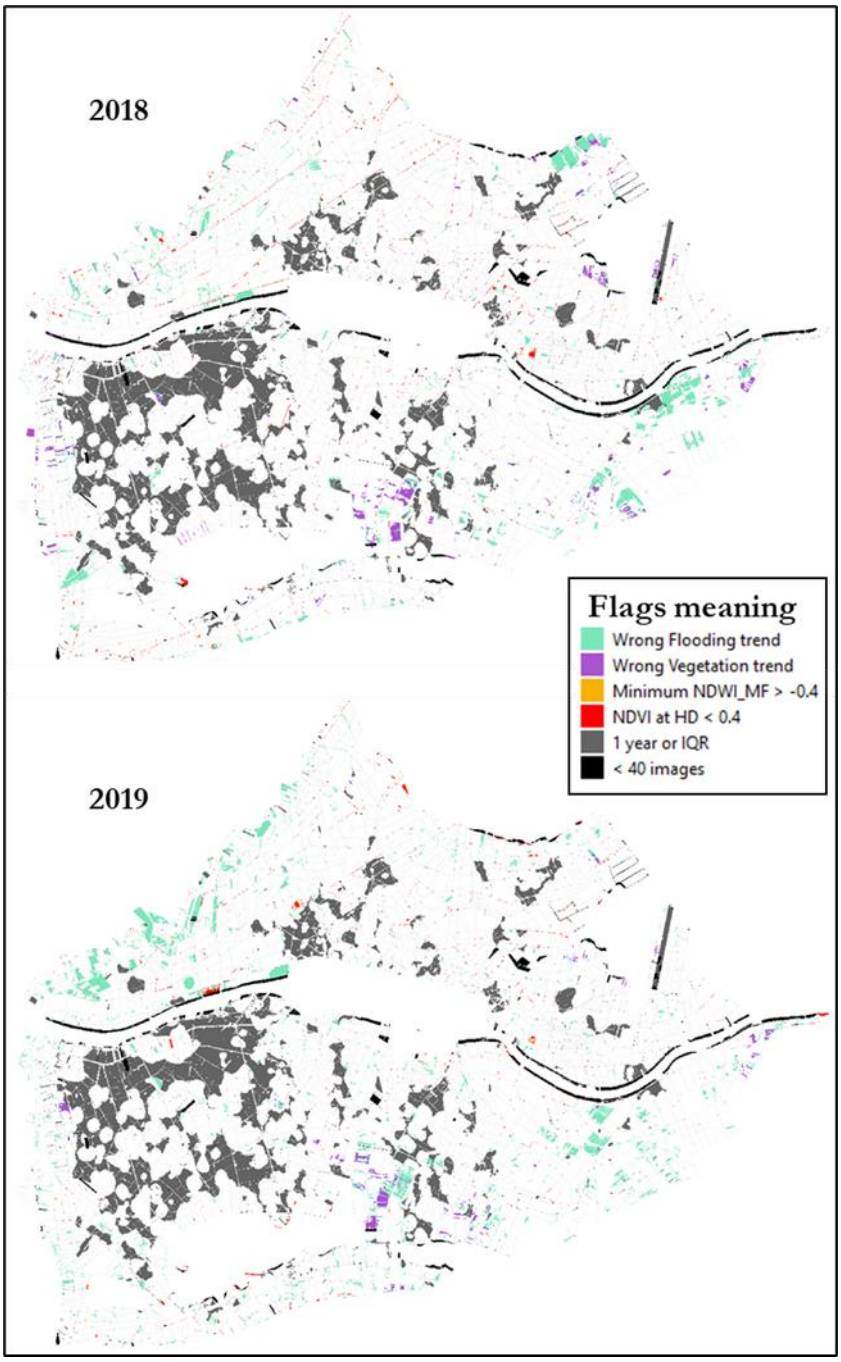

Figure 32. Flagged pixels in 2018 and 2019. Rice masks added for reference.

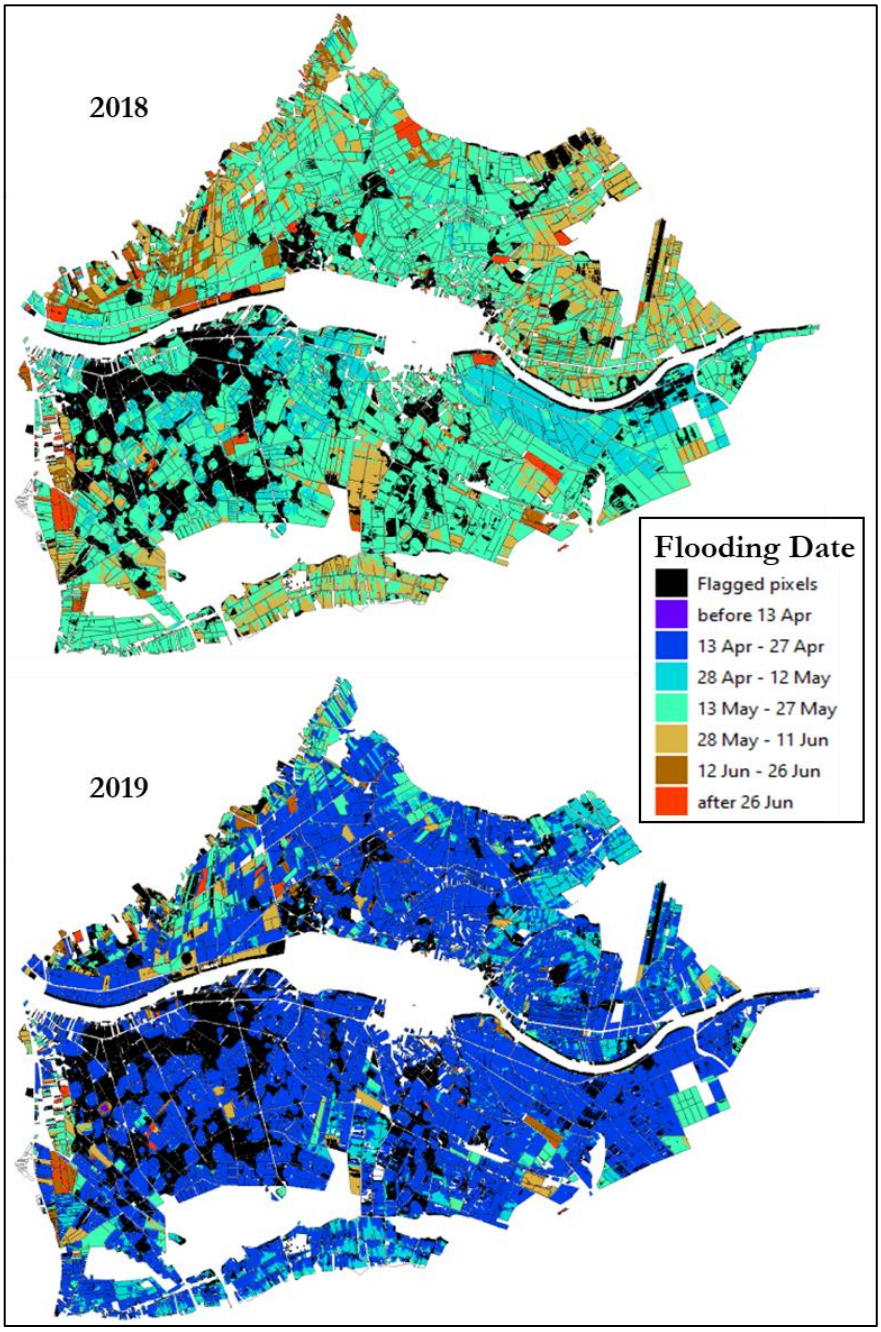

Figure 33. Flooding date in 2018 and 2019. Rice masks added for reference.

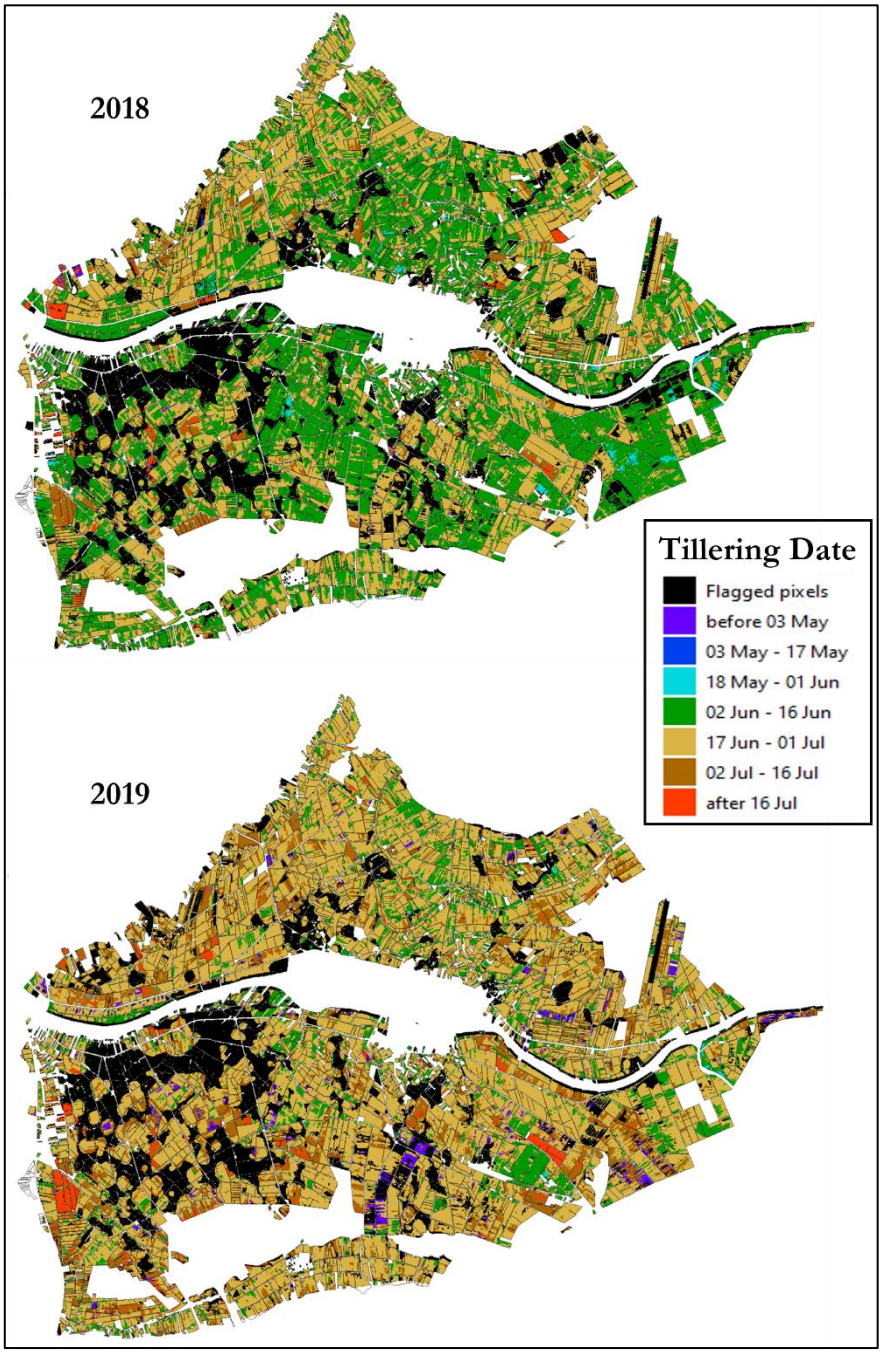

Figure 34. Tillering date in 2018 and 2019. Rice masks added for reference.

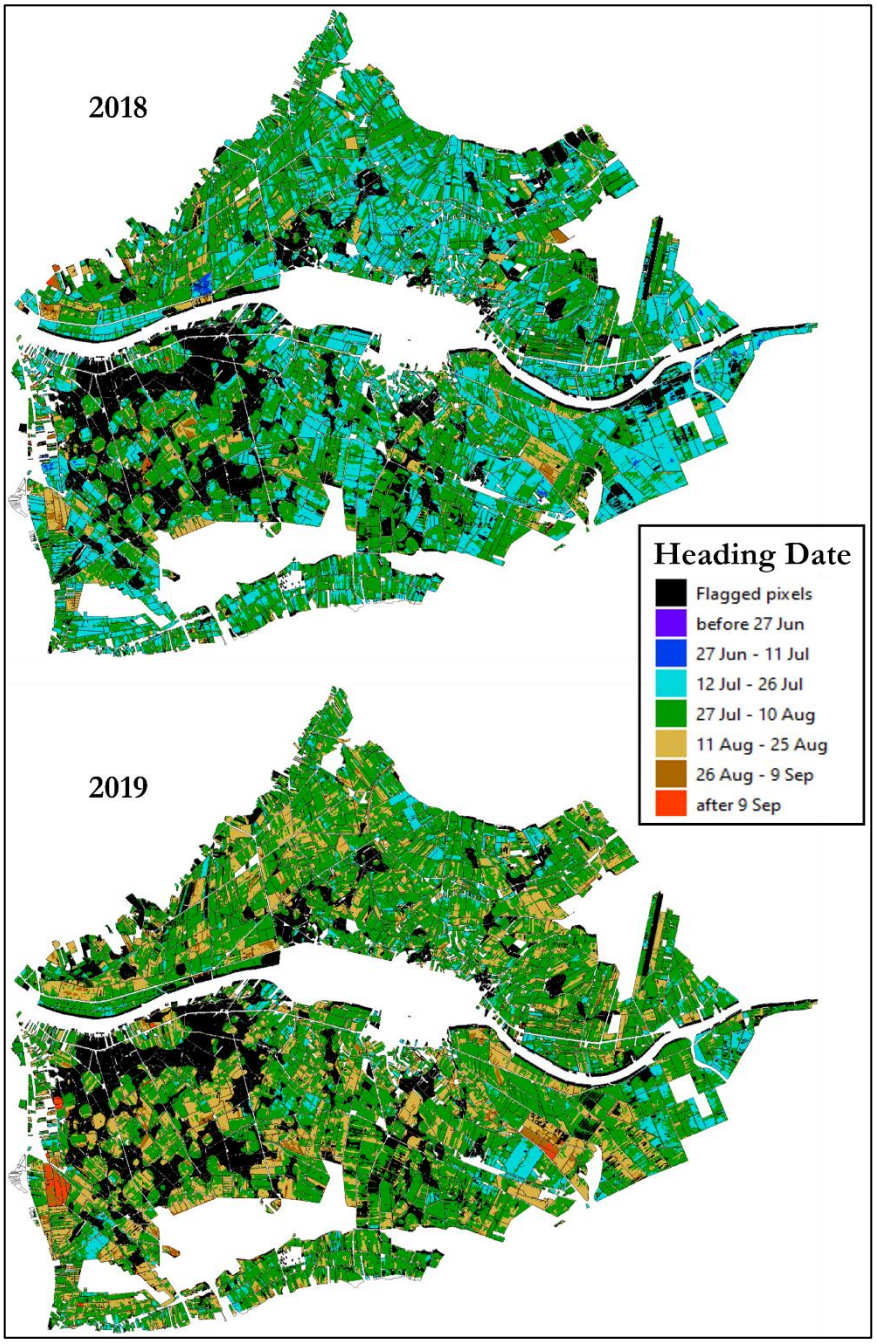

Figure 35. Heading date in 2018 and 2019. Rice masks added for reference.

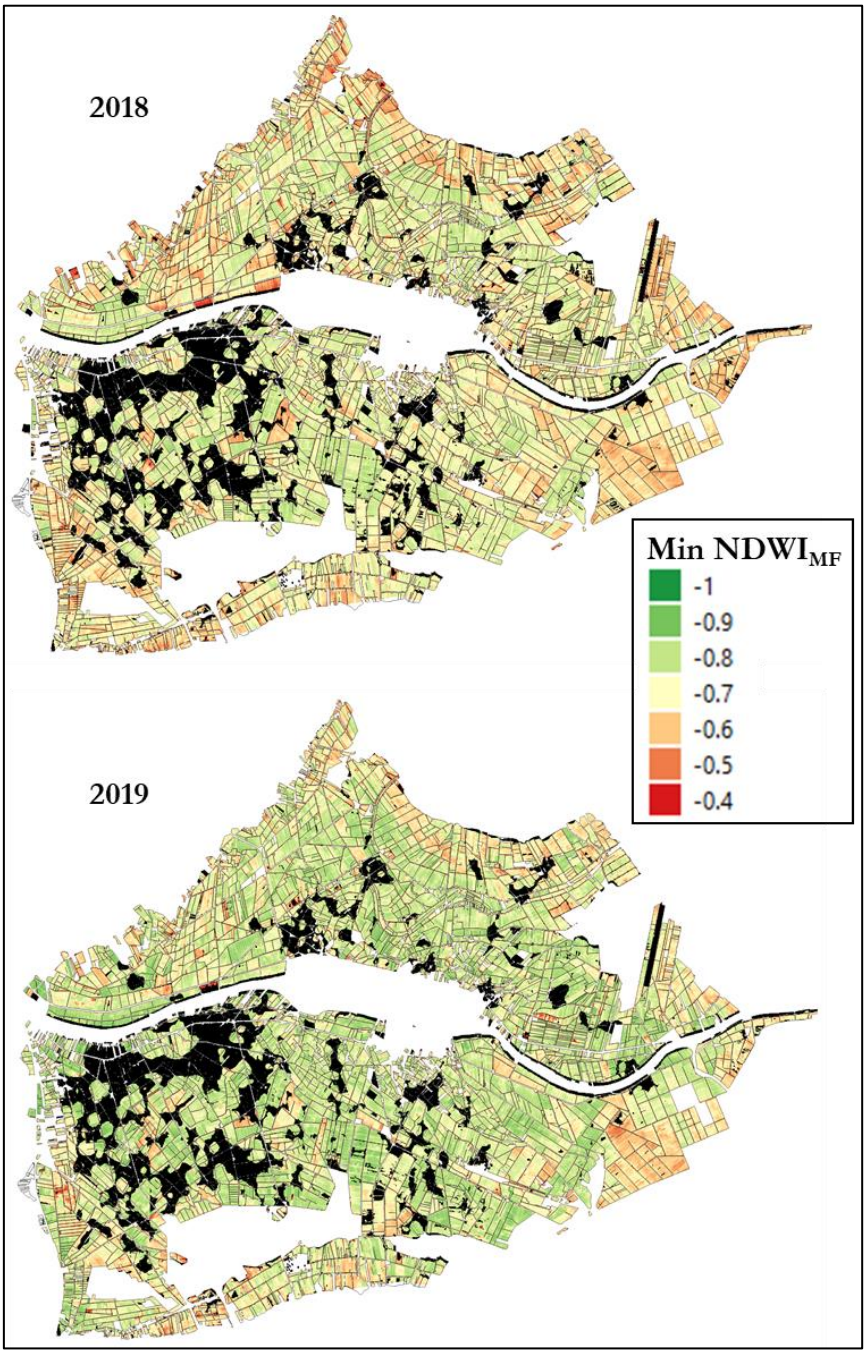

Figure 36. Minimum NDWI$_{MF}$ in 2018 and 2019. Rice masks added for reference.

4.5. CONCLUSION

Atmospheric conditions (*e.g.,* cloud presence) and differences in rice fields characteristics (*e.g.,* area, soil properties, management practices) increase the difficulty of using coarse resolution or low-frequency multispectral satellite data (*e.g.*, MODIS, Landsat) for the effective monitoring of agricultural practices and crop efficiency. For these purposes, in this study, we used three different spectral indexes (NDVI, $NDWI_{MF}$, $NDWI_{GAO}$) derived from Sentinel-2 (temporal frequency of 5 days). At different spatial scales, key rice farming features were identified (*i.e.,* Flooding, Tillering, Heading Date, Maturity, End of Flooding and Re-Flooding after harvest), thus defining the main phenological phases of the crops (*i.e.,* Vegetative Phase, Reproductive Phase, Maturity-Ripening Phase), identifying flooding regimes (flooded or dry), and producing accurate estimates of rice yield. However, few ground truth data were available and satellite data gaps due to cloud cover limited significantly the applicability of the method, restricting its capabilities in several fields. Further research must address these issues by increasing the density of satellite data (*e.g.,* multi-platform data, enhanced cloud, and shadows masking), and reference data, for fully assessing the accuracy of the proposed key features' extraction scheme and its extended applicability to all the Ebro Delta region and other similar areas (deltaic low-yielding rice systems).

Chapter 5

ATMOSPHERIC CORRECTION IN INLAND AND COASTAL WATERS

VALIDATION EXERCISE WITH SENTINEL-2 PROCESSORS

Edited version of:

Soriano-González, J., Urrego, E.P., Sòria-Perpinyà, X., Angelats, E., Alcaraz, C., Delegido, J., Ruíz-Verdú, A., Tenjo, C., Vicente, E., Moreno, J. Towards the combination of C2RCC processors for improving water quality retrieval in inland and coastal areas. *Remote Sensing*. 2022, 14, 1124.

Atmospheric correction is one of the main challenges for an accurate retrieval of water reflectance, deriving the water optical properties, estimating water quality parameters, and identifying submerged vegetation from satellite imagery. In Chapters 2 and 3, different atmospheric correction processors have been used (*i.e.,* ACOLITE, POLYMER), but the validation of the atmospheric correction performance was not possible due to the unavailability of above-water radiometry measurements. Evaluating the performance of the atmospheric correction and uncertainties is crucial for retrieving precise information from water spectral response, models development, and the generation of time series. It is particularly important in coastal and inland waters, for which there is not a standardized approach yet. This chapter focuses on the evaluation of the retrieval of remote sensing reflectance and key water quality parameters from S2, validated with a great field dataset of above-water radiometry and water quality measurements. The three currently available Case 2 Regional Coast Colour (C2RCC) atmospheric correction processors are assessed in 12 inland and coastal waters with varying water features (*i.e.,* Chlorophyll-a, TSM, Secchi disk depth). Potential use cases and the main constraints for a C2-Nets-based operational water reflectance retrieval and water quality monitoring are discussed. Results are of interest for both the ocean colour community and third-party end-users less familiarized with the processing of remote sensing data.

5.1. INTRODUCTION

The quality of inland and coastal waters is increasingly threatened by human-driven activities and climate change (Dörnhöfer *et al.*, 2018), requiring timely and accurate information on the water quality parameters to understand ecosystem dynamics (Kutser *et al.*, 2016) and achieve the Sustainable Development Goals (Mostert, 2003). Water quality involves the measurement of the concentration of many parameters, including phytoplankton biomass, total suspended matter, and water transparency. These are key indicators of changes in the water column that provide valuable information on, for instance, the trophic and ecological status, the nutrient surplus, and the particulate load in the water column (Gholizadeh *et al.*, 2016). Due to the high spatiotemporal variability, water quality monitoring requires frequent, global, and systematic measurements.

Accomplishing these demands, the new generation of Earth observation satellites such as Landsat and Sentinels constellations provide free systematic data with enhanced radiometric, spatial, and temporal resolutions with respect to the previous generation of Earth observation satellites. In particular, the Sentinel-2 satellites (S2A and S2B) operated by the European Space Agency (ESA) have opened up new potential for monitoring water quality in a wide range of geographical scopes (Toming and Kutser, 2016; Soriano-González *et al.*, 2019). However, achieving realistic and systematic water reflectance and, thus, water quality estimates from satellite remote sensing is challenging. Low reflectance of water in the visible–near infrared (VIS–NIR) regions of the spectrum (Bakker *et al.*, 2001) prevents water-

leaving reflectance from reaching more than 20% of the total reflectance sensed at the top of the atmosphere (TOA), while atmospheric contribution can reach up to 90% (IOCCG, 2010). Correcting the contribution of atmospheric constituents (such as gases and aerosols) in the captured images (radiance at the satellite sensor) for each date and location is a major issue in remote sensing of aquatic environments. Atmospheric correction is also challenged by additional effects such as the presence of sun glint (specular reflection of sunlight over water) or land adjacency (radiance from surrounding land affecting closest water pixels), which are complex to estimate and site-specific (Hoepffner and Zibordi, 2009). In coastal and inland waters these effects are frequently coupled with high variability and low covariance in optically active constituents. In these waters, classified as case-2, the inorganic and/or organic sediments make an important or dominant contribution to the optical properties (Gordon and Morel, 1983), requiring high accuracy and precision in the atmospheric correction algorithms to successfully retrieve water constituents.

Atmospheric correction in case-2 waters has not been solved yet. As a result, huge efforts have been made to develop atmospheric correction processors, covering a wide range of different methods (Pereira-Sandoval *et al.*, 2019; Warren *et al.*, 2019; Renosh *et al.*, 2020). However, the performance of the processors may differ depending on the scenario (sun and observation geometry, atmospheric, optical, and site-specific conditions), and there is no standardized approach yet, but atmospheric correction processors keep evolving as new approaches and more data become available. This makes it necessary to continue validating different atmospheric correction approaches as well as water quality retrieval methods with *in situ* data accounting for a wide variety of water types and environmental conditions.

The atmospheric correction Case 2 Regional Coast Colour (C2RCC) processor has been updated. The C2RCC is a development of the original Case 2 Regional processor (Doerffer and Schiller, 2007) adapted to different multispectral satellites (*e.g.,* Sentinel-2, Landsat-8). The most recent update (available since February 2021) includes a new processor trained for atmospheric correction in complex waters. The C2RCC thus currently accounts for three processors (*i.e.,* C2-Nets: C2RCC, C2X, and C2X-COMPLEX) using different training datasets within a neural network (NN) approach.

This study focuses on the validation of the remote sensing reflectance and key water quality parameters retrieved from Sentinel-2 Multispectral Imagery (S2-MSI) processed with the different C2-Nets. The validation datasets include *in situ* measurements of above-water radiometry (bottom of atmosphere reflectance, BOA), chlorophyll-a concentration ([Chl-*a*]) data as an indicator of phytoplankton biomass, total suspended matter ([TSM]) as an indicator of particulate load, and Secchi disk depth (Z_{SD}) measurements related to water transparency. The study areas comprise a set of 12 different inland reservoirs and transitional and coastal waters at the Eastern Iberian Peninsula (Spain). The objectives of the study were to:

(i) assess and compare the performance of C2-Nets for atmospheric correction of case-2 waters;

(ii) validate C2-Nets-derived water quality products (*i.e.,* [Chl-*a*], [TSM], and Z_{SD});

(iii) define potential use cases and main constraints for C2-Nets-based operational water quality monitoring.

5.2. MATERIALS AND METHODS

5.2.1. Study areas

Ten freshwater reservoirs (*ca.* 1 PSU), a coastal bay (Alfacs bay, *ca.* 35 PSU), and Pétrola, an endorheic saline lagoon (*ca.* 60 PSU) were included in this study (Figure 37); all of them are located in the Eastern Iberian Peninsula (Spain). The study areas have different altitudes with respect to the sea level and include diverse morphological and biophysical characteristics, covering a wide variety of trophic states (Table 10). The monitoring of water quality in these areas is challenging for remote sensing due to the complex and variable characteristics of these environments (*e.g.,* high spatiotemporal variability, small, shallow waters, and land adjacency effects).

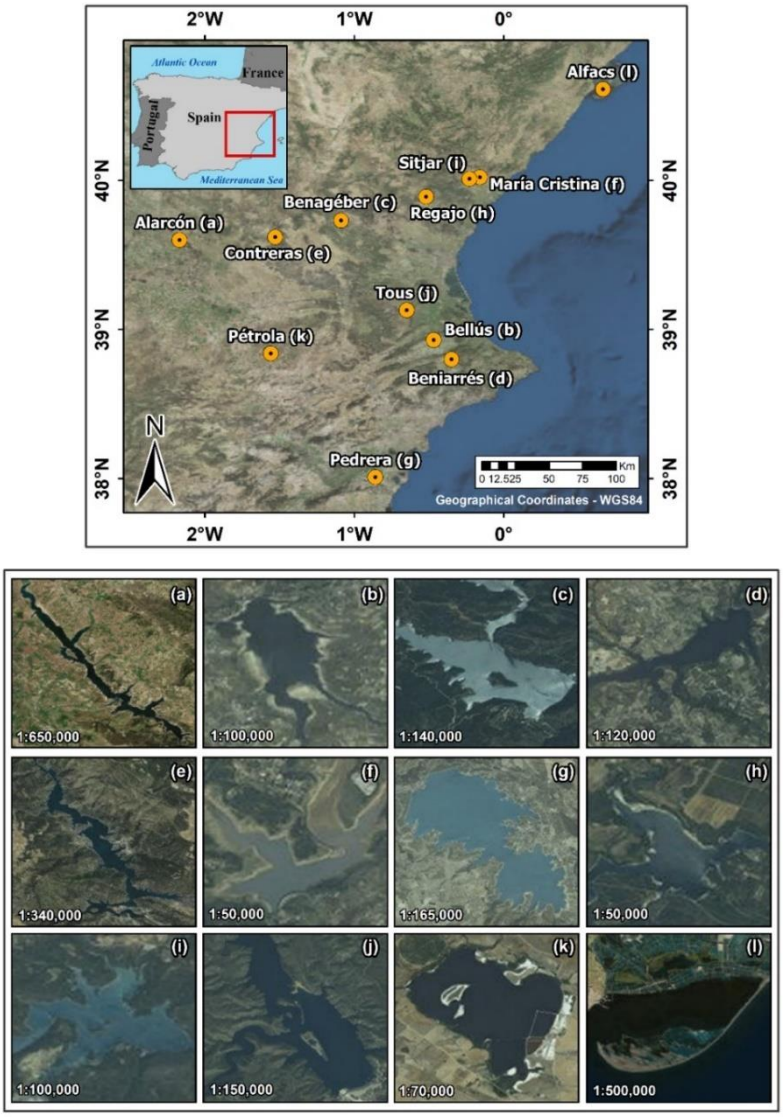

Figure 37. Study areas. Basemap source: Esri, DigitalGlobe, GeoEye, Earthstar Geographics, CNES/AIRbus DS, USDA, USGS, AeroGrid, IGN, and GIS User community.

Table 10. Descriptors of study areas by location, including the number of valid S2 images and *in situ* measurements (N_{xxx}), the altitude (elevation), surface, salinity, atmospheric pressure, ozone (O_3), and the ranges within S2 dates of [Chl-*a*], [TSM], and Z_{SD}.

Location	N Dates	Elevation (m)	Surface (km^2)	Salinity (PSU)	Pressure (hPa)	O_3 (DU)	N Radiometry	N [Chl-*a*]	[Chl-*a*] (mg/m^3)	N [TSM]	[TSM] (g/m^3)	N Z_{SD}	Z_{SD} (m)
Alarcón	2	814	68.4	1	1015.37±1.27	249.5±2.5	10	10	[1.1–5.26]	-	-	10	[1.75–4.6]
Bellús	3	159	8	1	1007±0.86	251.5±0.5	6	6	[13.86–68.01]	6	[18.66–22.13]	6	[0.45–0.63]
Benagéber	2	530	12	1	1011.56±0.18	263±14	7	6	[2.49–12.40]	6	[1.82–2.72]	6	[4–7.7]
Beniarrés	2	321	2.6	1	10150.39±1.85	269.5±11.5	6	6	[8.36–17.17]	6	[4.42–6.97]	6	[1.15–1.8]
Contreras	6	679	27.1	1	1008.57±5.91	257.5±22.5	23	21	[0.79–2.47]	15	[1.4–28.02]	21	[0.95- 7.3]
María Cristina	1	138	3.3	1	1004	245	2	2	[2.72–2.92]	2	[10.32–11.87]	2	0.75
Pedrera	1	111	12.7	1	1014.01	255	5	5	[0.86–1.19]	-	-	5	[2.95–3.25]
Regajo	3	407	0.8	1	1012.70±3.27	267.5±3.5	10	10	[4.03–10.21]	10	[2.95–9.12]	10	[0.95–4.25]
Sitjar	2	584	3.2	1	1009.78±5.78	260±15	4	4	[0.59–0.68]	4	[2.28–2.71]	4	[2.2–3.15]
Tous	4	163	9.8	1	1011.70±3.95	262±11	9	9	[0.58–1.72]	6	[0.67–1.13]	9	[6–9.1]
Alfacs	2	0	56	35	1005.56±5.78	246±3	9	9	[3.65–6.73]	-	-	9	[1.55–3]
Pétrola	1	852	3.4	60	1012.18±2.90	253±14	5	5	[77.58–309.2]	3	[142.27–162.33]	5	[0.17–0.45]
Total N	29	-	-	-	-	-	96	93	-	58	-	93	-

5.2.2. Field radiometry

Water-leaving radiance was obtained by the measurement of the above-water radiometry taken within a three-hour interval before or after the satellite pass. An ASD FieldSpec® HandHeld2 spectroradiometer and an Ocean Optics (HR 4000) spectrometer were used (Table 11). The measurement procedure to obtain water-leaving radiance was carried out following the methodology described by Mobley (1999), with a zenith angle of 40° and an azimuth angle of 135° to minimize sun-glint perturbations. For each point, five measurements of the water-leaving radiance and total downward irradiance were taken using a reflectance panel made of Spectralon® (25% nominal reflectance). With this data, remote sensing reflectance (Rrs) of each measurement (Table 10) was obtained according to Mobley (1999) and convolved to the S2-MSI spectral bands using the Sentinel-2 Spectral Response Functions (ESA S2-SRF v2.0).

Table 11. Spectroradiometers' specifications.

Instrument	Ocean Optics HR4000	ASD FieldSpec® HandHeld 2
Manufacturer	Ocean Optics, Inc; FL, Orlando, USA	Analytical Spectral Devices, Inc.; CO, USA
Acceptance angle	8°	8°
Spectral sampling interval	0.2 nm	1 nm
Spectral range	200–1100 nm	325–1075 nm

5.2.3. Water quality measurements

Water quality parameters included Secchi disk depth (Z_{SD}), chlorophyll-a ([Chl-*a*]), and total suspended matter [TSM] concentrations. The Z_{SD} data were measured by submerging the Secchi disk vertically and slowly into the water until it was no longer visible. The Z_{SD} was then defined as the maximum visible Secchi disk depth. For [Chl-*a*] determination, water samples were filtered through 0.4–0.6 μm GF/F glass fiber filters, extracted using standard methods (Shoaf and Lium, 1976), and calculated with Jeffrey and Humphrey's (1975) equations. The [TSM] was measured using the gravimetric method (APHA, 1998). All water quality measurements were carried out coinciding with above-water radiometry measurements, but not all types of *in situ* measurements were available for all dates and locations (Table 10).

5.2.4. Sentinel-2 data

The Sentinel-2 constellation consists of two satellites (S2A and S2B). Each one has on-board the MultiSpectral Instrument (S2-MSI). The S2-MSI TOA Level-1 (L1C) imagery includes information along 13 spectral bands centered at different

wavelengths (~443–2200 nm) and with different spatial resolutions of 10, 20, and 60 m (Table 12). A set of 30 S2-MSI TOA (L1C) cloud-free images were downloaded from Copernicus Access Hub coinciding with field radiometry measurements (Figure 38) and resampled to 20 m using the Graph Processing Tool (GPT) of the Sentinel Application Platform (SNAP v8.0).

Figure 38. Temporal line of cloud-free S2 A/B images matching field measurements by study area.

Table 12. S2A and S2B spectral bands, central wavelength (λ), spatial resolution, and application. Data from Copernicus Sentinel-2 MSI user guide. The field 'C2-Nets' indicates the spectral bands outputted by C2-Nets (Y = Yes, N = No).

Bands	ID	Spectral Region	Spatial resolution (m)	λ_{S2A} (nm)	λ_{S2B} (nm)	Bandwidth S2A - S2B (nm)	C2-Nets
B1	B443	Coastal aerosol	60	442.7	442.2	21 – 21	Y
B2	B490	Blue	10	492.4	492.1	66 – 66	Y
B3	B560	Green	10	559.8	559	36 – 36	Y
B4	B665	Red	10	664.6	664.9	31 – 31	Y
B5	B705	Red-edge1	20	704.1	703.8	15 – 16	Y
B6	B740	Red-edge2	20	740.5	739.1	15 – 15	Y
B7	B783	Red-edge3	20	782.8	779.7	20 – 20	Y
B8	B842	NIR	10	832.8	832.9	106 – 106	N
B8A	B865	NIR narrow	20	864.7	864	21 -22	Y
B9	B945	Water vapour	60	945.1	943.2	20 – 21	N
B10	B1620	SWIR / Cirrus	60	1373.5	1376.9	31 – 30	N
B11	B1620	SWIR1	20	1613.7	1610.4	91 – 94	N
B12	B2200	SWIR2	20	2202.4	2185.7	175 - 185	N

5.2.5. Atmospheric correction approaches

The Case 2 Regional Coast Colour is a development of the original Case 2 Regional processor (Doerffer and Schiller, 2007), based on a multi-sensor per-pixel artificial neural network (NN) method (Warren *et al.*, 2019). It processes TOA images of a variety of sensors, including S2-MSI, and generates atmospherically corrected images. The output data include Rrs, as well as a set of automatic products for water quality such as [Chl-*a*] (conc_chla) and [TSM] (conc_tsm), and the depth of the water column from which 90% of the water-leaving irradiance is derived (Kd_z90max).

The Case 2 Regional Coast Colour includes different processors (C2-Nets) which differ in the NN training ranges of inherent optical properties (IOPs; Table 13). The C2RCC-Net (here C2RCC) is the original net covering typical ranges of coastal IOPs. C2RCC was complemented with the CoastColour dataset to extend the range for coastal waters including extreme cases (Brockman *et al.*, 2016) resulting in the C2X-Net (C2X). The C2X-COMPLEX-Net (C2XC) was trained with intermediate ranges of IOPs, larger than C2RCC and tighter than C2X (ESA Step Forum). C2-Nets do not include specific correction for sun glint or land adjacency. The three C2-Nets were applied on all valid S2-MSI images (Figure 38) through the GPT of SNAP v8.0. The parametrization for the atmospheric correction of each image included: pressure (hPa) from NCEPR2 data (Kanamitsu *et al.*, 2002) and O_3 (DU) from AuraOMI data (NASA, 2018) downloaded for each location and date from the ocean data archive of NASA Ocean Color Data. Salinity (PSU) was estimated in each location by approximation with more frequent field measurements (Table 10). Despite the salinity of Pétrola being ~60 PSU (Table 10), it was set to 40 PSU, the maximum value accepted by the C2-Nets. Given the unavailability of water temperature measurements, it was left as default on all dates (15 °C). These site-specific parameters may influence atmospheric correction calculations introducing uncertainty in the estimation of the aerosol optical depth and are an inherent part in the C2-Nets NN processing (Brockman *et al.*, 2016); thus, it is recommended to consider them for reducing estimation uncertainty. For land/water segmentation, the valid pixel expression was set as a threshold on the SWIR band B11 (Table 12) of S2-MSI L1C images. The threshold ranged between 0.025 and 0.11, and it was heuristically defined for each location and date according to the trade-off between keeping the maximum number of pixels of interest (water pixels inside study areas) and the minimum noise (*e.g.,* mountain shadows, land). From each C2-Net, bands of TOA reflectance, remote sensing reflectance (Rrs), and Kd_z90max were extracted. The conc_chla and conc_tsm products were also generated, with the default factors and exponents (conc_chla = 21 ∗ a_pig ^ 1.04; conc_tsm = 1.72 ∗ b_part + b_wit ∗ 3.1). In addition, C2-Nets flags (Pereira-Sandoval *et al.*, 2019), which include codes for quality control of pixels, were exported.

Table 13. IOPs' training ranges of the C2-Nets.

IOPs (m^{-1})	Description	C2RCC	C2X	C2XC
a_pig	Absorption coefficient of phytoplankton pigments.	[≈0, 5.3]	[≈0, 51.0]	[≈0, 30.81]
a_det	Absorption coefficient of detritus.	[≈0, 5.9]	[≈0, 60.0]	[≈0, 17.0]
a_gelb	Absorption coefficient of gelbstoff (CDOM absorption).	[≈0, 1.0]	[≈0, 60.0]	[≈0, 4.25]
b_wit	Scattering coefficient of white particles (calcareous sediments).	[≈0, 60.0]	[≈0, 590.0]	-
b_part	Scattering coefficient of typical sediments.	[≈0, 60.0]	[≈0, 590.0]	-
b_tot	Scattering coefficient of typical sediment and white particles.	-	-	[≈0, 1000.0]

*adapted from Borckman *et al.* (2016) and ESA Step Forum

5.2.6. Match-up exercise

The match-up exercise was performed for the three C2-Nets Rrs separately and applied to each validation dataset (*i.e., in situ* Rrs, [Chl-*a*], [TSM], and Z_{SD}).

(i) A 3x3 pixel window, centered at the coordinates of *in situ* measurements, was extracted for each date and location, and C2-Nets were quality-checked in all extracted pixels by applying the recommended flags (Warren *et al.*, 2019). These quality flags indicate issues related to the scope of the training range of the used NN and/or cloudy conditions (Brockman *et al.*, 2016; Pereira-Sandoval *et al.*, 2019) and should be considered for reducing potential artifacts and uncertainty.

(ii) Flagged pixels, as well as pixels with negative Rrs at bands B443, B490, B560, and B665 (Table 12), were removed from the analysis (Cui *et al.*, 2010), and the number of remaining pixels within each pixel window was checked. Windows with fewer than 5 remaining pixels were removed from the analysis.

(iii) Outliers were defined through boxplot analysis applied separately to each pixel window and available spectral bands (B443-B783 and B865; Table 12).

(iv) Pixels with outliers in any of the bands were removed. The number of pixels within the pixel windows was revised once more, and those with fewer than 5 pixels remaining were removed from the analysis.

(v) The coefficient of variation (CV in Equation 14) of B560 was computed for each remaining pixel window, removing those with $CV > 15\%$ (Cui *et al.*, 2010).

$$CV = \sigma / \bar{x} * 100 \quad (14)$$

where σ is standard deviation and $\bar{x}$ is the mean.

5.2.7. Performance assessment of C2-Nets

From the validation dataset to the analysis of the performance of the C2-Nets, the workflow is summarized in Figure 39.

5.2.7.1 Validation of remote sensing reflectance (Rrs)

Validation of Rrs was broadly based on the scoring scheme proposed in (Müller *et al.*, 2015). However, match-up criteria and the number of statistics differed. In addition, all available C2-Nets spectral bands (Table 12) were included, validated, and used for the ranking in this study. The assessment was carried out with the maximum possible number of match-ups for each C2-Net.

The scoring scheme extends the common validation strategy of comparisons between above-water measurements and satellite spectral bands by a ranking system.

(i) Bands scoring

For each C2-Net Rrs and TOA reflectance band, a set of 5 statistical parameters and their 95% confidence intervals were calculated for each available spectral band independently. The Root Mean Squared Error (*RMSE*), the Relative *RMSE* ($RMSE_{rel}$), the Bias, the *RMSE* of the Residual Error ($RMSE_{RE}$), and the Pearson's *r*, were computed and transformed into relative scores as in (Müller *et al.*, 2015), evaluating the relationship of quality dependent on the C2-Net. For scoring purposes, Bias was used in absolute terms ($|Bias|$) and *r* was transformed to a negative orientated value ($1-r$). The *RMSE*, $RMSE_{rel,}$ and $RMSE_{RE}$ were used directly. To each property, the evaluation scores were assigned by band separately. The C2-Net with the smallest value in the statistical property received 2 points. Then, if a value corresponding to another C2-Net fell within the confidence interval of the best, this C2-Net received 2 points as well. If the value of a C2-Net was outside the confidence interval of the best but their confidence intervals overlapped, this algorithm received 1 point. Else, the C2-Net was given 0 points. See Müller *et al.* (2015) for detailed information on the scoring-based method.

(ii) Spectral shape fitting

First, the spectral bias was removed by normalizing *in situ* and satellite-a-derived spectra to 560 nm (B560 in S2) before the evaluation. Chi-square tests (χ^2) of the *in situ* and C2-Nets-derived spectral shapes (including all available C2-Nets bands) were conducted for each match-up, and the percentage of chi-square values lower than the 95% confidence level ($N\chi^2_{95}$) was calculated. Finally, the mean χ^2 ($\overline{\chi^2}$) for each C2-Net Rrs and TOA match-ups were derived.

(iii) Match-up efficiency

The relative number of valid match-ups (R_{matchs}) was calculated as the ratio between the valid observations after the match-up exercise for each C2-Net and the potential initial match-ups with *in situ* radiometry

5.2.7.2 Validation of water quality products

The conc_chla and conc_tsm derived from C2-Nets with default factorization were validated with *in situ* [Chl-*a*] and [TSM]. The performance metrics selected for these parameters were the Mean Average Error (*MAE*; Equation 15), the Root Mean Squared Error (*RMSE*; Equation 16), the Bias (Equation 17), and the Pearson's *r* (*r*). The kd_z90max is a variable strongly correlated with the Z_{SD} (Poole and Atkins, 1929; Holmes, 1970), however, being different variables, only the *r* was used for the comparison with the measured Z_{SD}. In addition, the coefficient of determination (R^2), the slope (*m*), and intercept (*b*) of linear regression were calculated.

$$MAE = \frac{1}{N}\sum_{i=1}^{N}|M_i - O_i| \quad (15)$$

$$RMSE = \sqrt{\sum_{i=1}^{N}\frac{(M_i - O_i)^2}{N}} \quad (16)$$

$$BIAS = \frac{1}{N}\sum_{i=1}^{N}(M_i - O_i) \quad (17)$$

where M_i are the estimated values from C2-Nets and O_i the field measured ones.

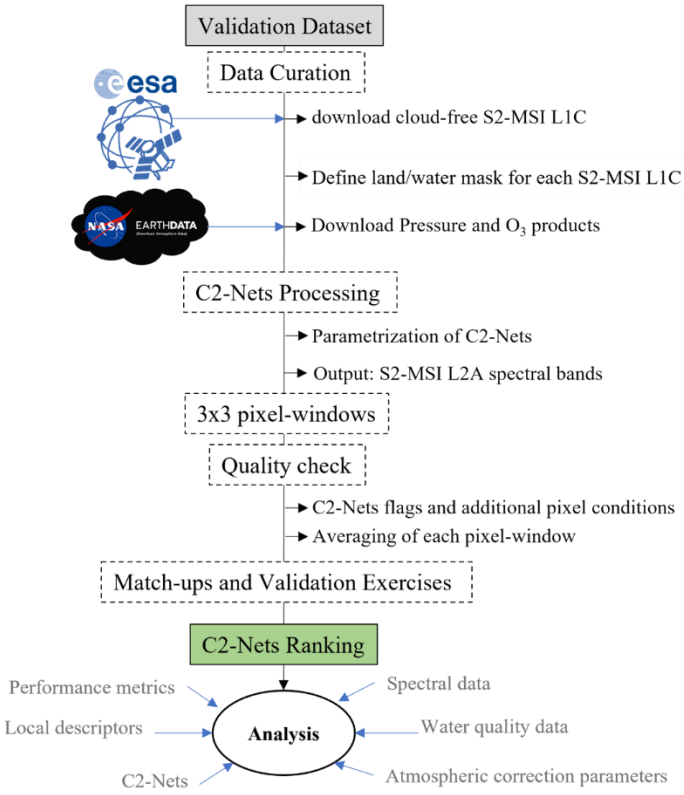

Figure 39. Workflow.

5.3. RESULTS

5.3.1 *In situ* water quality

The inclusion of different locations and dates involved wide ranges of water quality (Table 14). Most of the measurements corresponded to [Chl-*a*] < 3 mg/m³ and [TSM] < 4 g/m³ (median in Table 14). Minimum [Chl-*a*] and [TSM] (0.58 mg/m³ and 0.74 g/m³) were found in the Tous reservoir related with maximum Z_{SD} (9.1 m). Contrarily, maximum [Chl-*a*] and [TSM] (309.62 mg/m³ and 162.33 g/m³) were associated with the minimum Z_{SD} (0.17 m) in the hypertrophic salty lagoon of Pétrola.

Table 14. Number of water quality measurements by type (*N*), their concentration ranges (Min, Max), median, mean and standard deviation (σ).

WQ parameters	*N*	*Min*	*Max*	*Median*	*Mean*	σ
[Chl-*a*] (mg/m³)	93	0.58	309.6	2.72	20.55	61.5
Z_{SD} (m)	93	0.17	9.10	3.00	3.34	2.4
[TSM] (g/m³)	58	0.67	162.3	3.65	13.70	33.5

5.3.2 Match-ups exercise

The match-up exercise was carried out in a strict manner, thus maximizing the quality of the performance of each C2-Net. After the quality check, the number of match-ups was reduced by between ~12% to ~66% depending on the C2-Net and the type of *in situ* measurement (Figure 40). Most of the rejected match-ups were due to pixel windows having $CV > 15\%$ in B560. For all *in situ* datasets, a higher number of valid match-ups was found with C2RCC, while the lowest number was found for C2X (Figure 40).

5.3.3 Validation of Rrs

Comparing C2-Nets, disregarding the different number of match-ups, the bands' statistical results (Table 15) were translated into the similar scoring of C2RCC and C2XC in B443-B490, highest scoring of C2RCC in B560-B665, highest scoring of C2XC in B705-B783, and C2X ranking first in B865 (Figure 41a). Despite the winner's variability in single bands scoring, C2XC was the unique C2-Net scoring at all bands, ranking first in the total band score (Figure 41b). C2X did not score in B665 and C2RCC and did not achieve any point from B740-B865 (Figure 41a).

In general terms, all C2-Nets tended to underestimate Rrs of blue and green bands, with most of the errors within the [−50, 50]% interval (Figure 42). Relative errors were more dispersed between B665-B865 and C2XC, and C2X clearly improved C2RCC in cases with greater NIR Rrs (Figure 42). These led to better fitting of C2X and C2XC Rrs in NIR wavelengths (Figure 43) and contributed to making C2XC

(which included higher relative number of match-ups with greater NIR Rrs) the most capable of retaining the spectral shape with $\overline{\chi^2}$ closest, to 0 ($\overline{\chi^2} = -0.02$) and maximum $N\chi^2 = 1$ (Figure 41b). However, with C2RCC more radiometry match-ups (85%) were kept than with C2XC (53%) and C2X (33%). Match-ups with high reflectance pixels with peaks in B560 and B705 and/or greater NIR Rrs were more susceptible to rejection with C2RCC (*e.g.,* Pétrola in Figure 44g), and potential match-ups related to more clear waters with lower Rrs along the spectrum and/or a single peak in B560 were more likely rejected with C2X and C2XC (*e.g.,* Tous in Figure 44f). This was visible even from TOA reflectance (Figure 45), although all C2-Nets included match-ups with different types of spectrums (*e.g.,* Figure 44a,c).

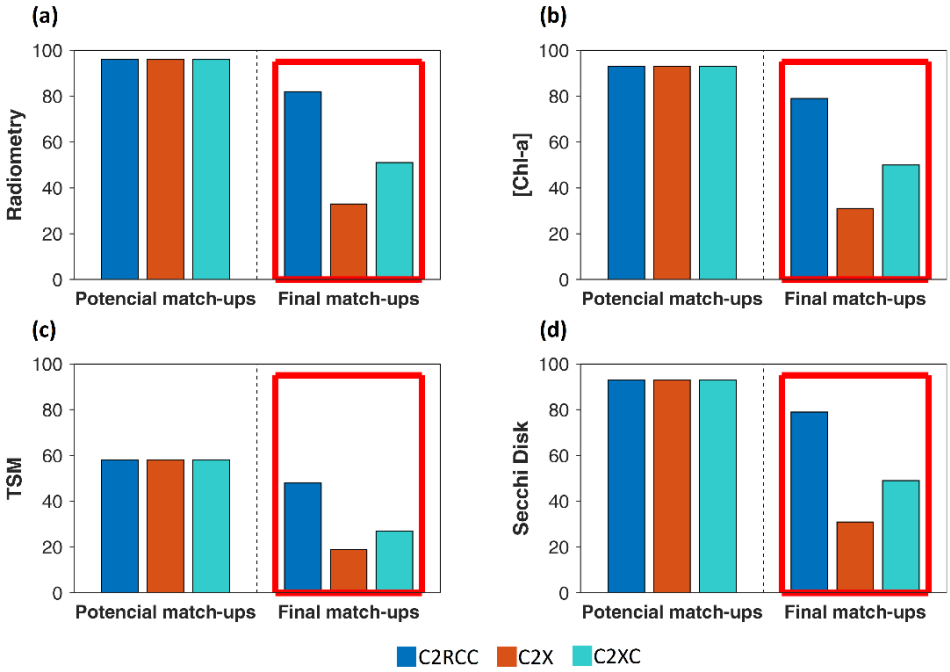

Figure 40. Match-up exercise by sub-dataset and C2-Nets: (a) Radiometry, (b) [Chl-*a*], (c) [TSM], (d) Secchi disk. Final match-ups for each C2-Net are highlighted with a red square.

Table 15. Band statistics for TOA and Rrs derived from C2-Nets datasets. Best results for each band and statistic are highlighted.

C2Net	Band	*RMSE*	$RMSE_{rel}$	$RMSE_{RE}$	*|BIAS|*	*r*
C2RCC_TOA	B1	0.1260	30.900	0.0139	0.1250	0.615
C2RCC_Rrs		0.0043	0.548	0.0030	0.0031	0.817
C2X_TOA		0.1250	20.200	0.0109	0.1240	0.672
C2X_Rrs		0.0052	0.4970	0.0044	0.0029	0.568
C2XC_TOA		0.1250	28.200	0.0159	0.1240	0.682
C2XC_Rrs		0.0036	0.806	0.0035	0.0004	0.739

Table 15. (continued).

C2Net	Band	*RMSE*	$RMSE_{rel}$	$RMSE_{RE}$	*|BIAS|*	*r*
C2RCC_TOA	B2	0.1020	14.850	0.0193	0.0997	0.639
C2RCC_Rrs		0.0051	0.552	0.0036	0.0036	0.853
C2X_TOA		0.1010	10.300	0.0140	0.0998	0.717
C2X_Rrs		0.0059	0.476	0.0049	0.0033	0.728
C2XC_TOA		0.1030	14.100	0.0207	0.1006	0.642
C2XC_Rrs		0.0041	0.886	0.0041	0.0000	0.814
C2RCC_TOA	B3	0.0819	8.490	0.0235	0.0785	0.740
C2RCC_Rrs		0.0047	0.587	0.0040	0.0025	0.894
C2X_TOA		0.0849	5.720	0.0189	0.0828	0.794
C2X_Rrs		0.0062	0.517	0.0061	0.0010	0.747
C2XC_TOA		0.0861	8.290	0.0226	0.0831	0.635
C2XC_Rrs		0.0051	0.921	0.0050	0.0003	0.809
C2RCC_TOA	B4	0.0557	20.720	0.0252	0.0496	0.517
C2RCC_Rrs		0.0022	0.543	0.0017	0.0014	0.972
C2X_TOA		0.0551	11.080	0.0212	0.0509	0.720
C2X_Rrs		0.0039	0.600	0.0038	0.0006	0.863
C2XC_TOA		0.0579	20.600	0.0251	0.0522	0.332
C2XC_Rrs		0.0018	0.710	0.0018	0.0000	0.921
C2RCC_TOA	B5	0.0519	29.300	0.0262	0.0449	0.581
C2RCC_Rrs		0.0036	0.560	0.0033	0.0015	0.845
C2X_TOA		0.0524	14.226	0.0237	0.0467	0.798
C2X_Rrs		0.0026	0.793	0.0026	0.0004	0.949
C2XC_TOA		0.0593	29.300	0.0283	0.0520	0.690
C2XC_Rrs		0.0024	0.753	0.0024	0.0004	0.985
C2RCC_TOA	B6	0.0467	78.200	0.0257	0.0391	0.282
C2RCC_Rrs		0.0014	4.690	0.0014	0.0005	0.741
C2X_TOA		0.0422	42.000	0.0209	0.0367	0.476
C2X_Rrs		0.0007	0.761	0.0006	0.0004	0.975
C2XC_TOA		0.0508	86.300	0.0263	0.0435	0.347
C2XC_Rrs		0.0013	0.673	0.0012	0.0004	0.990
C2RCC_TOA	B7	0.0468	65.640	0.0268	0.0384	0.281
C2RCC_Rrs		0.0014	4.332	0.0013	0.0004	0.728
C2X_TOA		0.0423	40.990	0.0222	0.0361	0.460
C2X_Rrs		0.0009	0.753	0.0007	0.0005	0.977
C2XC_TOA		0.0506	84.802	0.0272	0.0427	0.289
C2XC_Rrs		0.0007	0.576	0.0007	0.0001	0.996
C2RCC_TOA	B8A	0.0430	246.000	0.0274	0.0332	0.194
C2RCC_Rrs		0.0007	0.635	0.0006	0.0004	0.694
C2X_TOA		0.0371	55.900	0.0224	0.0296	0.313
C2X_Rrs		0.0004	0.659	0.0003	0.0001	0.957
C2XC_TOA		0.0455	291.000	0.0277	0.0361	0.077
C2XC_Rrs		0.0006	0.591	0.0005	0.0003	0.985

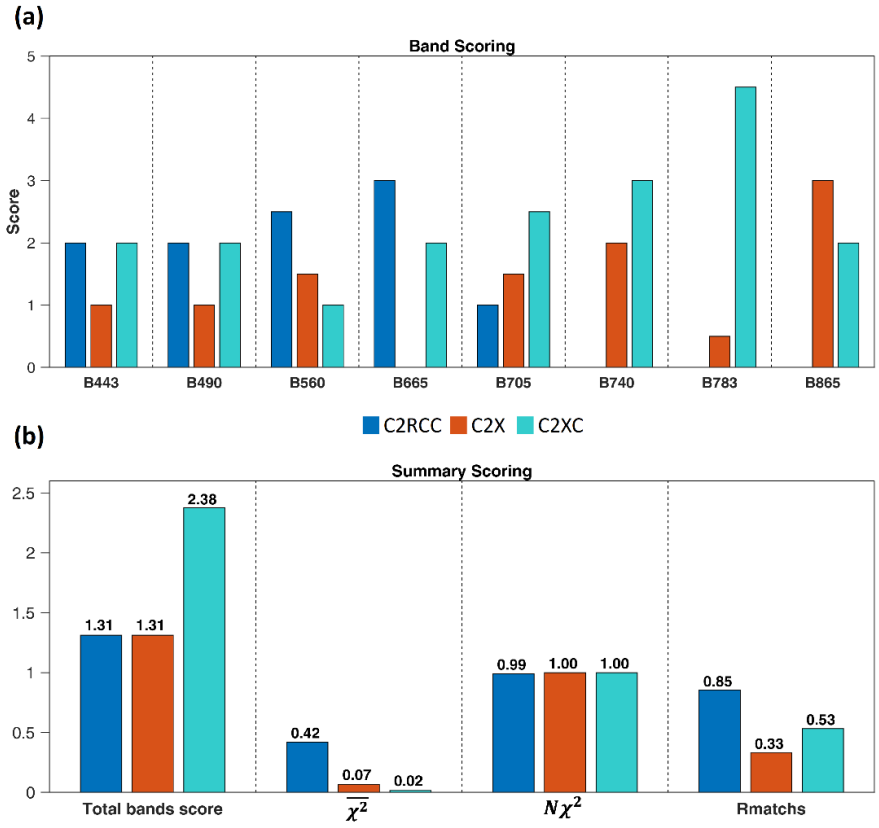

Figure 41. (a) Band Scoring per C2-Nets Rrs. (b) Summary of the Validation of Rrs. For representation, $\overline{\chi^2}$ is presented in absolute values and all bands'scores have been summed and divided by the number of available bands (N_{bands} = 8) for computing the Total bands' score.

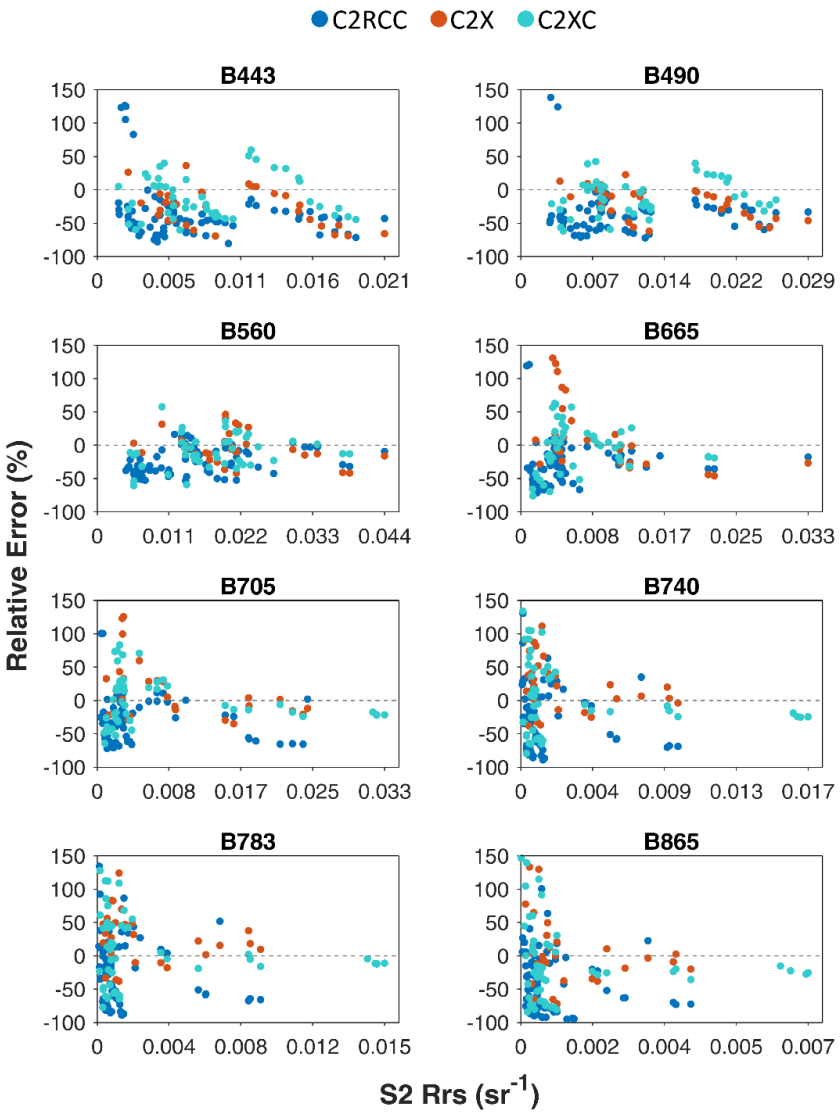

Figure 42. The relative error between measured and C2-Nets derived Rrs at all available spectral bands for each C2-Nets. Relative error was computed for representation as [(measured Rrs - C2-Nets Rrs)/measured Rrs × 100].

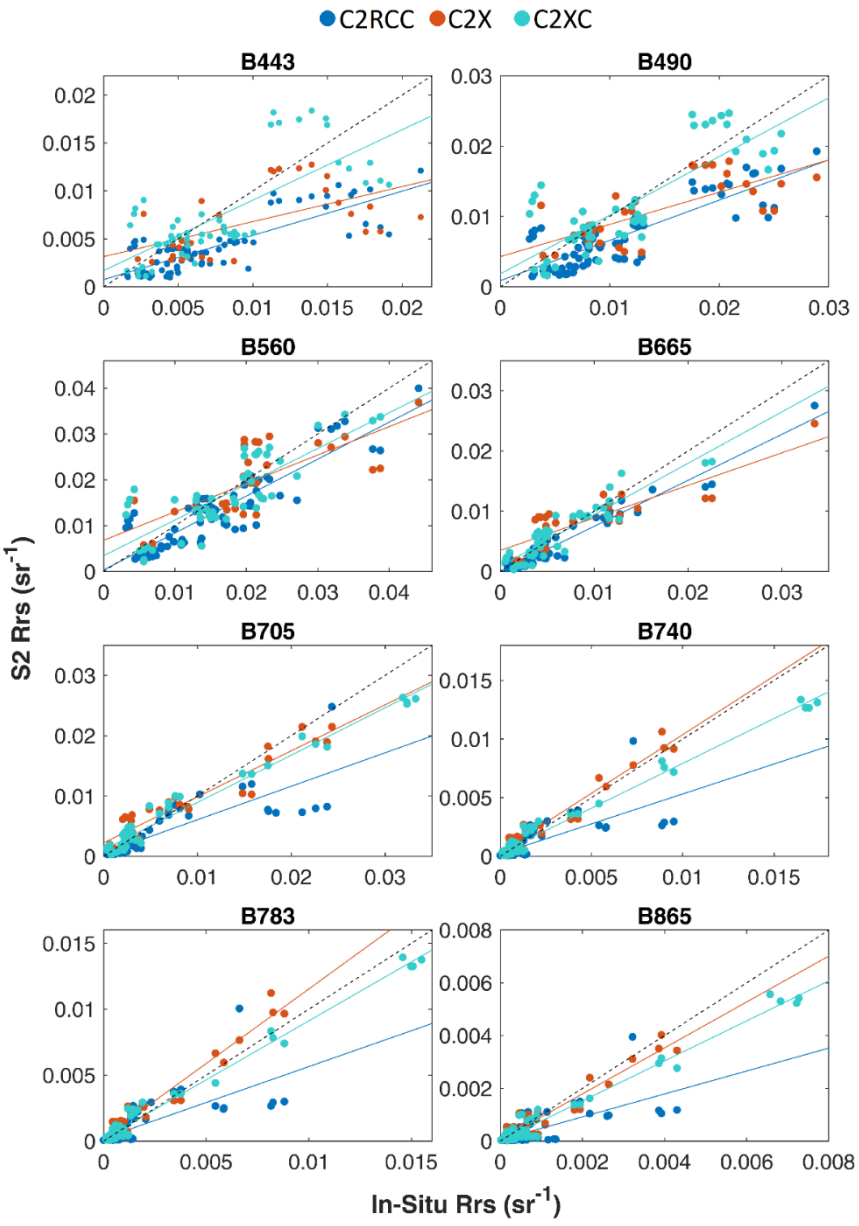

Figure 43. Scatter plots between measured and C2-Nets estimated Rrs at all available spectral bands. Dashed line corresponds to reference (1:1) line.

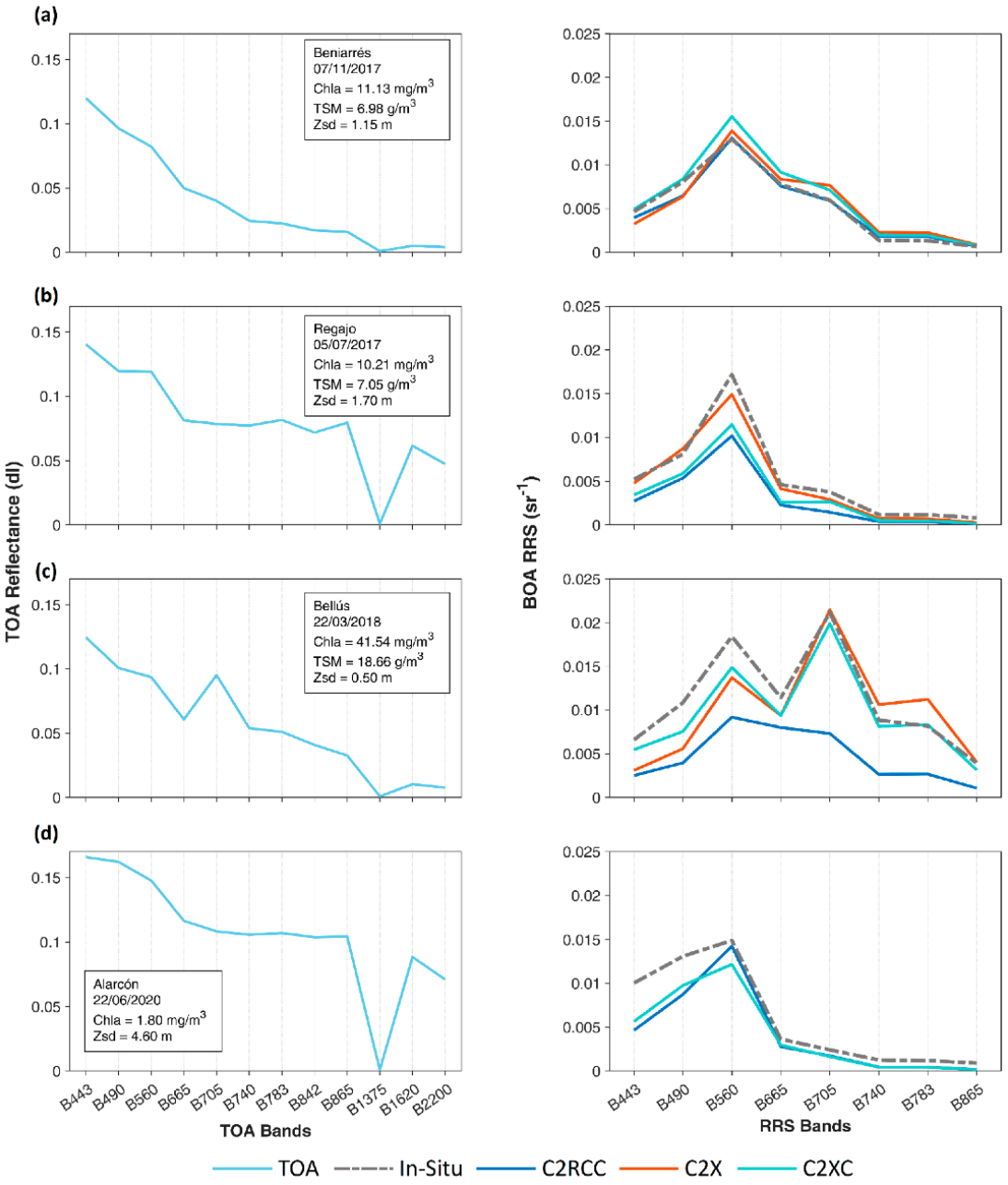

Figure 44. TOA reflectance spectrums (left column) and *in situ* and C2-Nets estimated Rrs (right column) for different scenarios (a-h). Availability of C2-Nets Rrs depends on the pixel flagging criteria described in the paper.

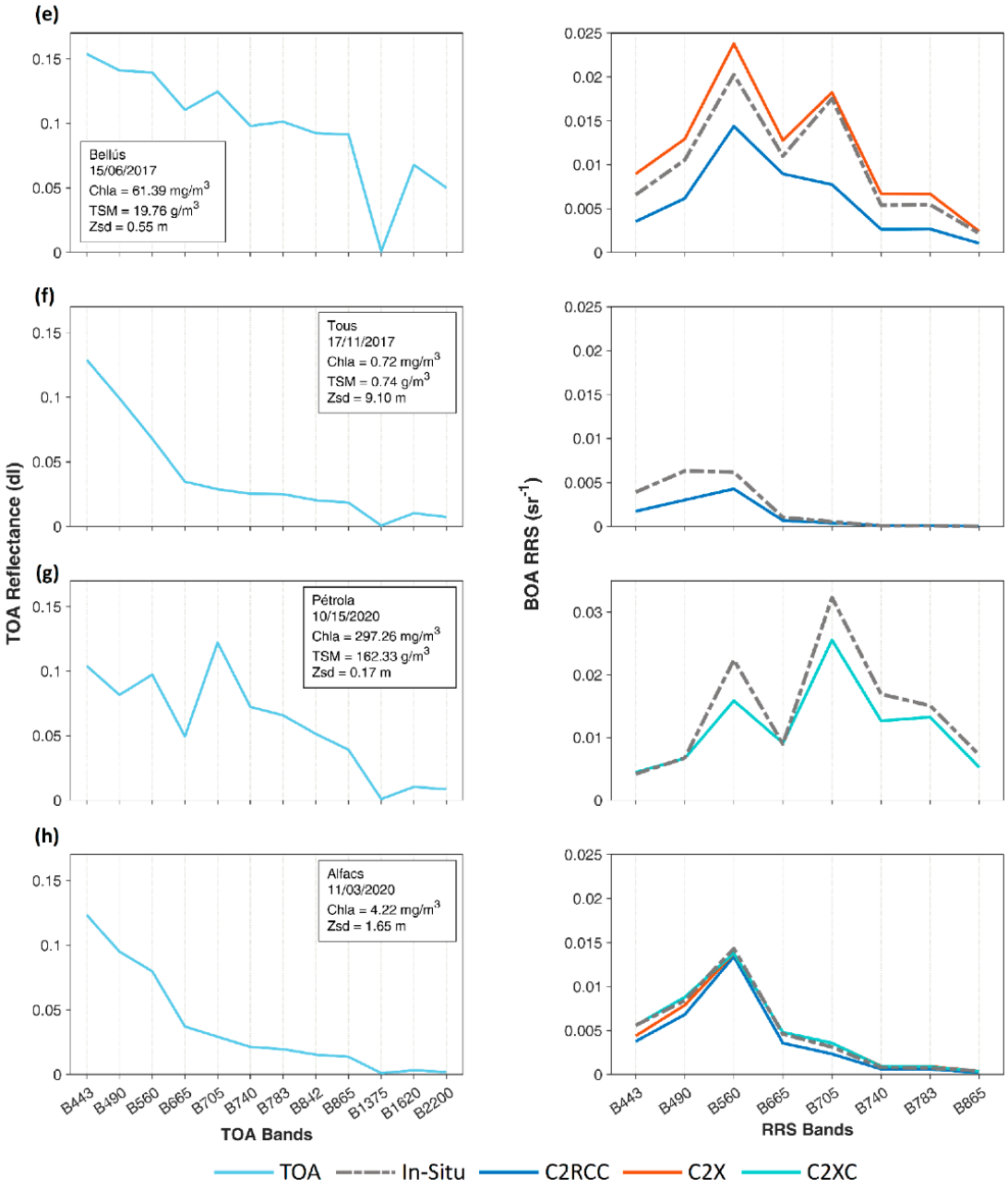

Figure 44. (continued).

Exploring the relation of the performance of C2-Nets with TOA reflectance, a k-means classification (4 classes) was conducted including TOA reflectance, *in situ* Rrs, and C2-Nets Rrs separately for C2-Nets (Figure 46). Clusters found for different C2-Nets were grouped by similarity (proximity) in cluster centers. In general terms, the clusters C1 and C4 (Figure 46) grouped those pixels with TOA and C2-Nets peaks at 560 and 705 nm, frequently associated with increasing NIR Rrs (*e.g.,* Figure 44b,d,e). Clusters C* and C** fit in the same category, although the small numbers of match-ups (Figure 46a) mainly highlight the trends of four locations and dates which were included in C1 or C4 with the C2RCC dataset (*e.g.,* Figure 44c) or only accepted with C2XC (Figure 44g).

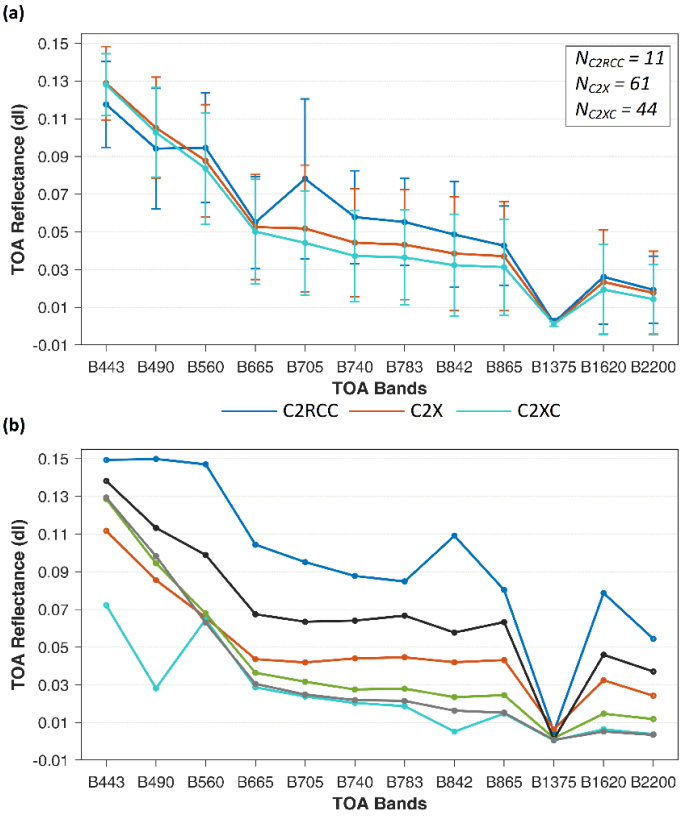

Figure 45. (a) Mean (lines) and standard deviation (bars) of TOA reflectance spectrums describing, by C2-Net, the set of rejected pixels during the match-ups exercise steps ii-v; (b) Mean TOA spectrums of rejected pixels in all C2-Nets. Rejected pixels by the C2-Nets flags are not included.

The C3 class grouped more than 50% of the valid match-ups of the three C2-Nets (Figure 46a), including smoother TOA reflectance spectrums generally related to lower NIR Rrs and/or presence of a single/dominant C2-Nets B560 peak (*e.g.,* Figure 44f,h). The match-ups of the C2 class were only included with C2RCC and

C2XC (Figure 46), and all of them correspond to the same location and date. These spectrums were characterized by high TOA reflectance in all spectral regions (Figure 46a), including relatively high SWIR reflectance (Figure 44d), although the *in situ* Rrs was similar to the measurements in C3 (Figure 46b).

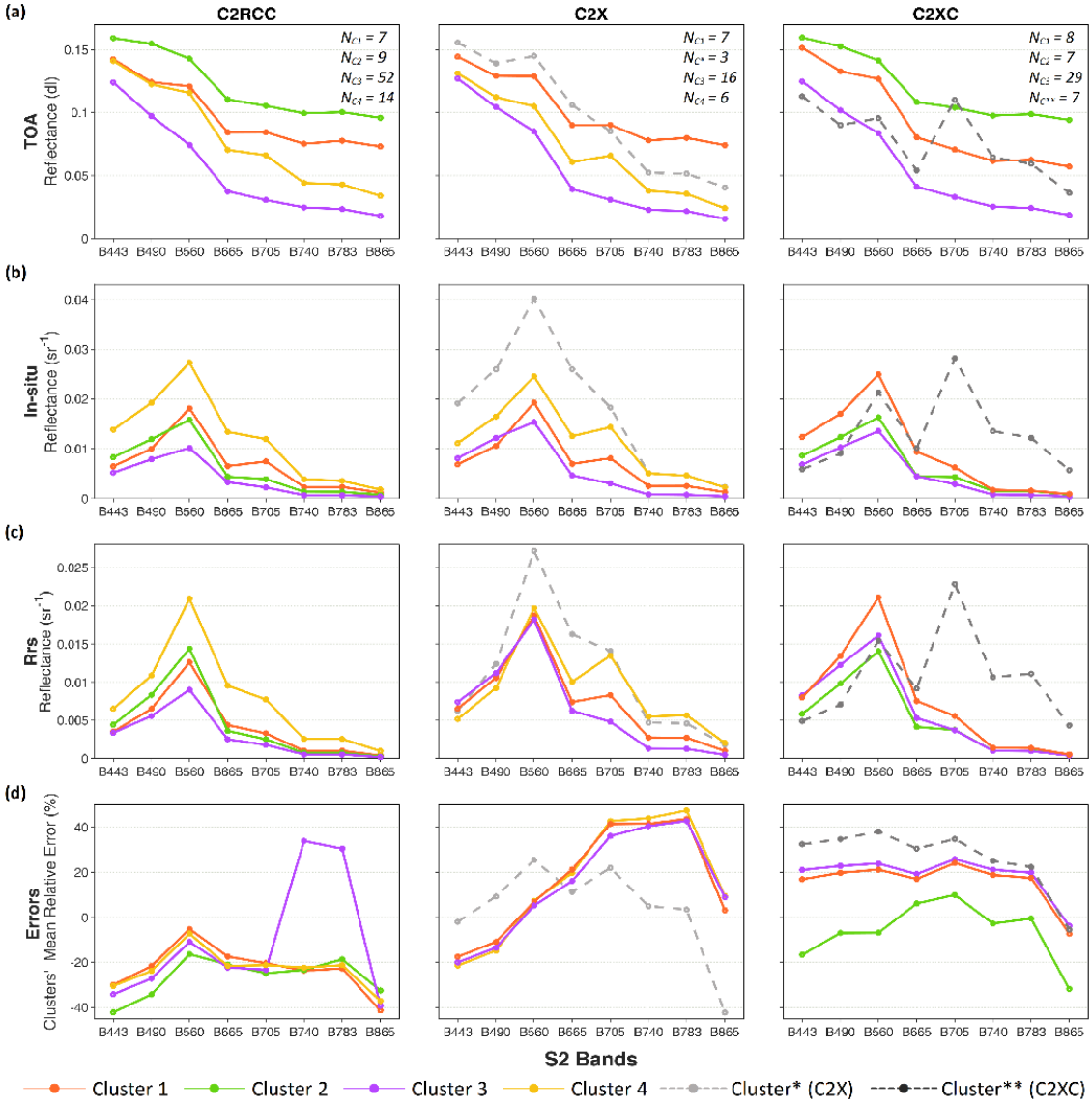

Figure 46. *K*-means clustering including TOA reflectance, measured and C2-Nets derived Rrs (a-c). Lines represent, by C2-Nets (columns), clusters centres for (a) TOA reflectance; (b) *in situ* Rrs, (c) C2-Nets Rrs and, (d) mean relative error of cluster members' *in situ* and C2-Nets Rrs. For ease of representation, clusters have been coloured according to the similarity between C2-Nets classes.

5.3.4 Validation of water quality

For [TSM] and [Chl-*a*], the *MAE*, *RMSE*, *Bias,* and Pearson's *r* analysis were conducted. For assessing the Kd_z90max and Z_{SD} relationship, only Pearson's *r* was calculated. Both for [TSM] and [Chl-*a*], C2RCC achieved the lowest *MAE* and *RMSE*, with *BIAS* closest to 0, followed by C2X and C2XC (Table 16). However, the C2XC dataset included extreme measured [Chl-*a*] and [TSM] (Table 16), for which high underestimation was observed (Figure 47a,b). Such extreme match-ups had a high impact on C2XC-derived *MAE*, *RMSE,* and *Bias* (Table 16), but higher relationships between measured and derived [Chl-*a*] ($r = 0.94$) and [TSM] ($r = 0.81$) from the C2XC dataset were observed (Table 14). Despite this, relative errors were highly variable even for [Chl-*a*] < 25 mg/m^3 and [TSM] < 25 g/m^3, leading to uncertain retrievals, especially for [Chl-*a*]. Regarding Z_{SD}, the highest correlation was observed with Kd_z90max derived from C2XC ($r = 0.94$), but $r > 0.75$ was retrieved with all C2-Nets (Table 16). The Kd_z90max from C2RCC included a subset of the *in situ* Z_{SD} measurements corresponding to increasingly clear waters with $Z_{SD} > 6$ m (match-ups mainly included by C2RCC). The Kd_z90max was lower than Z_{SD} for this set of points (Figure 47c).

Table 16. Summary of validation of [Chl-*a*], [TSM], and Kd_z90max derived from C2-Nets. The *m* and *b* stand for slope and intercept of the linear regression.

C2Net	Param.	*In situ min-max*	C2-Nets *min-max*	*MAE*	*RMSE*	*BIAS*	*r*	R^2	*m*	*b*
C2RCC	[Chl-*a*]	0.58 – 68.01	0.43 – 23.68	5.7	11.5	-1.16	0.72	0.52	0.26	4.38
C2X		0.61 – 68.01	1.84 – 100.25	10.2	17.3	5.85	0.81	0.66	1.16	3.96
C2XC		0.59 – 309.20	0.01 – 139.56	17.8	48.1	-12.1	0.94	0.88	0.45	5.03
C2RCC	[TSM]	0.74 – 28.02	0.93 – 19.13	2.9	4.6	-0.13	0.75	0.56	0.65	2.17
C2X		2.28 – 28.02	3.84 – 56.22	10.9	14.9	8.77	0.68	0.46	1.42	3.95
C2XC		2.28 – 162.33	0.33 – 58.52	13.1	29.0	-2.76	0.81	0.65	0.33	9.71
C2RCC	Z_{SD}	0.45 – 9.1	0.45 – 7.03	-	-	-	0.77	0.59	1.09	0.08
C2X		0.45 – 5.80	0.27 – 4.00	-	-	-	0.82	0.67	1.09	0.29
C2XC		0.17 – 7.70	0.27 – 6.63	-	-	-	0.94	0.88	0.88	0.12

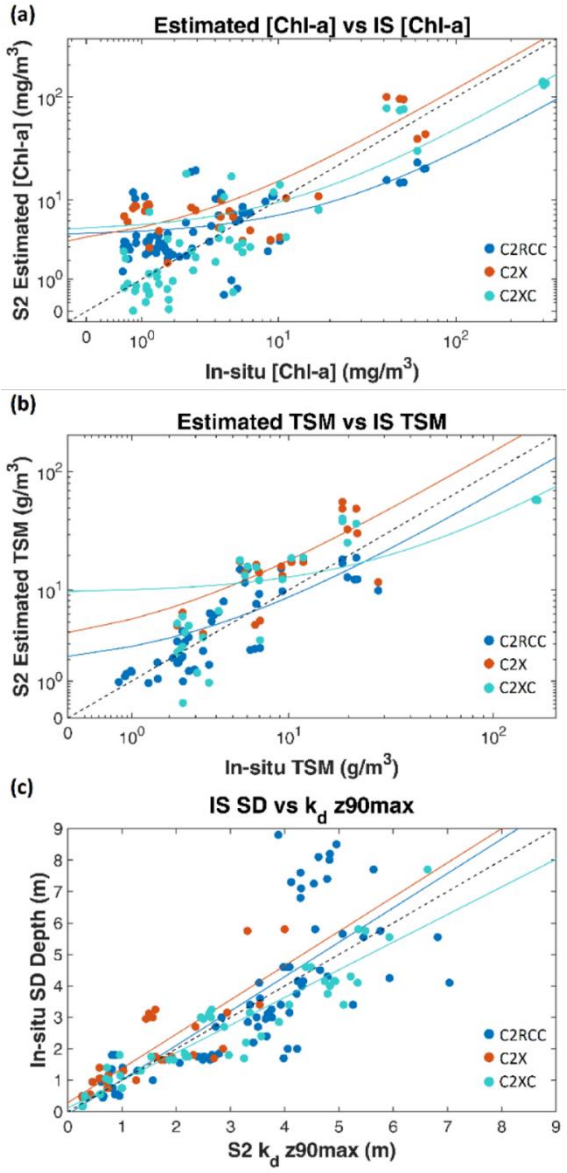

Figure 47. Scatter plots of *in situ* and C2-Nets estimated (a) [Chl-*a*], (b) [TSM], and (c) Z_{SD}. Plots in (a) and (b) are shown in logarithmic scale for ease of interpretation. Dashed is the reference (1:1) line.

5.4. DISCUSSION

To date, only C2RCC and C2X have been previously explored for retrieval of water surface reflectance or water quality (*e.g.,* Warren *et al.*, 2019; Pahlevan *et al.*, 2021). This study evaluates the new C2XC processor, comparing it to the previous C2RCC and C2X.

5.4.1 Performance on Retrieval of Rrs with C2-Nets

Comparing C2-Nets scoring (Figure 41), C2X and C2XC retained the spectral shape better than C2RCC, with C2XC outperforming C2X in all bands except B560 and B865 (Figure 41a) and showing greater consistency than other C2-Nets in the relative errors of B443-B783 through different types of waters (Figure 46d). However, with C2X and C2XC, a great number of pixel windows were rejected (Figure 40), mainly related to oligotrophic–mesotrophic waters. Most of these match-ups were only kept with C2RCC. Contrarily, the match-ups rejected with C2RCC were related to higher Rrs and associated with green (B560) and NIR (B705) peaks (C1 and C2 in Figure 46). In these scenarios, C2RCC tended to highly underestimate Rrs, even overlooking spectral peaks, limiting the use of this processor in eutrophic–hypertrophic waters. In those scenarios, C2X and C2XC retrieved the peaks more accurately, especially in the NIR (*e.g.,* Figure 44c,e), although they tended to mismatch in the green peaks, especially in the presence of large B705 reflectance (*e.g.,* Figure 44b,e,g). This may be related to the absorption of colored dissolved organic matter (CDOM), as found in (Niroumand-Jadidi *et al.*, 2021) in lakes with high concentrations of optically active constituents, where CDOM absorbs most of the light in the blue part of the spectrum (Ligi *et al.*, 2017), complicating the optimum retrieval of IOPs and leading to mismatching of peaks in green bands. Even so, C2X and C2XC provided for a better representation of the overall spectral shape in more turbid waters.

The different performances of C2-Nets along different scenarios could be explained by the different range of training datasets (Table 13) and the minimization of adverse effects by the NN (Tavares *et al.*, 2021). The C2RCC showed better performance in oligotrophic–mesotrophic waters, but in ultraoligotrophic waters (clear waters with $Z_{SD} > 3$ m and [Chl-*a*] < 2.5 mg/m^3) accurate retrieval of Rrs was complicated (*e.g.,* Figure 44f) as also observed in (Pereira-Sandoval *et al.*, 2019). The C2XC was suitable for more complex waters (up to hypereutrophic reservoirs) but also improved the performance of C2RCC in some mesotrophic scenarios, such as coastal waters in Figure 44h. Although C2X has been observed to be more suitable for coastal and complex waters than for clear waters (Pereira-Sandoval *et al.*, 2019; Pahlevan *et al.*, 2021; Tavares *et al.*, 2021), the reduced number of valid match-ups (33%) and lower consistency in the accuracy along the spectrum observed with this processor made it the most uncertain C2-Net. This could be related to the large training range of IOPs of C2X, which may allow good Rrs retrievals to be achieved in different types of scenarios (*e.g.,* Figure 44b,e) - including oligotrophic–clear and eutrophic–turbid lakes (Soomets *et al.*, 2020) - although the width of IOP ranges may also introduce a

risk of diverging from the actual solution from the inversion, leading to confusion (Niroumand-Jadidi *et al.*, 2021).

5.4.2 Recommendations on the selection of C2-Nets

The aforementioned suggests combining C2-Nets to improve Rrs estimates in a wide range of scenarios. The choice of the C2-Nets could be limited to C2RCC and C2XC for most of the scenarios observed in the studied areas targeted. Different studies have proposed to switch between atmospheric correction methods depending on optical water types (OWTs). To define OWT, Uudeberg *et al.* (2019) developed a classification based on key features of the Rrs reflectance spectrum, such as the location of the spectral maximum, slopes, and amplitude. However, the choice of the atmospheric correction processor strongly affects the OWT classification and has to be performed after the atmospheric correction process. In Pereira-Sandoval *et al.* (2019), it was observed that the accuracy of several atmosphere correction processors improved markedly after the prior classification of water types defined by [Chl-*a*] and Z_{SD} ranges of *in situ* measurements. However, this kind of classification implies prior knowledge on dynamic ranges of water quality parameters, and biophysical characteristics are not always the unique factor defining the performance of C2-Nets (see Figure 44a,b).

To improve these approaches, we suggest that research focused on the classification of TOA optical types might be useful for selecting the optimum C2-Net, improving accuracy in the retrieval of Rrs. The TOA measurements do not require prior knowledge of the conditions of the studied area and somehow include information on the atmosphere, the optical properties of water, and additional effects such as sun glint or land adjacency. A simplistic classification of the TOA reflectance spectrum and its relationship with C2-Nets choice is shown (Figure 46). Further research including more data and deeper classification analysis should also be conducted attending to the severity of sun glint and the effect of land adjacency, which have a larger impact in small inland waters (Ansper and Alikas, 2019). After selection and processing with the optimum C2-Net, methods accounting for spectral shape, magnitude, and distinctive Rrs spectral features (*e.g.,* ; Moore *et al.*, 2014; Spyrakos *et al.*, 2018; Uudeberg *et al.*, 2019) will be further evaluated for accurately defining the OWT.

5.4.3 Recommendations on water quality estimation with C2-Nets

For estimation of Z_{SD}, the Kd_z90max band derived from C2-Nets showed great potential (Figure 42c), particularly with C2XC (Table 16). Despite this, estimating the Z_{SD} in clear waters seems more challenging, while in other meso-eutrophic waters, light attenuation-related products have already demonstrated great accuracy (Soomets *et al.*, 2020). Other studies proposed to use the B560/B705 ratio (Sòria-Perpinyà *et al.*, 2021) for estimating Z_{SD}, but this approach should be more limited to mesotrophic–eutrophic waters since in hypereutrophic waters accuracy in green reflectance decreases, which may lead to higher uncertainty of this band ratio in

turbid waters. Regarding [Chl-*a*] and [TSM], both conc_chla and conc_tsm bands from C2-Nets did not provide acceptable estimations, and their use with default parameters (factors and exponents) is not suitable for the whole range of optically active constituent concentrations and scenarios targeted here. The performance of C2-Nets' [Chl-*a*] and especially [TSM] products could be improved by recalibrating with *in situ* data the factors used in the C2-Nets for their computation, but they might need to be adapted for specific locations. A common alternative approach is to switch between different empirical and bio-optical algorithms depending on the optical water type (OWT). Algorithm blending based on OWT has proven to be superior to single algorithms when considering the entire dynamic range of environmental conditions (Moore *et al.*, 2014).

In general terms, for estimation of [Chl-*a*] in more complex waters, it would be recommended to avoid the use of blue and green bands, with higher uncertainty in the presence of peaks in B705. Also, in eutrophic waters, the reflectance peak of phytoplankton shifts towards longer wavelengths, and the use of B705 is recommended (Gons *et al.*, 2005; Toming *et al.*, 2016; Caballero *et al.*, 2020). Thus, in those cases, the combined use of red and NIR bands - for which C2XC and C2X showed better agreement with *in situ* Rrs in these types of waters - must be considered. For instance, band ratios based on red–NIR combinations have been demonstrated to be able to accurately retrieve [Chl-*a*] in turbid eutrophic waters (Gitelson *et al.*, 2008; Mishra and Mishra, 2012; Caballero *et al.*, 2020). In more clear waters, related to oligo-mesotrophic status, empirical standard algorithms based on VIS combinations such as OC2, OC3, and OC4 are frequently applied with an accurate estimation of [Chl-*a*] (Pereira-Sandoval *et al.*, 2019; Moore *et al.*, 2014; Caballero *et al.*, 2020). The use of blue and green bands is appropriated in oligotrophic waters (<4 mg/m^3), although red bands contain relevant information for retrieving [Chl-*a*] in these types of waters too (Pahlevan *et al.*, 2021), and the retrieval of [Chl-*a*] through the combination of red and green bands has shown less sensitivity to the atmospheric correction in oligotrophic to mesotrophic waters (Soriano-González *et al.*, 2019).

For the estimation of [TSM], the optimal spectral range is located between 680 and 730 nm (Nechad *et al.*, 2010), and different studies propose to exploit the B705 band, alone or in combination with VIS bands, with which linear relationships have been observed for a wide range of TSM concentrations (Gernez *et al.*, 2015; Alvado *et al.*, 2021; Sòria-Perpinyà *et al.*, 2021).

5.5. CONCLUSION

This study highlights the potential of the combination of C2-Nets processors for improving the accuracy and consistency of water surface reflectance estimates on a pixel-wise basis. Within the processors, this study is one of the first attempts to test the capabilities of C2XC, the most recent evolution of the C2RCC. The results suggest that combining the use of C2RCC and C2XC — depending on the pixel optical type in the TOA — would lead to improved accuracy in the retrieval of Rrs in a wide range of waters, along with several different scenarios. Regarding the

retrieval of water quality parameters, the C2-Nets Kd_z90max product demonstrated great capabilities as a proxy of Z_{SD}. However, for estimating [Chl-*a*] and [TSM], the use of the products included in the output of the C2-Nets, with default factors and exponents, is limited and site-specific. Thus, different approaches might be selected, including the recalibration of the constants in the C2-Nets parametrization or the blending of different algorithms, depending on the optical water type and the related performance of the atmospheric correction. An in-depth exploration of TOA reflectance classification could contribute to an accurate selection and combination of C2-Nets and their further evolution, which suggests a promising future for supporting the monitoring of inland and coastal waters.

Chapter 6

MONITORING COASTAL STORM EFFECTS WITH SENTINEL-2

A LAND-AQUATIC INTEGRATED APPROACH

Edited version of:

Angelats, E., Soriano-González, J., Fernández-Tejedor, M., Alcaraz, C. Combined inundation and water quality monitoring during short extreme events using Sentinel-2: The case of study of Gloria storm in Ebro Delta. XXIVth ISPRS Congress 2022 (Nice).

From an integrated monitoring approach of coastal areas, it is essential to understand land and aquatic environments dynamics, and the relationships and interactions between them. This approach is of major importance when assessing the effects of extreme events such as high-intensity and/or long-duration coastal storms. In this sense, most of the studies focus on flooding risk assessment and the morphological changes in the coastal front, but the integration of both land and sea processes is not common. This chapter presents a methodology for the monitoring of land inundation and water quality (*i.e.,* chl-*a*) dynamics before and after an extreme storm in a coastal area from S2 imagery, applied to Alfacs Bay (Ebro Delta) during the Gloria storm (January 2020). The proposed methodology combines some of the methods described in Chapters 2-5. Despite it is an initial study, its future development will be of interest for understanding future impacts of extreme meteorological events, which frequency will increase because of climate change, and consequently to develop management practices for preserving ecosystem services and integrity.

6.1. INTRODUCTION

The nature of coastal areas makes them highly dynamic and susceptible to extreme variations under anomalous weather circumstances. Particularly, low-lying areas such as deltaic systems are highly vulnerable to extreme storms. The impact of the storms and associated hazards (*e.g.,* wave-driven, sea-level rise hazards) in this kind of environment induce morphodynamic processes such as beach erosion or overwash (Jiménez *et al*., 2011) and flooding episodes that may affect large extensions where multiple uses coexist (*e.g.,* urban areas, agri-food industry, ecosystem services). In addition to the physical impacts in the terrestrial ecosystem, significant rainfall and strong winds related to extreme storms lead to increased run-off from land and turbulence in coastal waters, with an expected impact on the water quality and aquatic ecosystems (Hernández *et al*., 2020). A better understanding of the relation between storm events and landscape/ecosystem development is needed. This is a key step for improving territorial and emergency management strategies on storm-induced hazards assessment, preparedness, response, and environmental resilience monitoring.

The Ebro Delta area is an excellent case of study because it harbours important terrestrial and aquatic ecosystems, as well as several related economic activities sensitive to extreme storms. It is a subsident area with an unprotected coastline enclosing two coastal bays with high ecological and socio-economical value. The importance of storm hazards in Ebro Delta in terms of magnitude and recurrency has been increasing since the 90's with most hazardous storms characterized by low-pressure systems off the Ebro Delta coast and eastern wave storms, usually accompanied by storm surges and heavy rainfall. Such events lead to a compound flooding that affects most of the Ebro Delta surface and induces morphological disturbance in the coastal front and bays (Jiménez *et al*., 2011). Furthermore, increased discharge of Ebro River, land run-off, and sediment suspension and

transport in coastal waters suppose a direct impact on the aquatic ecosystems and related economic activities such as fisheries or aquaculture (Berdalet *et al.*, 2020).

This, together with the expected exacerbation of these trends under climate change scenario, has led to several studies assessing the effect of these events in the area. Some studies have been focused on reporting and documenting the events with social media and media pictures, visual interpretation of airborne imagery, and reporting of the consequences (González *et al.*, 2020; Jiménez *et al.*, 2020). Alternatively, most scientific research efforts have been focused on the investigation of flooding risk and coverage, and morphodynamics through numerical model simulations under storm and climate change scenarios, and do not include reports on water quality dynamics (Alvarado-Aguilar *et al.*, 2012; Garcia *et al.*, 2013; Amores *et al.*, 2020). All this information is a highly valuable source of knowledge for assessing the consequences of the storm-induced hazards in the delta contributing to improving risk, land, and emergency management strategies. However, there is still a gap for improvement in terms of observation-driven methods for the monitoring of storm-induced hazards, complementing and/or enhancing the current approaches in the area. Especially, on the assessment of flooding events and associated morphodynamic changes under high-intensity storms over large areas, and the monitoring of water quality parameters (*e.g.,* Total Suspended Solids (TSS) or chlorophyll-a concentration (chl-*a*)), when access to *in situ* measurements may be limited. From this perspective, spaceborne multispectral remote sensing is a unique source of data as it provides a synoptic view over large areas and frequent systematic observations.

Among remote sensing platforms, the Sentinel-2 multispectral imagery satellites (S2) represent a breakthrough in terms of flooding and water quality monitoring (Caballero *et al.*, 2020; Goffi *et al.*, 2020; Sobel *et al.*, 2020; Cavallo *et al.*, 2021). Detection of flooding and land surface water change based on multispectral satellite imagery generally relies on the use of water-related indicators proposed as combinations in the VIS, NIR, or SWIR spectral regions in form of spectral index (Pekel *et al.*, 2014). Overall, combinations of VIS/SWIR and NIR/SWIR spectral bands provide for a clear diagnostic of water surfaces, having positive values for flood conditions and negative values for soil, both wet and dry (Boschetti *et al.*, 2014). However, as the selected index response varies as a function of the study area, water characteristics, environmental and atmospheric conditions, the combination of multi-source data is recommended for improving classification accuracy (Acharya *et al.*, 2018). Multiparameter classification methods aim to reinforce the characterization by exploiting redundancy or complementarity provided by multiple spectral features (Goffi *et al.*, 2020). In this regard, the integration of different band combinations has been reported to improve the accuracy of land cover mapping (including flooding and classification of dry and mixed surfaces) through different segmentation techniques (*e.g.,* Cavallo *et al.*, 2021; Tavus *et al.*, 2020).

Extensive research can be found related to the retrieval of water quality parameters such as TSS or chl-*a* from remote sensing reflectance (Rrs). The common

approaches rely on empirical and/or bio-optical algorithms that exploit spectral signatures of different water constituents, along with different band combinations depending on the water optical properties (Moore, *et al.*, 2014; Caballero, *et al.*, 2020). All of them use a set of *in situ* values to calibrate and validate the different models. The performance of the different algorithms depends mainly on the type of water of the study and the accuracy of the atmospheric correction, but also on the dynamic range of concentrations of water quality parameters within the area of study. Some research has been done in relation to the monitoring of the impact of short extreme events on water quality. Sobel *et al.* (2020) used S2 imagery to evaluate the impact of several Hurricanes in the Gulf of Mexico in terms of TSS concentration. Several studies suggest that water quality recovers relatively quickly from severe events (Huang *et al.*, 2011; Chen *et al.*, 2017) while others indicate long-term impacts (Beaver *et al.*, 2013; Wetz and Yoskiwitz, 2013).

This study presents a methodology for the monitoring of the inundation and water quality (*i.e.,* chl-*a*) dynamics from S2 imagery under extreme storms in coastal areas. In particular, the proposed methodology has been applied in a coastal bay of the Ebro Delta (Catalonia, NE Spain) to evaluate jointly the impact in terms of land-flooding and water quality in Alfacs bay during and after the Gloria storm (January 2020). The study aims to demonstrate how S2 imagery together with appropriate modelling can be used as a tool for assessing the ecosystem response of a coastal area in the aftermath of an extreme climatic event, through an integrated approach. Moreover, this study presents the first steps of an overall goal that is to set the bases in a long term, for a workflow for rapid response and continuous monitoring of storm emergencies in low deltaic and highly vulnerable areas such as the Ebro Delta.

6.2. MATERIALS AND METHODS

6.2.1 Study area

The results presented in this chapter are focused on Alfacs bay (Figure 48), the southern coastal bay, where many of the threats driven by storms in the Ebro Delta are observed. In this sense, Alfacs bay concentrates an aquaculture activity, an extremely vulnerable piece of coast heavily affected by erosion (Trabucador barrier), and La Banya spit, a special Protection Area for birds including a dune system that is part of Ebro Delta Natural Park.

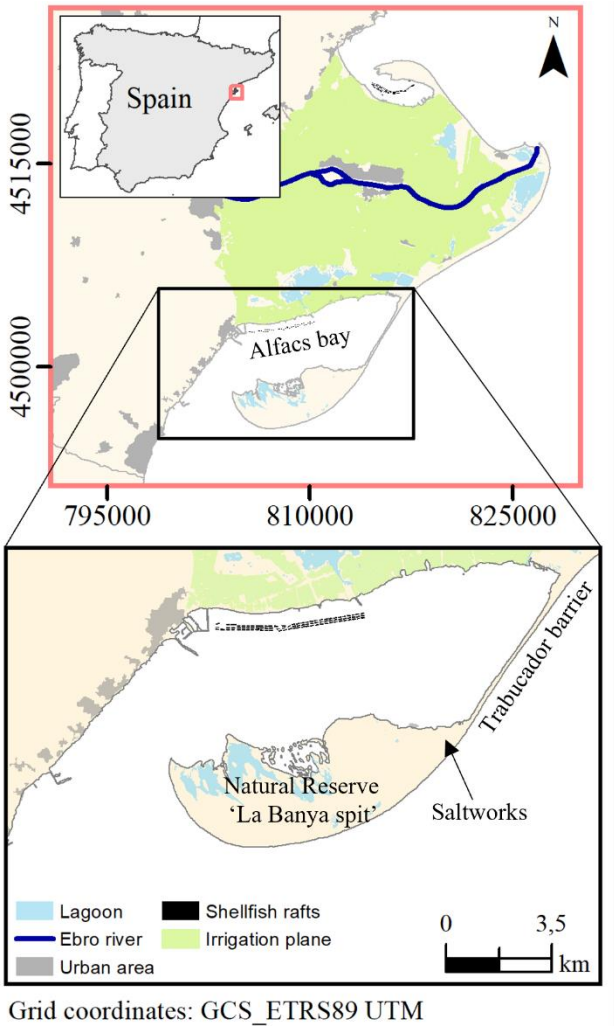

Figure 48. Summarized depiction of the study area.

6.2.2 Gloria storm

Gloria storm was a marine storm affecting the Ebro Delta region in January 2020 (19.01.20 – 23.01.20). It has been classified as one of the most intense among the events in the region during the last decades with immediate economic losses of several millions of euros. During the event of storm Gloria, the situation was dominated by a southern deep low-pressure system that generated sea level surface elevation (up to 1 m) and strong easterly winds which induced wind waves in the sea surface (Amores et.al, 2020) with high significant height (maximum Hs > 7m) and heavy rainfall on land (maximum cumulative precipitation > 130 mm). The Gloria storm had devasting effects on urban areas, agriculture fields, the natural

environment, and different crucial infrastructures such as road nets, becoming the most hazardous event in Ebro Delta in the last decades.

6.2.3 Inundation mapping

A set of 11 S2A/B L2A (atmospherically corrected surface reflectance) cloud-free images were visually filtered and downloaded from Copernicus Open Acces Hub (https://scihub.copernicus.eu/) accounting for dates pre-, during, and post-Gloria storm. All S2 L2A images were subset to the Ebro Delta area (Figure 48) and resampled to 20 m pixel using the Sentinel Application Platform (SNAP v8.0). The same tool was then used for deriving two variants of Normalized Difference Water Index (NDWI), namely, $NDWI_{GAO}$ (Gao *et al.*, 1996) and $NDWI_{XU}$ (Xu *et al.*, 2006). The $NDWI_{GAO}$ combines NIR (B8 band centered at 832 nm) and SWIR (B11 band centered at 1614) bands of S2 (eq. 18), while the $NDWI_{XU}$ applies a VIS/SWIR approach combining Green (B3 band centered at 560 nm) and SWIR (B11) S2 bands (eq. 19).

$$NDWIGAO = \frac{B8-B11}{B8+B11} \tag{18}$$

$$NDWIXU = \frac{B3-B11}{B3+B11} \tag{19}$$

These indexes were used later as input in an unsupervised *k*-means clustering to generate 4 classes for each image. Then, the mean and standard deviation of pixels within each class and SI (4 classes × day-1 × number of dates; $N = 44$) were extracted and reclassified into two classes by means, again, of unsupervised *k*-means clustering. The $NDWI_{XU}$ cluster centers were then used for defining water (positive $NDWI_{XU}$) and non-water classes (negative $NDWI_{XU}$) resulting in binary maps. This method aimed to first differentiate 4 classes which may be water or non-water and then solve the uncertainty of single images classification by time series analysis of different classes accounting for different types of water and surface state. It was implemented using a customized script developed for R software v3.6 (R Core Team, 2017).

6.2.4 Chl-*a* mapping

The chl-*a* maps during the Gloria storm are part of a longer time series (October 1st 2019, to September 30th 2021) in the area of Ebro Delta (Figure 48 top). This subsection summarizes the methodology used to generate this time series of chl-*a* maps.

All available S2 L1C orbit R051 images during the two-year period of interest were downloaded from the Copernicus Services Data Hub (https://cophub.copernicus.eu/dhus/#/home). After image-by-image visual checking for clouds and shadows over the Ebro Delta coastal waters, the valid images ($N_{images} = 210$) were pre-processed. This step included the resampling of the bands to 20 m pixel, the subset to the extent of the area of interest, and the

atmospheric correction specific for coastal waters, all implemented through the Graph Processing Tool of SNAP v8.0. The atmospheric correction was done with the latest version of the Case 2 Regional Coast Colour processor (Doerffer, *et al.*, 2007; Brockman *et al.*, 2016), here referred as to C2XC. It was applied on all valid S2 images, with a fine-tuning of daily auxiliary data (pressure, ozone, altitude, salinity, and water temperature). For land/water segmentation, the valid pixel expression was set as a threshold on band B11 of S2 L1C images. The threshold was defined independently for each image with the histogram-based triangle method. The output of C2XC included Rrs at VIS-NIR S2 bands.

Field measurements ($N = 146$) were conducted along 26 dates, at different locations including waters in Alfacs bay, Fangar bay, and the surrounding exterior Mediterranean sea. The measurements corresponded to integrated water column samples, taken within a window of ±3 hours of S2 pass. For chl-*a* determination, water samples were filtered through 0.4-0.6 μm GF/F glass fiber filters, extracted using standard methods (Shoaf and Lium, 1976), and calculated with Jeffrey and Humphrey's (1975) equations.

Then, the match-up exercise between field-measured chl-*a* data and C2XC Rrs was done using a quality-check procedure based on 3x3 pixel-window centered at field measurements. The quality check included the removal of pixels flagged inherently by C2XC, an additional outlier filtering using boxplot analysis, and the removal of negative Rrs pixels. Only pixel windows with more than 4 pixels remaining were accepted for posterior analysis. After this step and the rejection of cloud-affected S2 images, the number of valid field chl-*a* data was 73, ranging between 0.1 – 8 mg/m^3, along 14 different dates.

For chl-*a* estimation, a set of 11 band combinations (2 to 4 spectral bands) in form of spectral indices (SI) were computed for all valid match-ups. These SI included bands B1 (centered at 443 nm) to B6 (centered at 740 nm) and exploit specific chl-*a* absorption peaks in Blue and Red spectral regions, and/or use red-Edge information for mitigating the effect of absorption by non-algal particles and yellow substances. For instance, common ocean colour algorithms based on Blue to Green ratios (O'Reilly and Werdell, 2019), the three-band model of Gitelson *et al.* (2011), and the Normalized Difference Chlorophyll Index (Mishra and Mishra, 2012) were included among the tested SI. Chl-*a* was modelled with all of them. A 70% of chl-a data was used for model calibration (cal), and 30% for validation (val). The cal/val datasets were generated randomly. Models were developed for raw and log-transformed (when possible) Rrs and chl-*a* data (*i.e.,* raw-raw, log-raw, log-log). Linear, linear piecewise (1 breakpoint), polynomial (2nd, 3rd, and 4th order), logarithmic, power, and exponential models were tested. All the process was repeated through 100 iterations, with varying cal/val datasets. For each model (Band Combination × Type of Fitting × Iteration), performance was evaluated by means of the following statistics: the Mean Average Error (*MAE*), the Root Mean Squared Error (*RMSE*), the Average Percentage Difference (*APD*), the *BIAS* (eq.20-23) and the Pearson's r (*r*). The statistics were computed including calibration and validation datasets.

To generate the chl-*a* maps, all flagged pixels (C2XC flagging) or pixels with negative Rrs in any of the spectral bands of each valid S2 image were removed. A mask was applied for avoiding most shallow waters and the presence of macrophytes, which make the retrieval of chl-*a* more uncertain. Then, the model with the best performance was applied to all valid images and pixels. Those with negative chl-*a* value (residual) were set to 0 mg/m^3 and pixels with chl-*a* > 30 mg/m^3 were removed (noData) given the higher uncertainty in so high concentrations. Pixels corresponding to the mussel rafts were masked out with a rafts' shapefile (Figure 48 – Shellfish rafts).

$$MAE = \frac{1}{N}\sum_{i=1}^{N}|M_i - O_i| \quad (20)$$

$$RMSE = \sqrt{\sum_{i=1}^{N}\frac{(M_i - O_i)^2}{N}} \quad (21)$$

$$APD = \sum_{i=1}^{N}\frac{|M_i - O_i|}{O_i} * 100 \quad (22)$$

$$BIAS = \frac{1}{N}\sum_{i=1}^{N}(M_i - O_i) \quad (23)$$

Where M_i are the estimated values and O_i the field measured ones.

6.3. RESULTS AND DISCUSSION

6.3.1. Chl-*a* estimates

Overall, models that performed better were related to Rrs bands combinations including B2 (centered at 490 nm) or B3 (centered at 560 nm), and B4 (centered at 665 nm) or B5 (centered at 705 nm). The best model for chl-*a* estimation was found with a simple B5/B2 band ratio fitted with a 2nd polynomial (eq. 24). The performance metrics of the model were *MAE* = 0.60 mg/m^3, *APD* = 36.22 %, *RMSE* = 0.89 mg/m^3, *BIAS* = 0.05 mg/m^3, and *r* = 0.89.

$$chl - a = -0.62 + 10.88 * (\frac{B_5}{B_2}) + 8.07 * (\frac{B_5}{B_2})^2 \quad (24)$$

Despite the implemented model achieving good agreement within the full range of derivation ~ 0 - 8 mg/m^3 (Figure 49), overestimation of retrieved chl-*a* concentrations in scenarios with great concentrations of TSS is expected. Empirical algorithms, as the one used, can perform well only inside their range of derivation and for the area for which they are derived. They are more limited in their ability to discriminate between non-unique signals from parameters that may be covariant with chl-*a*, for instance, TSS (Matthews *et al.* 2012), which increases particularly during storm events. This could not be validated because no chl-*a* nor TSS data were available in such cases, but it was observed in RGB composites that after strong winds or storm events, the water of the bays turns darker brownish or whitish, suggesting higher TSS (*e.g.,* in Figure 50 and 51B). In these cases, the selected model will tend to overestimate chl-*a* since the reflectance on B5 increases with great TSS,

overlapping the absorption of chl-*a* in the Blue (Soriano-González *et al.*, 2019). In these cases, other empirical or semi-analytical algorithms may be more accurate. However, it is important to highlight that the proposed methodology for chl-*a* retrieval is easy to replicate, and straightforward using several software tools such as SNAP, which may be important for a wide part of the scientific community related with ecosystems monitoring and modelling response but with few or no remote sensing skills.

Nevertheless, further research should move towards a multi-algorithm combination, suitable across different types of water optical properties. The development of a blending algorithm requires accurately defining the optical water type (Moore *et al.*, 2014) accounting for the spectral shape, magnitude, and distinctive Rrs spectral features. Furthermore, a greater amount of field data is needed, covering all different scenarios, which were not represented in the current chl-*a* dataset.

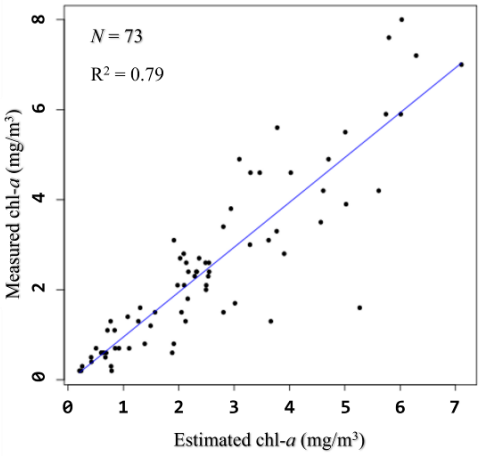

Figure 49. Linear regression of estimated and measured chl-*a*.

6.3.2. Inundation mapping

Systematic validation of inundation maps was not conducted, albeit a visual comparison of the resulting maps showed good agreement with what can be interpreted from the 10 m RGB composites of S2 in Alfacs bay (*e.g.,* in Figure 50). The method allowed us to assess the evolution of the main morphological phenomena that occurred during the Gloria storm in the bay, the breaching of the Trabucador barrier. From visual interpretation, the main limitations of the method arise from; i) small features (*e.g.,* shellfish rafts, borders between dry and flooded surfaces) which may be misclassified due to the pixel mixing with the flooded surrounding environment; ii) increasing uncertainty in presence of emerged or submerged vegetation and continuous succession of small emerged and submerged patches (Ozesmi and Bauer, 2002).

Figure 50. Delineation of emerged land and water surface two weeks after Gloria storm (05.02.20) with the proposed methodology (black line) superposed to the S2 RGB composite.

Additional research is needed for further validating the accuracy and exploring possible unseen corners of the proposed methodology. For instance, the minimum number of images to be used must be defined. Also, the 4-initial *k*-means classes may be a constraint in more heterogeneous environments, needing to explore the increasing of clusters number. Regarding the improvement in the detection of small features, suitability for resampling to 10 m instead of 20 m pixel can be studied, albeit it will strongly depend on the native resolution of S2 bands. In addition, information on the sea level simultaneously to the S2 pass must be considered in deeper analysis.

In spite of all that, the proposed method does not depend on large time series, avoids the difficulty of finding stable thresholds as in decision trees or rule-based approaches, is fast and unsupervised, and requires simple computation, allowing for rapid mapping in the aftermath of a storm, which is a key pillar in the management of extreme events.

6.3.3. Chl-*a* and morphology response to Gloria storm in Alfacs bay

For assessing the dynamics of water quality and flooding in the Alfacs bay, three status-maps (Figure 51) and three change-maps (Figure 52) were generated within a period of one month encompassing the Gloria storm (21.01.20).

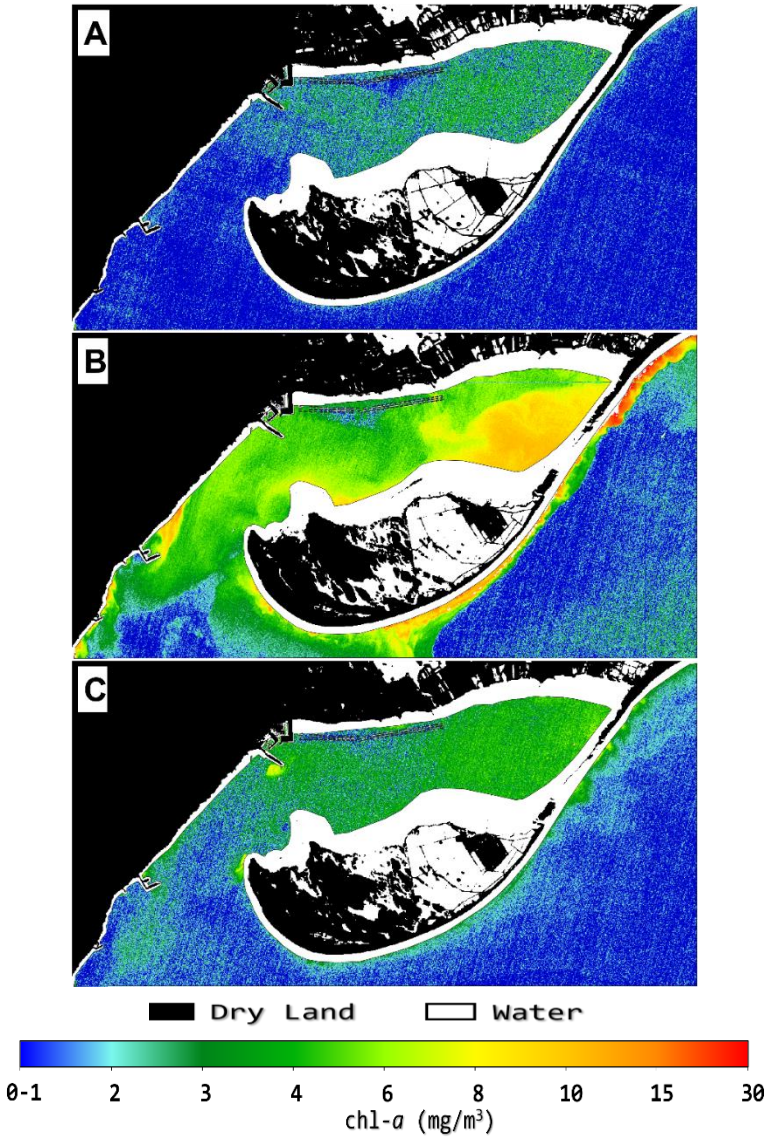

Figure 51. Water quality and inundation mapping in the area of Alfacs bay before and after Gloria Storm. A) 16.01.20; B) 05.02.20; C) 10.02.20.

The Gloria Storm caused breaching of the Trabucador barrier, without showing signs of recovery after 20 days (Figure 51B). The thin line that seems to reconnect the delta with La Banya spit (Figure 51C and 52B) was the ongoing reconstruction of the road for in/out of the trucks transporting salt from the saltworks (Figure 1). La Banya spit remained disconnected from the delta during all the period shown (Figure 4C and 5C), preventing the passage of vehicles and the transport of goods to and from the saltworks. It can be observed in the change maps that the

Trabucador barrier breached from the center and receded back into the bay. The setback was evident in the extremes of the barrier as observed in Figures 5A and 5C corresponding to the difference between the 15th and 20th days after the storm and the image of 5 days before the Gloria storm.

In La Banya spit (Figure 48), the most important effects of Gloria storm were observed on the eastern side, at the dune fields. In this area, the barchan dunes in the shoreline side showed stability, with no inundation detected (Figure 5). The inner dunes, however, showed a more dynamic behaviour, alternating flooding, and drying of the northern and southern faces during the period of study (Figure 52A-B). Where flooding is more intense, the inner parts of La Banya spit are subjected to loss of volume (Rodríguez-Santalla *et al.*, 2021). The drying out of some of these parts may be explained by the accretion due to sand blown from the beach and dunes and trapped by vegetation growing on the foredune. This phenomenon is observed in Figure 52C, with most of the dried area concentrated behind barchan dunes. This highlights the importance of the barchan dunes for maintaining the shoreline during a storm (Rodríguez-Santalla *et al.*, 2021).

Regarding water quality dynamics associated with the Gloria storm, water turbulence increased, particularly in the inner north-eastern Alfacs bay, related to the Trabucador breaching (Figure 51B) and the shallow shelf formed behind it. This led to increased chl-*a* concentrations, although the model could be overestimating them in this scenario, as high TSS concentration is expected in this area behind the Trabucador barrier breaching stretch. In the last date shown (10.01.20 – Figure 51C), chl-*a* concentrations were again closer to pre-storm concentrations (Figure 52C). Different from the Trabucador barrier, the water quality showed signs of recovery in a short term. In the long-term, water quality dynamics should be revised again since the breaching of the Trabucador barrier has important implications in the morphodynamics and hydrodynamics of the bay (Gracia *et al.*, 2013). These are major factors for the development of phytoplankton populations related to the modulation of chl-*a* inside Alfacs bay, with a direct effect on the farming of shellfish (Soriano *et al.*, 2019).

6.4. CONCLUSIONS

This study presents a methodology for chl-*a* (in water) and inundation mapping (on land) based on parallel processing of Sentinel 2 multispectral imagery. The methodology has been applied to the assessment of impacts of an extreme coastal storm affecting the Ebro Delta in January 2020. The Ebro Delta is a suitable place to apply the methodology developed here since it shares common threats with other coastal regions and, more specifically, with other deltas.

Despite constraints related to the validation of inundation maps and the uncertainty of chl-*a* retrieval under optical water types out of the range of development of the model, the results obtained are promising. The model presented for chl-*a* mapping will normally produce chl-*a* estimates with accuracy greater than 70% and, the

methodology proposed for mapping of land water surface changes demonstrated great agreement with visual interpretation from 10 m RGB imagery.

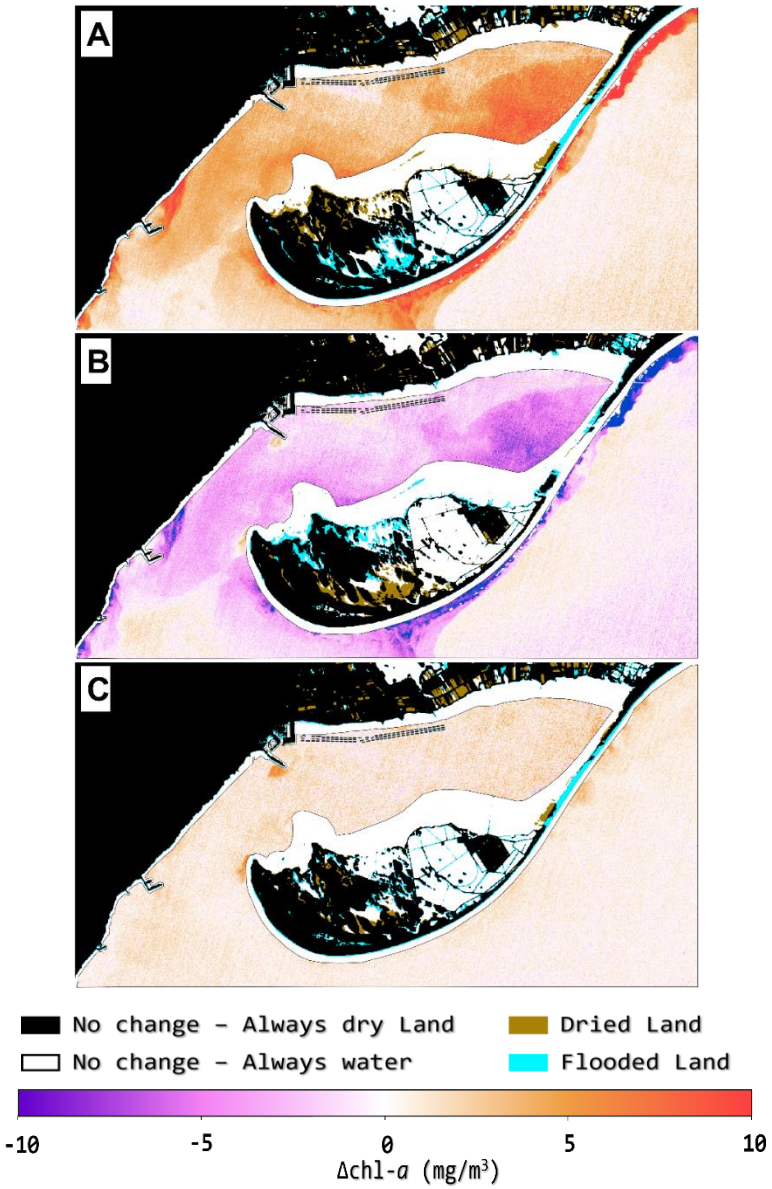

Figure 52. Changes in water quality and inundation related to the Gloria storm. Differences between A) 05.02.20 -16.01.20; B) 10.02.20 - 05.02.20; C) 10.02.20 – 16-01.20.

The exposed methodological development allowed assessing changes both in water and land, through a well-explained processing chain which can be easily implemented almost with SNAP open software. Both, inundation delineation and

water quality mapping methodologies can be applied fast, allowing for rapid evaluation of storm-related perturbances on terrestrial and aquatic ecosystems, with particular importance in the management of coastal areas. Sentinel 2 demonstrated great capabilities for complementing current methods and supporting management in diverse environments, through the potential for conducting studies with integrated approaches, which is currently a line to follow for achieving the sustainable development goals.

The research presented in this paper is one of the first steps with Sentinel 2 of a long-term strategy to understand the ecosystem response in Ebro Delta both in space and time in front of short extreme events. Further research should include an improvement of the current water quality modelling aiming to de-coupling TSS from chl-*a*. The inundation mapping must be validated, assessing the accuracy of the method and arising potential constraints or improvements not included in this preliminary study. The proposed methodology is planned to be extended to all Ebro Delta region, and tested also in other short extreme events that occurred recently such as Filomena storm (January 2021).

Chapter 7

GENERAL DISCUSSION and FURTHER RESEARCH

In a context of climate change characterized by accelerated sea-level rise, sea-water temperature increase, and the exacerbated frequency of extreme events, Integrated Coastal Zone Management (ICZM) is an immediate priority. ICZM provides enabling mechanisms, facilitates capacity building and the implementation of sustainable policies, among other benefits (O'Mahony *et al.*, 2022). An integrated monitoring is thus essential. In this thesis, the potential of Sentinel-2 (S2) as an efficient monitoring tool for coastal areas (low cost, systematic, high-resolution, and long-term) has been demonstrated. We addressed several technical and scientific issues related to the estimation of a variety of key coastal parameters, from atmospheric correction and image pre-processing (first steps) to data modelling and analysis (last steps).

Image pre-processing and data expansion

The detection of clouds and shadows and their effect on the temporal distribution of data are an important constraint in optical remote sensing. Detecting and removing clouds and shadows is challenging, and may lead to misdetection. In this thesis, cloud cover reduced significantly the temporal frequency of useful S2 data, and highlighted the misclassification effect on data timeliness consistency (*e.g.,* confusion between flooded rice paddies and shadows). Although we implemented an enhanced method for clouds and shadows masking (Chapter 4), misdetection of dispersed clouds and overestimation of shadows persisted. It is needed to further explore approaches such as the Water Pixel Extraction algorithm (Ngoc *et al.*, 2019), or similar ones, focused on the removal of shadows over water pixels, and applicable to different satellite sensors (*e.g.,* S2 MSI, Landsat-8 OLI).

Multi-platform approaches contribute to increase the temporal frequency of good-quality observations (Li and Roy, 2017). In this context, the integration of Landsat-8, -9, and S2 data is recommended due to the similarities in pixel resolution and the VIS-NIR-SWIR spectral configuration. Furthermore, the thermal infrared bands of the Landsat series provide additional physical information, which is highly valuable for a number of applications such as the cloud discrimination process (Mateo-García *et al.*, 2018). In the Ebro Delta, by combining Landsat -8, -9, and S2 data, the number of available images increases 60 % (covering the full area), compared to only using Sentinel-2. Averaged frequency is reduced to 2.8±1.3 days (Figure 53), and it is expected to further improve with S2-C and S2-D, expanding the possibilities for finding cloud-free images, concurrent satellite and *in situ* measurements, and improving data-filling methods based on timeseries analysis.

Regarding atmospheric correction, a validation of the C2RCC processors (C2-Nets), in both inland and coastal waters, was conducted using above-water radiometry measurements (Chapter 5). However, increasing the dataset of above coastal-water radiometry measurements is needed, since most of those used in our study were conducted in inland reservoirs. Because the C2-Nets rely on Neural Networks trained with different ranges of inherent optical properties, the appropriate selection

of the C2-Nets is a key step for the accurate estimation of water surface reflectance, and hence water quality parameters. The results in Chapter 5 show that the combination of the C2-Nets should be conducted on a pixel-wise, based on the classification of the signal received at the Top Of Atmosphere (TOA), needing to further explore the TOA response to different atmospheric conditions, variable Optical Water Types (OWT), and additional effects such as sun glint or land adjacency.

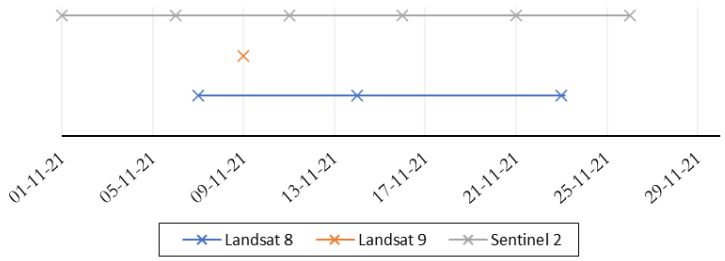

Figure 53. Example of increased data frequency in the integration of Landsat-8, -9 and Sentinel-2 images covering the full Ebro Delta in November 2021.

Considering other atmospheric correction methods, ACOLITE (Vanhellemont and Ruddick, 2018) and POLYMER (Steinmetz *et al.*, 2011) use a single processor, reducing the complexity of the classification of the 'TOA optical types'. They do not depend on Neural Networks, but are image based atmospheric correction processors and include methods for sun glint removal (Steinmetz *et al.*, 2011, Harmel *et al.*, 2018), improving the accuracy of water surface reflectance retrievals along with different satellite platforms. Another alternative is the Icor atmospheric correction processor (De Keukelaere *et al.*, 2018), which includes the SIMilarity Environment Correction module (SIMEC) for counteracting the effects of land adjacency, which may have a greater impact in Ebro Delta bays during the rice growing season (red-edge increase in typical vegetation spectra). Therefore, different processors exist and further research should be intended to explore the methods, procedures, and use cases for a simplified and systematic retrieval of accurate water surface reflectance estimates in coastal waters.

Water quality estimation

The accuracy on the estimation of water quality parameters with Sentinel-2 depends largely on water composition (type and concentrations). Different processing chains and algorithms have been successfully implemented in the Ebro Delta bays (Chapters 2, 5, and 6) for the retrieval of Secchi disk depth (Z_{SD}) and chlorophyll-*a* (chl-*a*) from Sentinel-2. In this context, the diffuse attenuation coefficient of light at 490 nm derived from the C2-Nets showed a high relationship ($r > 0.75$) with Z_{SD}

measurements (Chapter 5). Other authors propose to use VIS-NIR combinations, switching to longer wavelengths along with the increase in turbidity (Alikas *et al.,* 2015). In the same line, turbidity algorithms such as the proposed by Dogliotti *et al.*, 2015 may also be used as proxy for Z_{SD}, given the close relationship between the two variables. Regarding chl-*a* concentration, spectral indices based on simple band ratios including blue and green or red-edge bands (Chapters 2 and 6) provided for estimates with acceptable accuracy (*MAE* ~ 0.60 mg/m^3). However, the performance of the developed models out of their range of derivation, in terms of chl-*a* concentration (Ebro Delta bays - typically mesotrophic waters) and the scenarios for which they were derived (*e.g.,* water column composition and optical depth), requires an in-deep assessment to define their scope of application. The developed models are less reliable in conditions of high concentration of Total Suspended Matter (TSM) and/or Coloured Dissolved Organic Matter (CDOM), which may occur due to increased water turbulence, sediment resuspension or land runoff (Chapter 6). In these cases, the selected model tends to overestimate chl-*a* concentration, leding to unreliable results, and other empirical or semi-analytical algorithms may be more accurate. Further research should focus on the pixel-wise classification of Optical Water Types (OWT) and the development of a multi-algorithm blending approach, which has proven to be superior to single-algorithms across different water optical properties (Moore *et al.*, 2014, Caballero *et al.*, 2020).

Monitoring of water quality from remote sensing data enables the evaluation of its variability worldwide, overcoming the lack of data from new, remote, or large marine areas, with several applications in shellfish aquaculture such as definition of farming suitability index for site selection or zoning (Habbane *et al.*, 1997, Radiarta and Saitoh, 2009). Among the different water quality parameters of interest that can be measured by sensors from satellites, chl-*a* concentration is commonly used in shellfish aquaculture because it is considered the best proxy of phytoplankton biomass (Huot *et al.,* 2007). With this approach, we showed the potential of S2 for monitoring phytoplankton biomass in Alfacs and Fangar bays (Chapter 2). However, including additional water quality parameters and increasing data frequency is essential for developing bio-physiological models and deriving carrying capacity estimates, needed for proposing adequate and feasible management strategies. In this context, it is necessary to further explore the remote estimation of other water quality parameters such as CDOM, indicator of organic matter, and surface water temperature, key in the biocenosis and physical processes.

Monitoring of submerged vegetation

Remote sensing of submerged vegetation, including its detection and classification, is possible to a certain extent, in shallow and/or transparent waters by using combinations of VIS-NIR bands and supervised classification methods (Chapter 3). However, there are some constraints in relation to the spectral and spatial resolution of satellite platforms such as the pre-conditions imposed by the minimum allowable

extension and the heterogeneity of vegetation meadows (mixed classes and small patches are more difficult to discriminate), the interference of water turbidity and leaf shadowing in the sensed signal, the effect of growing depth and background, and the effect of epiphytes or microphytobenthos on spectral signature (dampening in the VIS spectrum). These aspects need further study, as well as an improvement of the algorithms for submerged vegetation classification under these different circumstances. Recent advances on deep learning-based segmentation and classification methods might provide new insights on this topic. In the Ebro Delta, Sentinel-2 showed the potential for the estimation of macrophyte and macroalgae coverage (discrimination capabilities), and its use as environmental proxy for agricultural run-off disturbance, albeit expanding the dataset of field measurements/observations is needed to validate the applied methodology. To improve it, we propose to explore approaches accounting for vegetation leaf area and/or substrate induced variations (Yang and Yang, 2009; Pu *et al.*, 2015), exploiting the spectral peak around 700 nm, which is differently influenced by seagrass types, and it is located beyond the wavelengths usually affected by epiphytes (Hwang *et al.*, 2019).

Agricultural monitoring

It is possible to automatize the monitoring of rice paddies (phenology, management, and crop yield) by combining cloud computing platforms and remote sensing data. In Chapter 4, we proposed an automatic extraction scheme using S2 which demonstrated great capabilities, albeit it needs further validation by increasing the ground truth dataset (*e.g.,* sowing date, irrigation period, rice yield, cultivar). In addition, because data frequency is critical for ensuring consistent timeseries at all rice fields, similarly to previous reported issues, cloud and shadows masking, data recovery, and multi-platform approaches are necessary to be addressed. Tackling these, time series smoothing can be improved by weighting data according to cloud contamination scores or other parameters related to spectral index uncertainty (*e.g.,* saturation). Additional improvements of the developed methodology include exploring different vegetation and land-surface inundation indexes, improving the rice paddies identificacion pixel-wise, and evolving from the proposed rice yield proxy to more sophisticated approach. We suggest to assess vegetation spectral index accounting for background effects (optimum for initial rice stages) and/or having a higher performance in stages with increased rice biomass; and land-surface inundation indexes combining VIS and SWIR bands (*e.g.* $NDWI_{XU}$ in Chapter 6) to increase the accuracy of hydroperiod estimates (Boschetti *et al.*, 2014 and 2017). For pixel-type discrimination purposes, the use of Synthetic Aperture Radar (SAR) imagery such as Sentinel-1 (SAR C-Band) in combination with multispectral data from S2 and Landsat series can help. Despite of a complex processing chain, Sentinel-1 SAR offers cloud penetration capacity, thus ensuring systematic measurements, and shows particular spectral response of water and the spiky structure of rice - at SAR wavelengths and S1 observation modes -, thus making rice fields more distinctive. These characteristics are useful in timeseries analysis for rice

discrimination and monitoring purposes (Campos-Taberner *et al.* 2017). For rice yield quantification, it is required to move towards approaches in line with the multidisciplinary simulator for standard crops (STICS, Brisson *et al.* 2003), including auxiliary data such as daily weather (*e.g.,* temperature), soil descriptions (*e.g.,* organic-inorganic ratio), and considering Leaf Area Index profiles (Courault *et al.*, 2021).

Assessment of Storm effects

Extreme storms events can significantly affect coastal areas. In Chapter 6 we assessed the changes in water quality and land inundation in the southern hemi-delta of Ebro River as a consequence of the Gloria Storm by means of a simple methodology based on S2 imagery. Although the research is still preliminary, we showed the potential for the integrated assessment of storms disturbance through satellite remote sensing. Further research must focus on improving water quality assessment (following the methods described previously), and land inundation, which could benefit from methods proposed for the assessment of rice paddies flooding and cloud and shadow detection over water pixels, landcover mapping methodologies, and by combining multi-source data for improving classification accuracy (Acharya *et al.*, 2018, Huang and Jin, 2020). In this sense, the integration of vegetation spectral indexes using the red-edge (*e.g.,* NDVI, SAVI), water spectral indexes including SWIR and VIS or NIR spectral bands (*i.e.* NDWI's), combinations in the HSV colour space, and the coupling of multispectral and SAR sensors data, can improve the accuracy of land cover mapping, including flooding and classification of dry and mixed surfaces (*e.g.* Goffi *et al.*, 2020, Tavus *et al.*, 2020, Cavallo *et al.*, 2021).

Further research must include additional geomorphological effects of storms on the emerged beach. In this context, the position of the land-water boundary is determined by several factors (e.g., sea level, waves regime), thus serving as an integrated and dynamic proxy of state (reference) and impact (change), contributing to understand coastal functionality, response, and resilience to extreme events. For this purpose, the CoastSat tool (Vos *et al.*, 2019) is of particular interest since it is an open and cloud-based solution that offers transparent and adaptative processing chains for shoreline extraction in sandy beaches from multiple satellites (including Sentinel-2, Landsat-7, -8, -9, PlanetScope). Tools alike open the possibility of gathering massive collections of shoreline positions at sandy beaches along large periods (from to late 90's to the present) world-wide. The inclusion of the shoreline dynamics in the coastal monitoring system will be a key contribution to the development of ICZM model.

Further considerations

ICZM must be developed from an ecosystemic approach, considering the structure and functioning of the whole ecosystem, and the relationships among its different components, for contributing to the sustainable management of the ecosystem and its resources. This requires the generation of huge volumes of information, a task in

which remote sensing contributes, as shown in this thesis. The development of methods to merge all these data and derive comprehensive and integrated products will be the next steps for the implementation of ICZM. In this sense, proposed solutions need to be supported by coordinated and multidisciplinary processes (Politi *et al.*, 2019), leveraging a combination of cross-disciplinary technologies including remote sensing, Big Data, and data-science methods (Gambín *et al.*, 2021). In this context, the amount of data generated by different monitoring systems (field surveys, automatic samplers, remote sensing, ancillary data) create the perfect backdrop for the use of Artificial Intelligence (AI) approaches (*i.e.* Machine-Learning, Deep Learning). Among the different AI methods, unsupervised and semi-supervised learning (data classification, feature extraction, anomaly detection, pattern recognition), knowledge fusion (combination of theory/physical and data-driven methods), and transfer learning (extrapolatable methods, *in situ* data independence) deserve special attention to exploit the integration of multi-platform, multi-scale and multi-parameter data towards the development of feasible ICZM models. To implement them, combined efforts between agencies, research institutions and regional governments are needed, promoted to develop coordinated models that will yield actionable and reliable information to constitute the future of decision-making systems (Sit *et al.*, 2020).

Chapter 8

CONCLUSIONS

- Sentinel-2 allowed the monitoring of key coastal features close to the time and spatial frames at which they develop, both on land and in aquatic environments. Multiplatform approaches will contribute to overcome the main limitations found in the single-constellation approach (*e.g.,* decreasment of data gaps).

- Atmospheric correction of Sentinel-2 imagery is required for surface reflectance consistency across space and time. For applications in coastal waters, C2XC was the most accurate C2-Net, compared to C2RCC and C2X, which translated into greater reliability for the retrieval of water quality features. A potential blending of C2RCC and C2XC would improve their individual performance.

- Sentinel-2 has the potential to derive credible key water features' estimates. The diffuse attenuation coefficient of light at 490 nm showed high relationship with the Secchi disk depth (proxy for water transparency), albeit it weakens in optically deep waters.

- Spectral indexes including blue or green, and red or red-edge spectral bands provided for chlorophyll-*a* estimates (proxy for phytoplankton biomass) with acceptable accuracy. To overcome uncertainties due to increased suspended particulate and dissolved matter, algorithm-binding approaches based on pixel-wise classification of optical water types are recommended.

- Sentinel-2 is capable of detecting and distinguishing submerged vegetation under certain conditions, modulated by features such as water transparency, vegetation depth, and meadows homogeneity. In clear shallow waters (0-2 m), supervised classification of VIS-NIR composites allowed to depict macroalgae and seagrass coupled dynamics.

- Sentinel-2 has great capabilities for measuring agricultural asset dynamics. The derivative analysis on temporal profiles of common spectral indexes (*i.e.*, NDVI, NDWIs) combined with a rule-based key crop features selection, proved to be a feasible methodology for automatic monitoring of rice phenology, crop yield, and flooding regime up to pixel scale.

- Sentinel-2 is useful for understanding the compound impact of coastal storms. Land inundation mapping, based on semi-supervised classification of NDWI's, and in-water chlorophyll-*a* monitoring, derived from blue to red-edge ratio, provided a holistic overview of Gloria storm' effects in Alfacs bay (*e.g.,* sand barrier breaching, and increased phytoplankton biomass).

- Overall, Sentinel-2 allowed to relate spatiotemporal dynamics of key ecosystem variables with natural and anthropic forcings, with importance for the integrated management of coastal zone resources (*e.g.*, agri-food industry, protected areas).

Bibliography

A

Acharya, T.D., Subedi, A., Lee, D.H., 2018. Evaluation of water indices for surface water extraction in a Landsat 8 scene of Nepal. Sensors 18 (8), 2580.

Alikas, K., Kratzer, S., Noorma, A., Soomets, T., Paavel, B., 2015. Robust remote sensing algorithms to derive the diffuse attenuation coefficient for lakes and coastal waters: Algorithm for diffuse attenuation coefficient. Limnology and Oceanography: Methods 13: 402-415.

Alvado, B., Sòria-Perpinyà, X., Vicente, E., Delegido, J., Urrego, P., Ruíz-Verdú, A., Soria, J.M., Moreno, J., 2021. Estimating Organic and Inorganic Part of Suspended Solids from Sentinel 2 in Different Inland Waters. Water, 13 (18), 2453.

Alvarado-Aguilar, D., Jiménez, J.A., Nicholls, R.J., 2012. Flood hazard and damage assessment in the Ebro Delta (NW Mediterranean) to relative sea level rise. Natural Hazards, 62: 1301-1321.

Amores, A., Marcos, M., Carrió, D. S., Gómez-Pujol, L., 2020. Coastal impacts of storm gloria (January 2020) over the northwestern mediterranean. Natural Hazards Earth Systems Science, 20: 1955-1968.

Ansper, A., Alikas, K., 2019. Retrieval of chlorophyll a from Sentinel-2 MSI data for the European Union water framework directive reporting purposes. Remote Sensing, 11, 64.

APHA., 1998. Standard Methods for the Examination of Water and Wastewater, 20th ed., American Public Health Association: Washington, DC, USA.

Artigas, M.L., Llebot, C., Ross, O.N., Neszi, N.Z., Rodellas, V., Garcia-Orellana, J., Masqué, P., Piera, J., Estrada, M., Berdalet, E., 2014. Understanding the Spatio-Temporal Variability of Phytoplankton Biomass. Distribution in a Microtidal Mediterranean Estuary. Deep Res. Part II Top. Stud. Oceanogr., 101: 180-192.

B

Bakker, W.H., Gorte, B.G.H., Horn, J.A., Janssen, L.L.F., Pohl, C., Parkash, A., Reeves, C. V., Weir, M.J.C., Woldai, T., 2001. Principles of Remote Sensing:

An introductory textbook. ITC Educational Textbook Series 2. The International Institute for Aerospace Survey and Earth Sciences (ITC), Enschede, Netherlands.

Beaver, J. R., Casamatta, D. A., East, T. L., Havens, K. E., Rodusky, A. J., James, R. T., Tausz, C. E., Buccier, K. M., 2013. Extreme weather events influence the phytoplankton community structure in a large lowland subtropical lake (Lake Okeechobee, Florida, USA). Hydrobiologia, 709(1): 213-226.

Berdalet, E, Marrasé, C., Pelegrí, J.L, 2020. Resumen sobre la Formación y Consecuencias de la Borrasca Gloria (19-24 enero 2020). Institut de Ciències del Mar, CSIC, 20 de marzo de 2020, 38.

Berger, M., Moreno, M., Johannessen, J.A., Levelt, P.F., Hanssen, R.F., 2012. ESA's sentinel missions in support of Earth system science. Remote Sens. Environ., 120: 84-90.

Blondeau-Patissier, D., Gower, J.F.R., Dekker, A.G., Phinn, S.R., Brando, V.E., 2014. A Review of Ocean Color Remote Sensing Methods and Statistical Techniques for the Detection, Mapping and Analysis of Phytoplankton Blooms in Coastal and Open Oceans. Prog. Oceanogr., 123: 23-144.

Bolton, D.K., Gray, J.M., Melaas, E.K., Moon, M., Eklundh, L., Friedl, M.A., 2020. Continental-scale land surface phenology from harmonized Landsat 8 and Sentinel-2 imagery. Remote Sensing of Environment, 240, 111685.

Boschetti, M., Busetto, L., Manfron, G., Laborte, A., Asilo, S., Pazhanivelan, S., Nelson, A. 2017. PhenoRice: A method for automatic extraction of spatio-temporal information on rice crops using satellite data time series. Remote Sensing of Environment, 194: 347-365.

Boschetti, M., Busetto, L., Ranghetti, L., Garcia-Haro, J., Campos-Taberner, M., Confalonieri, R. 2018. Testing Multi-Sensors Time Series of Lai Estimates to Monitor Rice Phenology: Preliminary Results. IEEE International Geoscience and Remote Sensing Symposium (IGARSS-2018): 8221-8224.

Boschetti, M., Nutini, F., Manfron, G., Brivio, A., Nelson, A. 2014. Comparative Analysis of Normalised Difference Spectral Indices Derived from MODIS for Detecting Surface Water in Flooded Rice Cropping Systems. PLoS ONE 9 (2): e88741.

Bradley, B.A., Jacob, R.W., Hermance, J.F., Mustard, J.F. 2007. A Curve Fitting Procedure to Derive Inter-Annual Phenologies from Time Series of Noisy Satellite NDVI Data. Remote Sensing of Environment, 106 (2): 137-45.

Blann, K.L., Anderson, J.L., Sands, G.R., Vondracek, B., 2009. Effects of Agricultural Drainage on Aquatic Ecosystems: A Review. CRIT. REV. ENV. SCI. TEC., 39(11): 909-1001.

Brisson, N., Gary, C., Justes, E., Roche, R., Mary, B., Ripoche, D., Zimmer, D., Sierra, J., Bertuzzi, P., Burger, P., Bussière, F., Cabidoche, Y.M., Cellier, P.,

Debaeke, P., Gaudillère, J.P., Hénault, C., Maraux, F., Seguin, B., Sinoquet, H., 2003. An overview of the crop model STICS. Europ J Agro 18(3-4): 309-332.

Brockmann, C., Doerffer, R., Peters, M., Stelzer, K., Embacher, S., Ruescas, A., 2016. Evolution of the C2RCC neural network for Sentinel 2 and 3 for the retrieval of ocean colour products in normal and extreme optically complex waters. In Proceedings of the Living Planet Symposium, Prague, Czech Republic, 9-13 May 2016.

Busch, J.A., 2013. Phytoplankton Dynamics and Bio-Optical Variables Associated with Harmful Algal Blooms in Aquaculture Zones. PhD dissertation, Universität Bremen, Bremen, Germany.

C

Caballero, I., Navarro, G., Ruiz, J., 2018a. Multi-platform assessment of turbidity plumes during dredging operations in a major estuarine system. International Journal of Applied Earth Observation and Geoinformation, 68: 31-41.

Caballero, I., Steinmetz, F., Navarro, G., 2018b. Evaluation of the First Year of Operational Sentinel-2A Data for Retrieval of Suspended Solids in Medium- to High-Turbiditywaters. Remote Sens., 10, 982.

Caballero, I., Fernández, R., Escalante, O.M., Mamán, L., Navarro, G., 2020. New capabilities of Sentinel-2A/B satellites combined with *in situ* data for monitoring small harmful algal blooms in complex coastal waters. Sci. Rep., 10: 1-14.

Camp, J., Delgado, M., 1987. Hidrografía de Las Bahías Del Delta Del Ebro. Investigación Pesquera, Instituto de Ciencias del Mar: Barcelona, Spain, 1987: 351–369.

Campbell, J.W., O'Reilly, J.E., 2006. Metrics for Quantifying the Uncertainty in a Chlorophyll Algorithm: Explicit Equations and Examples Using the OC4.v4 Algorithm and NOMAD Data. Ocean Color Bio-Opt. Algorithm Mini-Workshop, 4: 1-15.

Campos-Taberner, M., García-Haro, F.J., Camps-Valls, G., Grau-Muedra, G., Nutini, F., Busetto, L., Katsantonis, D., Stavrakoudis, D., Minakou, C., Gatti, L., Barbieri, M., Holecz, F., Stroppiana, D., and Boschetti, M., 2017. Exploitation of SAR and Optical Sentinel Data to Detect Rice Crop and Estimate Seasonal Dynamics of Leaf Area Index. Remote Sensing, 9 (3).

Cannizzaro, J.P., Carder, K.L., 2006. Estimating Chlorophyll a Concentrations from Remote-Sensing Reflectance in Optically Shallow Waters. Remote Sens. Environ., 101: 13-24.

Cao, Q., Jianning, Y.M., Yu, S.W., Yuan, F., Cheng, S., Huang, S., Wang, H., Yang, W., and Liu, F., 2016. Improving In-Season Estimation of Rice Yield Potential

and Responsiveness to Topdressing Nitrogen Application with Crop Circle Active Crop Canopy Sensor. Precision Agric., 17: 136-54.

Casanova, D., 1998. Quantifying the Effects of Land Conditions on Rice Growth. A Case Study in the Ebro Delta (Spain) Using Remote Sensing. Wageningen University, The Netherlands.

Cavallo, C., Papa, M.N., Gargiulo, M., Palau-Salvador, G., Vezza, P., Ruello, G., 2021. Continuous Monitoring of the Flooding Dynamics in the Albufera Wetland (Spain) by Landsat-8 and Sentinel-2 Datasets. Remote Sensing, 13, 3525.

Cerralbo, P., F-Pedrera Balsells, M., Mestres, M., Fernández, M., Espino, M., Grifoll, M., Sánchez-Arcilla, A., 2019. Use of a hydrodynamic model for the management of water renovation in a coastal system. Ocean Sci., 15: 215-226.

Chen, Y., Cebrian, J., Lehrter, J., Christiaen, B., Stutes, J., Goff, J., 2017. Storms do not alter long-term watershed development influences on coastal water quality. Marine Pollution Bulletin, 122(1–2), 207.

Coluzzi, R., Imbrenda, V., Lanfredi, M., Simoniello, T., 2018. A First Assessment of the Sentinel-2 Level 1-C Cloud Mask Product to Support Informed Surface Analyses. Remote Sensing of Environment, 217: 426-443.

Copernicus Open Access Hub. Available online: https://scihub.copernicus.eu/ (accessed on 27 September 2021).

Courault, D., Hossard, L., Flamain, F., Baghdadi, N., Irfan, K., 2020. Assessment of agricultural practices from Sentinel 1 and 2 images applied on rice fields to develop a farm typology in the Camargue region. IEEE Journal of Selected Topics in Applied Earth Observations and Remote Sensing, 13: 5027-5035.

Courault, D., Hossard, L., Demarez, V., Dechatre, H., Irfan, K., Braghladi, N., Flamain, F., Ruget, F., 2021. STICS crop model and Sentinel-2 images for monitoring rice growth and yield in the Camargue region. Agron. Sustain. Dev. 41 (49).

Cui, T., Zhang, J., Groom, S., Sun, L., Smyth, T., Sathyendranath, S., 2010. Validation of MERIS ocean-color products in the Bohai Sea: A case study for turbid coastal waters. Remote Sens Environ., 114: 2326–2336.

D

Dall'Olmo, G., Gitelson, A.A., 2005. Effect of Bio-Optical Parameter Variability on the Remote Estimation of Chlorophyll-a Concentration in Turbid Productive Waters: Experimental Results. Applied Optics, 44 (3): 412-422.

Dean, A.M., Populus, J., 2013. Remote Sensing and GIS Integration. Advances in geographic information systems and remote sensing for fisheries and aquaculture., Meaden, G. J., Aguilar-Manjarrez, J., Eds., 35-41.

Dekker, A., Brando, V., Anstee, J., Fyfe, S., Malthus, T., Karpouzli, E., 2006, Remote Sensing of Seagrass Ecosystems: Use of Spaceborne and Airborne Sensors, Seagrasses: biology, ecology and conservation. Dordrecht, Springer: 347-359.

Del López-Rodríguez, M.C., Leira, M., Valle, R., Moyà-Niell, G., 2016. El Fitoplancton Como Indicador de Calidad de Masas de Agua Muy Modificadas En La DMA. El Lago Artificial de As Pontes (A Coruña. España). Nov. Acta Científica Compostel. 23: 85-97.

Doerffer, R., Schiller, H., 2007. The MERIS Case 2 water algorithm. International Journal of Remote Sensing, 28.

Dogliotti, A., Ruddick, K., 2011. Improving Water Reflectance Retrieval from MODIS Imagery in the Highly Turbid Waters of La Plata River. VI International Conference in Current Problems in Optics of Natural Waters, St. Petersburg, Russia.

Dogliotti, A.I., Ruddick, K.G., Nechad, B., Doxaran, D., Knaeps, E., 2015. A single algorithm to retrieve turbidity from remotely-sensed data in all coastal and estuarine waters. Remote Sensing of Environment, 156: 157-168.

Dong, J., Xiao, X., 2016. Evolution of Regional to Global Paddy Rice Mapping Methods: A Review. ISPRS Journal of Photogrammetry and Remote Sensing 119: 214–27.

Dörnhöfer, K., Klinger, P., Heege, T., Oppelt, N., 2018. Multi-sensor satellite and *in situ* monitoring of phytoplankton development in a eutrophic-mesotrophic lake. Sci. Total Environ., 612: 1200-1214.

Duarte, P., Fernández-Reiriz, M.J., Labarta, U., 2012. Modelling Mussel Growth in Ecosystems with Low Suspended Matter Loads Using a Dynamic Energy Budget Approach. J. Sea Res., 67: 44-57.

E

ESA Step Forum. C2X-Complex. Available online: https://forum.step.esa.int/t/c2x-complex/29392 (accessed on 27 September 2021).

ESA., 2017. European Space Agency, Sentinel-2 Spatial Resolution. Available online: https://earth.esa.int/web/sentinel/user-guides/sentinel-2-msi/resolutions/spatial (accessed on 01 June 2019).

ESA S2-SRF v2.0. European Space Agency, Sentinel-2 Spectral Response Functions v2.0. Available online: https://earth.esa.int/web/sentinel/user-guides/sentinel-2-msi/document-library/asset_publisher/Wk0TKajiISaR/content/sentinel-2a-spectralresponses (accessed on 16 April 2020).

European Comission, 2002. The European Parliament and the Council of the

European Union. Recommendation of the European Parliament and of the Council Concerning the Implementation of Integrated Coastal Zone Management in Europe. Off. J. Eur. Communities 2002, 2001 (April), 24-27.

F

Fabbri, K.P., 1998. A methodology for supporting decision making in integrated coastal zone management. Ocean Coast. Manag., 39: 51-62.

Fernández-Beltran, R., Baidar, T., Kang, J., Pla, F., 2021. Rice-Yield Prediction with Multi-Temporal Sentinel-2 Data and 3D CNN: A Case Study in Nepal. Remote Sensing, 13, 1391.

Fernández-Gambín, A., Angelats, E., Soriano-González, J., Miozzo, M., Dini, P., 2021. Sustainable Marine Ecosystems: Deep Learning for Water Quality Assessment and Forecasting. IEEE Access, 9: 121344-121365.

Fernández-Montblanc, T., Gómez-Enri, J., Ciavola, P., 2020. The Role of Mean Sea Level Annual Cycle on Extreme Water Levels Along European Coastline. Remote Sensing. 2020, 12, 3419.

Forget, M.H., Stuart, V., Platt, T., 2009. Reports and Monographs of the International Ocean-Colour Coordinating Group (IOCCG). Remote Sensing in Fisheries and Aquaculture, 8, 1-128.

Fulton, M., 1993. Cereal and wool production in the Esperance Sandplain area of Western Australia: The need for a systems approach for sustainable agriculture, Am. J. Alternative Agr., 2 (8): 85-90.

G

Gao, B.C., 1996. NDWI - A Normalized Difference Water Index for Remote Sensing of Vegetation Liquid Water from Space. Remote Sensing of Environment, 7212: 257-66.

Gao, F., Hilker, T., Zhu, X., Anderson, M., Masek, J., Wang, P., Yang, Y., 2015. Fusing Landsat and MODIS Data for Vegetation Monitoring. IEEE Geoscience and Remote Sensing Magazine, 3 (3): 47-60.

Garcia, L.E., Rodriguez, D.J., Wijen, M., Pakulski, I. 2016. Earth Observation for Water Resources Management: Current Use and Future Opportunities for the Water Sector. World Bank Group, Washington, DC, USA.

Geng, L., Ma, M., Wang, X., Yu, W., Jia, S., Wang, H., 2014. Comparison of Eight Techniques for Reconstructing Multi-Satellite Sensor Time series NDVI Data Sets in the Heihe River Basin, China. Remote Sensing, 6 (3): 2024-2049.

Genua-Olmedo, A., Alcaraz, C., Caiola, N., Ibáñez, C., 2016. Sea level rise impacts

on rice production: the ebro delta as an example. Sci. Total Environ., 571: 1200-1210.

Gernez, P., Doxaran, D., Barillé, L., 2017. Shellfish Aquaculture from Space: Potential of Sentinel2 to Monitor Tide-Driven Changes in Turbidity, Chlorophyll Concentration and Oyster Physiological Response at the Scale of an Oyster Farm. Front. Mar. Sci., 4: 1-15.

Gernez, P., Lafon, V., Lerouxel, A., Curti, C., Lubac, B., Cerisier, S., Barillé, L., 2015. Toward Sentinel-2 high resolution remote sensing of suspended particulate matter in very turbid waters: SPOT4 (Take5) experiment in the Loire and Gironde estuaries. Remote Sensing, 7: 9507-9528.

Gholizadeh, M., Melesse, A., Reddi, L., 2016. A Comprehensive Review on Water Quality Parameters Estimation Using Remote Sensing Techniques. Sensors, 16, 1298.

Gitelson, A., Nikanorov, A., Szabo, G., Szilagyi, F., 1986. Etude de La Qualite Des Eaux de Surface Télédétéction. In Monitoring to Detect Chamges in Water Quality Series, IAHS Publication, 157, Budapest, Hungary: 111-121.

Gitelson, A.A., Kondratyev, K.Y., 1991. Optical Models of Mesotrophic and Eutrophic Water Bodies. Int. J. Remote Sens., 12: 373-385.

Gitelson, A.A., Yacobi, Y.Z., Karnieli, A., Nurit, K., 1996a. Reflectance Spectra of Polluted Marine Waters in Haifa Bay, Southeastern Mediterranean: Features and Application for Remote Estimation of Chlorophyll Concentration. J. Earth Sci., 45: 127-136.

Gitelson, A.A., Kaufman, Y.J., Merzlyak, M.N., 1996b. Use of Green Channel in Remote Sensing of Global Vegetation from EOS-MODIS. Remote Sensing of Environment 58 (3): 289-98.

Gitelson, A.A., Dall'Olmo, G., Moses, W., Rundquist, D.C., Barrow, T., Fisher, T.R., Gurlin, D., Holz, J., 2008. A Simple Semi-Analytical Model for Remote Estimation of Chlorophyll-a in Turbid Waters: Validation. Remote Sens. Environ., 112: 3582-3593.

Gitelson, A.A., Gao, B.C., Li, R.R., Berdnikov, S., Saprygin, V., 2011. Estimation of chlorophyll-a concentration in productive turbid waters using a Hyperspectral Imager for the Coastal Ocean: The Azov Sea case study. Environ. Res. Lett., 6: 1-6.

Goffi, A., Stroppiana, D., Brivio, P.A., Bordogna, G., Boschetti, M., 2020. Towards an automated approach to map flooded areas from Sentinel-2 MSI data and soft integration of water spectral features. International Journal Applied Earth Observation and Geoinfo., 84, 101951,

Gons, H.J., Rijkeboer, M., Ruddick, K.G., 2002. A Chlorophyll-Retrieval Algorithm for Satellite Imagery (Medium Resolution Imaging Spectrometer) of Inland and Coastal Waters. J. Plankton Res., 24: 947-951.

Gons, H.J., Rijkeboer, M., Ruddick, K.G., 2005. Effect of a waveband shift on chlorophyll retrieval from MERIS imagery of inland and coastal waters. J. Plankton Res., 27, 125-127.

Gons, H.J., Auer, M.T., Effler, S.W., 2008. MERIS Satellite Chlorophyll Mapping of Oligotrophic and Eutrophic Waters in the Laurentian Great Lakes. Remote Sens. Environ., 112, 4098–4106.

González, M. (coord.), 2020: El temporal Gloria (19-23/01/2020): Els efectes dels processos geològics sobre el territori, 122 pàg. Col·lecció: Monografies tècniques 8. Institut Cartogràfic I Geològic de Catalunya.

Gordon, H.G., Morel, A., 1983. Remote assessment of ocean color for interpretation of satellite visible imagery: A review. Springer: New York. USA, 114.

Gorelick, N., Hancher, N., Dixon, M., Ilyushchenko, S., Thau, D., Moore, R., 2017. Google Earth Engine: Planetary-Scale Geospatial Analysis for Everyone. Remote Sensing of Environment 202: 18-27.

Gower, J.F.R., Doerffer, R., Borstad, G.A.,1999. Interpretation of the 685 nm Peak in Water-Leaving Radiance Spectra in Terms of Fluorescence, Absorption and Scattering, and Its Observation by MERIS. Int. J. Remote Sens., 20: 1771-1786.

Gracia, V., García, M., Grifoll, M. and Sánchez-Arcilla, A., 2013. Breaching of a barrier beach under extreme events. The role of morphodynamic simulations. Journal of Coastal Research, 65: 951-956.

Grant, J., Bacher, C., Ferreira, J.G., Groom, S., Morales, J., Rodriguez-Benito, C., .Saitoh, S., Sathyendranath, S., Stuart, V., 2009. Remote sensing applications in marine aquaculture. Remote sensing in fisheries and aquaculture. Reports of the International Ocean Colour Coordinatng Group (IOCCG), 8: 77-88.

Green, E., Short, F., 2003. World Atlas of Seagrasses, UNEP World Conservation Monitoring Centre, 298, Berkeley, University of California Press.

Gregor, J., Maršálek, B., 2004. Freshwater phytoplankton quantification by chlorophyll a: a comparative study of in vitro, *in vivo* and *in situ* methods. Water Res., 38: 517-522.

Grizonnet, M., Michel, J., Poughon, V., Inglada, J., Savinaud, M., Cresson, R., 2017. Orfeo ToolBox: open source processing of remote sensing images. Open geospatial data softw. stand., 2, 15.

Gullström, M., Lundén, B., Bodin, M., Kangwe, J., Öhman, M.C., Mtolera, M.S.P., Björk, M., 2006. Assessment of Changes in the Seagrass-Dominated Submerged Vegetation of Tropical Chwaka Bay (Zanzibar) Using Satellite Remote Sensing. Estuar. Coast. Shelf Sci., 67 (3): 399-408.

Gurlin, D., Gitelson, A.A., Moses, W.J., 2011. Remote Estimation of Chl-a Concentration in Turbid Productive Waters-Return to a Simple Two-Band NIR-Red Model. Remote Sens. Environ., 115: 3479–3490.

H

Habbane, M., ElSabh, M.I., Dubois, J.M., 1997. Determination of potential for aquaculture activities via passive teledetection and a grid-based geographical information system - Application to coastal waters to the Baie-des-Chaleurs (Eastern Canada). International Journal of Remote Sensing, 18: 3439-3457.

Harmel, T., Chami, M., Tormos, T., Reynaud, N., Danis, P.A., 2018. Sunglint Correction of the Multi-Spectral Instrument (MSI)-Sentinel-2 Imagery over Inland and Sea Waters from SWIR Bands. Remote Sens. Environ., 204, 308–321.

Harvey, E.T., Krause-Jensen, D., Stæhr, P.A., Groom, G.B., Hansen, L.B., 2018. Literature review of remote sensing technologies for coastal chlorophyll-a observations and vegetation coverage. Part of ReSTEK (Brug af Remote Sensing teknologier til opgørelse af klorofylkoncentrationer og vegetationsudbredelse i danske kystvande) and DCE Remote sensing in coastal area projects. Aarhus University, DCE-Technical Report from DCE, Danish Centre for Environment and Energy, 112.

Hemminga, M., Duarte, C., 2000. Seagrass Ecology, Cambridge, Cambridge University Press.

Hernández, W.J., Ortiz-Rosa, S., Armstrong, R.A., Geiger, E.F., Eakin, C.M., Warner, R.A., 2020. Quantifying the Effects of Hurricanes Irma and Maria on Coastal Water Quality in Puerto Rico using Moderate Resolution Satellite Sensors. Remote Sensing., 12: 964.

Hinkel, J., Lincke, D., Vafeidis, AT., Perrette, M., Nicholls, RJ., Tol, R. S.J., Marzeion, B., Ionescu, C., Levermann, A., 2014. Coastal flood damage and adaptation costs under 21st century sea-level rise. Proceedings of the National Academy of Sciences, 111: 3292-3297.

Hinton, J.C., 1996. GIS and Remote Sensing Integration for Environmental Applications. Int. J. Geogr. Inf. Syst., 10 (7): 877–890.

Hoepffner, N., Zibordi, G. Remote Sensing of Coastal Waters. Encycl. Ocean Sci. 2010, 732–741.

Holmes, R., 1970. The Secchi disk in turbid coastal waters. Limnol Oceanogr., 15: 688-694.

Hossain, M.S., Bujang, J.S., Zakaria, M.H., Hashim, M., 2015. The Application of Remote Sensing to Seagrass Ecosystems: An Overview and Future Research Prospects. Int. J. Remote Sens., 36 (1): 61-114.

Huang, W., Mukherjee, D., Chen, S., 2011. Assessment of Hurricane Ivan impact on chlorophyll-a in Pensacola Bay by MODIS 250m remote sensing. Marine Pollution Bulletin, 62 (3): 490-498.

Huang, M., Jin S., 2020. Rapid Flood Mapping and Evaluation with a Supervised Classifier and Change Detection in Shouguang Using Sentinel-1 SAR and Sentinel-2 Optical Data. Remote Sensing., 12(13): 2073.

Huete, A., Didan, K., Miura, T., Rodriguez, E., Gao, X., Ferreira, L., 2002. Overview of the Radiometric and Biophysical Performance of the MODIS Vegetation Indices. Remote Sens. Environ., 83: 195-213.

Huot, Y., Babin, M., Bruyant, F., Grob, C., Twardowski, M.S., Claustre, H., 2007. Relationship between photosynthetic parameters and different proxies of phytoplankton biomass in the subtropical ocean. Biogeosciences, 4: 853-868

Hwang, C., Chang, C.H., Burch, M., Fernandes, M., Kildea, T., 2019. Effects of Epiphytes and Depth on Seagrass Spectral Profiles: Case Study of Gulf St. Vincent, South Australia., Int. J. Environ. Res. Public Health, 16, 2701: 1-16.

I

Ibañez, C., Alcaraz, C., Caiola, N., Prado, P., Trobajo, R., Benito, X., Day, J.W., Reyes, E., Syvitski, J.P.M., 2019. Basin-scale land use impacts on world deltas: Human vs natural forcings. Global and Planetary Change, 173, 24-32.

IOCCG., 2010. Atmospheric Correction for Remotely-Sensed Ocean Colour Products. Wang, M., Ed., Reports of the International Ocean-Colour Coordinating Group, 10, Darmouth, Canada.

J

Jeffrey, S.W., Humphrey, G.F., 1975. New Spectrophotometric Equations for Determining Chlorophylls a, b, C1 and C2 in Higher Plants, Algae and Natural Phytoplankton. Biochem. Physiol. Pflanz., 167: 191-194.

Jiménez, J.A., Gracia, V., Valdemoro, H.I., Mendoza, E.T., Sánchez-Arcilla, A., 2011. Managing erosion-induced problems in NW Mediterranean urban beaches. Ocean & Coastal Management 54 (12), 907-918.

Jimenez, J.A, 2020. Dinàmica litoral, efectes dels temporals i comportament de les platges. Chapter of: "Sobre el temporal Gloria (19-23.01.20), els seus efectes sobre el país i el que se'n deriva: Report de Resposta Ràpida (R3)". Institut d'Estudis Catalans, 55-72.

Joshi, I.D., D'Sa, E.J., Osburn, C.L., Bianchi, T.S., 2017. Turbidity in Apalachicola Bay, Florida from Landsat 5 TM and Field Data: Seasonal Patterns and Response to Extreme Events. Remote Sens., 9, 367.

K

Kanamitsu, M., Ebisuzaki, W., Woollen, J., Yang, S.K., Hnilo, J.J., Fiorino, M., Potter, G.L., 2002. NCEP-DOE AMIP-II Reanalysis (R-2). Bull. Am. Meteorol. Soc., 83: 1631-1643.

Klemas, V.V., 2013. Remote Sensing of Coastal Hazards.Finkl, C. (eds) Coastal Hazards. Coastal Research Library, 1000. Springer, Dordrecht.

Knudby, A, Nordlund, L, 2011. Remote Sensing of Seagrasses in a Patchy Multi-Species Environment, Int. J. Remote Sens., 32 (8), 2227-2244.

Kutser, T., Paavel, B., Verpoorter, C., Ligi, M., Soomets, T., Toming, K., Casal, G., 2016. Remote Sensing of Black Lakes and Using 810 Nm Reflectance Peak for Retrieving Water Quality Parameters of Optically Complex Waters. Remote Sens., 8, 497.

De Keukelaere, L., Sterckx, S., Adriaensen, S., Knaeps, E., Reusen, I., Giardino, C., Bresciani, M., Hunter, P., Neil, C., Van Der Zande, D., Vaiciute, D., 2018. Atmospheric correction of Landsat-8/OLI and Sentinel-2/MSI data using iCOR algorithm: Validation for coastal and inland waters. Eur. J. Remote Sens., 51: 525-542.

L

Le, C., Hu, C., Cannizzaro, J., English, D., Muller-Karger, F., Lee, Z., 2013. Evaluation of Chlorophyll-a Remote Sensing Algorithms for an Optically Complex Estuary. Remote Sens. Environ., 129: 75-89.

Li, J., Roy, D., 2017. A global analysis of Sentinel-2A, Sentinel-2B and Landsat-8 data revisit intervals and implications for terrestrial monitoring. Remote Sens. 9, 902.

Ligi, M., Kutser, T., Kallio, K., Attila, J., Koponen, S., Paavel, B., Soomets, T., Reinart, A., 2017. Testing the Performance of Empirical Remote Sensing Algorithms in the Baltic Sea Waters with Modelled and *in situ* Reflectance Data. Oceanologia., 59 (1): 57-68.

Lins, R.C., Martinez, J.M., da M. Marques, D., Cirilo, J.A., Fragoso, C.R., 2017. Assessment of Chlorophyll-a Remote Sensing Algorithms in a Productive Tropical Estuarine-Lagoon System. Remote Sens., 9 (6): 1-19.

Liu Y, Islam MA, Gao J., 2003. Quantification of shallow water quality parameters by means of remote sensing. Progress in Physical Geography: Earth and Environment, 27(1): 24-43.

Liu, L., Xiao, X., Qin, Y., Wang, J., Xu, X., Hu, Y., Qiao, Z., 2020. Mapping cropping intensity in China using time series Landsat and Sentinel-2 images and Google Earth Engine. Remote Sensing of Environment, 239, 111624.

Liu, S., Liu, X., Liu, M., Wu, L., Ding, C., Huang, Z. 2017. Extraction of rice phenological differences under heavy metal stress using EVI time series from

HJ-1A/B data. Sensors (Switzerland) 17, 1-17.

Llebot, C., Rueda, F.J., Solé, J., Artigas, M.L., Estrada, M., 2014. Hydrodynamic States in a Wind-Driven Microtidal Estuary (Alfacs Bay). J. Sea Res., 85, 263-276.

Llebot, C., Solé, J., Delgado, M., Fernández-Tejedor, M., Camp, J., Estrada, M., 2011. Hydrographical Forcing and Phytoplankton Variability in Two Semi-Enclosed Estuarine Bays. J. Mar. Syst., 86, 69-86.

Lorenzen, C.J., 1996. A Method for the Continuous Measurement of *in vivo* Chlorophyll Concentration. Deep Res., 13, 223-227.

Lyzenga, D., Malinas, N.P., Tanis, F.J., 2006. Multispectral bathymetry using a simple physically based algorithm. Geoscience and Remote Sensing, IEEE Transactions on. 44: 2251-2259.

M

Main-Knorn, M., Pflug, B., Louis, J., Debaecker, V., Müller-Wilm, U., Gascon, F., 2017. Sen2Cor for Sentinel-2. SPIE 10427, Image and Signal Processing for Remote Sensing XXIII, 1042704.

Malenovský, Z., Rott, H., Cihlar, J., Schaepman, M.E., García-Santos, G., Fernandes, R., Berger, M., 2012. Sentinels for Science: Potential of Sentinel-1, -2, and -3 Missions for Scientific Observations of Ocean, Cryosphere, and Land. Remote Sens. Environ., 120: 91-101.

Martínez-Eixarch, M., Curcó A. and Ibañez, C. 2016. Effects of agri-environmental and organic rice farming on yield and macrophyte community in Mediterranean paddy fields. Paddy Water Environment 15: 457-468.

Martínez-Eixarch, M., Alcaraz, C., Viñas, M., Noguerol, J., Aranda, X., Prenafeta-Boldu, F.X., Saldaña-De la Vega, J.A., Catala, M.M., Ibañez, C., 2018. Neglecting the Fallow Season Can Significantly Underestimate Annual Methane Emissions in Mediterranean Rice Fields. PLoS ONE 13 (8): e0202159.

Mascaró, O., Romero, J., Pérez, M., 2014, Seasonal Uncoupling of Demographic Processes in a Marine Clonal Plant, Estuar. Coast. Shelf Sci., 142: 23–31.

Mateo-García, G., Gómez-Chova, L., Amorós-López, J., Muñoz-Marí, J., Camps-Valls, G., 2018. Multitemporal Cloud Masking in the Google Earth Engine. Remote Sensing, 10 (7):1079.

Matgen, P., Martinis, S., Wagner, W., Freeman, V., Zeil, P., McCormick, N., 2020. Feasibility assessment of an automated, global, satellite-based flood-monitoring product for the Copernicus Emergency Management Service. Publications Office of the European Union, Luxembourg.

Matthews, M.W., 2011. A Current Review of Empirical Procedures of Remote

Sensing in Inland and Near-Coastal Transitional Waters. Int. J. Remote Sens., 32: 6855-6899.

Matthews, M.W., Bernard, S., Robertson, L., 2012. An Algorithm for Detecting Trophic Status (Chlorophyll-a), Cyanobacterial-Dominance, Surface Scums and Floating Vegetation in Inland and Coastal Waters. Remote Sens. Environ., 124: 637-652.

McFeeters, S.K., 1996. The Use of the Normalized Difference Water Index (NDWI) in the Delineation of Open Water Features. International Journal of Remote Sensing 17 (7): 1425-32.

Mishra, S., Mishra, D.R., 2012. Normalized Difference Chlorophyll Index: A Novel Model for Remote Estimation of Chlorophyll-a Concentration in Turbid Productive Waters. Remote Sens. Environ., 117: 394-406.

Misra, G., Cawkwell, F., Wingler, A., 2020. Status of Phenological Research Using Sentinel-2 Data: A Review. Remote Sensing 12 (17): 10–14.

Mobley, C.D., 1999. Estimation of the remote-sensing reflectance from above-surface measurements. Appl. Opt., 38: 7442-7455.

Moore, T.S., Dowell, M.D., Bradt, S., Ruiz-Verdú, A., 2014. An optical water type framework for selecting and blending retrievals from bio-optical algorithms in lakes and coastal waters. Remote Sens Environ., 143: 97–111.

Morel, A., Prieur, L., 1977. Analysis of Variations in Ocean Color. Limnol. Oceanogr., 22: 709-722.

Moreno-García, B., Casterad, M.A., Guillén, M., Quílez, D., 2018. Agronomic and Economic Potential of Vegetation Indices for Rice N Recommendations under Organic and Mineral Fertilization in Mediterranean Regions. Remote Sensing 10 (12).

Mosleh, M.K., Hassan, Q.K., Chowdhury, E.H., 2015. Application of Remote Sensors in Mapping Rice Area and Forecasting Its Production: A Review. Sensors (Switzerland) 15 (1): 769–91.

Mostert, E., 2003. The European Water Framework Directive and water management research. Phys Chem Earth A/B/C., 28, 523-527.

Müller, D., Krasemann, H., Brewin, R.J.W., Brockmann, C., Deschamps, P.Y., Doerffer, R., Fomferra, N., Franz, B.A., Grant, M.G., Groom, S.B., Mélin, F., Platt, T., Regner, P., Sathyendranath, S., Steinmetz, F., Swinton, J., 2015. The Ocean Colour Climate Change Initiative: I. A methodology for assessing atmospheric correction processors based on *in situ* measurements. Remote Sens Environ., 162, 242–256.

Müller-Wilm, U., 2016. Sen2Cor Configuration and User Manual, Eur. Sp. Agency, Ref. S2-PDGS-MPC-L2A- SUM-V2.3, 1.

N

NASA, 2018. Goddard Space Flight Center, Ocean Ecology Laboratory, Ocean Biology Processing Group: Ancillary Meteorological Ocean Color Data, NASA OB. DAAC.

NASA Ocean Color Data. Available online: https://oceandata.sci.gsfc.nasa.gov (accessed September 2021).

Nechad B., Ruddick, K.G., Park, Y., 2010. Calibration and validation of a generic multisensor algorithm for mapping of total suspended matter in turbid waters. Remote Sens Environ., 114: 854-866.

Nicholls, R.J., Wong, P.P., Burkett, V., Codignotto, J., Hay, J., McLean, R., Saito, Y., 2007. Coastal systems and low-lying areas. Climate Change: Impacts, Adaptation and Vulnerability: Contribution of Working Group II to the Fourth Assessment Report of the Intergovernmental Panel on Climate Change. Cambridge University Press, Cambridge, UK: 315-356.

Niroumand-Jadidi, M., Bovolo, F., Bruzzone, L., Gege, P., 2021. Inter-Comparison of Methods for Chlorophyll-a Retrieval: Sentinel-2 Time series Analysis in Italian Lakes. Remote Sens., 13, 2381.

Nordlund, L.M., Koch, E.W., Barbier, E.B., Creed J.C., 2016. Seagrass Ecosystem Services and Their Variability across Genera and Geographical Regions. PLoS ONE, 11(10): 1-17.

Novoa, S., Doxaran, D., Ody, A., Vanhellemont, Q., Lafon, V., Lubac, B., Gernez, P., 2017. Atmospheric Corrections and Multi-Conditional Algorithm for Multi-Sensor Remote Sensing of Suspended Particulate Matter in Low-to-High Turbidity Levels Coastal Waters. Remote Sens., 9, 61.

Ngoc, D.D., Loisel, H., Jamet, C., Vantrepotte, V., Duforêt-Gaurier, L., Minh, C.D., Mangin, A., 2019. Coastal and inland water pixels extraction algorithm (WiPE) from spectral shape analysis and HSV transformation applied to Landsat 8 OLI and Sentinel-2 MSI. Remote Sensing of Environment., 223: 208-228.

O

Odermatt, D., Gitelson, A., Brando, V.E., Schaepman, M., 2012. Review of Constituent Retrieval in Optically Deep and Complex Waters from Satellite Imagery. Remote Sens. Environ., 118: 116-126.

Oliveira, E.N., Fernandes, A.M., Kampel, M., Cordeiro, R.C., Brandini, N., Vinzon, S.B., Grassi, R.M., Pinto, F.N., Fillipo, A.M., Paranhos, R., 2016.

Assessment of Remotely Sensed Chlorophyll- a Concentration in Guanabara Bay, Brazil. J. Appl. Remote Sens., 10, 026003.

O'Mahony, C., Gray, S., Gault, J., Cummins, V., 2022. ICZM as a framework for climate change adaptation action- Experience from Cork Harbour, Ireland. Marine Policy, 111, 102223.

O'Reilly J.E., Werdell, P.J., 2019. Chlorophyll algorithms for ocean color sensors- OC4, OC5 & OC6. Journal of Remote sensing of environment, 229: 32-47.

Ozesmi, S.L., Bauer, M.E, 2002. Satellite remote sensing of wetlands. Wetlands Ecology and Management, 10: 381-402.

P

Pahlevan, N., Mangin, A., Balasubramanian, S. V., Smith, B., Alikas, K., Arai, K., Barbosa, C., Bélanger, S., Binding, C., Bresciani, M., Giardino, C., Gurlin, D., Fan, Y., Harmel, T., Hunter, P., Ishikaza, J., Kratzer, S., Lehmann, M.K., Ligi, M., Ma, R., Martin-Lauzer, F.R., Olmanson, L., Oppelt, N., Pan, Y., Peters, S., Reynaud, N., Sander de Carvalho, L.A., Simis, S., Spyrakos, E., Steinmetz, F., Stelzer, K., Sterckx, S., Tormos, T., Tyler, A., Vanhellemont, Q., Warren, M., 2021. ACIX-Aqua: A global assessment of atmospheric correction methods for Landsat-8 and Sentinel-2 over lakes, rivers, and coastal waters. Remote Sens Environ., 258, 112366.

Pekel, J.F., Vancutsem, C., Bastin, L., Clerici, M., Vanbogaert, E., Bartholomé, E., Defourny, P., 2014. A near real-time water surface detection method based on HSV transformation of MODIS multi-Spectral time series data. Remote Sensing Environment. 140: 704-716.

Pereira-Sandoval, M., Ruescas, A.B., Urrego, P., Ruiz-Verdú, A., Tenjo, C., Soria-Perpinyà, X., Vicente, E., Soria, J.M., Moreno, J., 2019. Evaluation of Atmospheric Correction Algorithms over Spanish inland waters for Sentinel-2 MSI data. Remote Sens., 11(12), 1469.

Pérez, M., Camp, J., 1986. Distribución Espacial y Biomasa de Las Fanerógamas Marinas de Las Bahías Del Delta Del Ebro, Inv.Pesq.: 519-530.

Petus, C, Collier, C, Devlin, M, Rasheed, M, McKenna, S, 2014, Using MODIS Data for Understanding Changes in Seagrass Meadow Health: A Case Study in the Great Barrier Reef (Australia), Mar. Environ. Res., 98, 68–85.

Phiri, D., Simwanda, M., Salekin, S., Nyirenda, V.R., Murayama, Y., Ranagalage, M., 2020. Sentinel-2 Data for Land Cover/Use Mapping: A Review. Remote Sens., 12, 2291.

Politi, E., Paterson, S.K., Scarrott, R., Tuohy, E., O'Mahony, C., Cámaro-García, W.C.A., 2019. Earth observation applications for coastal sustainability: Potential and challenges for implementation. Anthropocene Coasts, 2 (1), 306329.

Poole, H.H., Atkins, W.R.G., 1929. Photoelectric measurements of submarine illumination throughout the year. Journal of the Marine Biological Association of the UK, 16(01): 297-324.

Prat, N., Muñoz, I., Camp, J., Comin, F.A., Lucena, J.R., Romero, J., Vidal, M., 1988. Seasonal Changes in Particulate Organic Carbon and Nitrogen in the River and Drainage Channels of the Ebro Delta (N.E. Spain). SIL Proc., 23: 1344-1349.

Prieur, L., Sathyendranath, S., 1981. An optical classification of coastal and oceanic waters based on the specific spectral absorption curves of phytoplankton pigments, dissolved organic matter, and other particulate materials. Limnology and Oceanography, 26.

Pu, R., Bell, S., Meyer, C., Baggett, L., Zhao, Y., 2012, Mapping and Assessing Seagrass along the Western Coast of Florida Using Landsat TM and EO-1 ALI/Hyperion Imagery. Estuar. Coast. Shelf Sci., 115: 234-245.

R

Radiarta, I.N., Saitoh, S.-I., 2009. Biophysical models for Japanese scallop, Mizuhopecten yessoensis, aquaculture site selection in Funka Bay, Hokkaido, Japan, using remotely sensed data and geographic information system. Aquaculture International, 17: 403-419.

Ramírez-Pérez, M., Gonçalves-Araujo, R., Wiegmann, S., Torrecilla, E., Bardaji, R., Röttgers, R., Bracher, A., Piera, J., 2017. Towards Cost-Effective Operational Monitoring Systems for Complex Waters: Analyzing Small-Scale Coastal Processes with Optical Transmissometry. PLoS One, 12 (1): 1-21.

Ramón, M., Cano, J., Peña, J.B., Campos, M.J., 2005. Current Status and Perspectives of Mollusc (Bivalves and Gastropods) Culture in the Spanish Mediterranean. Boletín Inst. Español Oceanogr., 21: 361-373.

Ramón, M., Fernández, M., Galimany, E., 2007. Development of Mussel (Mytilus Galloprovincialis) Seed from Two Different Origins in a Semi-Enclosed Mediterranean Bay (N.E. Spain). Aquaculture, 264: 148-159.

Ranson, K.J., 1975. Computer assisted classification of mixtures with simulated spectral signatures. Dissertation (Master of Science)- Colorado State University, Fort Collins.

RCoreTeam., 2017. R: A Language and Environment for Statistical Computing. Vienna, Austria: R Foundation for Statistical Computing.

Renosh, P., Doxaran, D., Keukelaere, L., Gossn, J., 2020. Evaluation of Atmospheric Correction Algorithms for Sentinel-2-MSI and Sentinel-3-OLCI in Highly Turbid Estuarine Waters. Remote Sens., 12 (8), 1285.

Rikimaru, A., Roy, P.S., and Miyatake, S., 2002. Tropical Forest Cover Density Mapping. Tropical Ecology 43 (1): 39-47.

Rodríguez-Santalla, I., Gomez-Ortiz, D., Martín-Crespo, T., Sánchez, M.J., Montoya-Montes, I., Martín-Velázquez, S., Barrio, F., Serra, J., Ramírez-Cuesta, J.M., Gracia, F.J., 2021. Study and Evolution of the Dune Field of La Banya Spit in Ebro Delta (Spain) Using LiDAR Data and GPR. Remote Sensing, 13, 802.

Rouse, J.W., Haas, R.H., Schell, J.A., Deering, D.W., 1974. Monitoring Vegetation Systems in the Great Plains with ETRS. Third Earth Resources Technology Satellite-1 Symposium, 309-17. Washington DC: Goddard Space Flight Center, NASA SP-351, Science and Technical Information office, NASA.

Rovira, A., Alcaraz, C., Ibañez, C., 2012. Spatial and temporal dynamics of suspended load at-a-cross-section: The lowermost Ebro River (Catalonia, Spain). Water Research, 46 (11), 3671-3681.

S

Sakamoto, T., Yokozawa, M., Toritani, H., Shibayama, M., Ishitsuka, N., Ohno, H., 2005. A Crop Phenology Detection Method Using Time series MODIS Data. Remote Sensing of Environment, 96 (3-4): 366–74.

Sánchez, B., Rasmussen, A., and Porter, J.R., 2013. Temperatures and the Growth and Development of Maize and Rice: A Review. Global Change Biology 20 (2): 408-17.

Sánchez-García, E., Palomar-Vázquez, J.M., Pardo-Pascual, J.E., Almonacid-Caballer, J., Cabezas-Rabadán, C., Gómez-Pujol, L., 2020. An efficient protocol for accurate and massive shoreline definition from mid-resolution satellite imagery. Coastal Engineering, 160, 103732.

Sánchez-García, M.J., Montoya-Montes, I., Casamayor, M., Alonso, I., Rodríguez-Santalla, I., 2019. Coastal Dunes in the Ebro Delta. Morales, J. (eds) The Spanish Coastal Systems. Springer, Cham.

Sanmartí, N., Solé, L., Romero, J., Pérez, M., 2018. Seagrass-Bivalve Facilitative Interactions: Trait-Mediated Effects along an Environmental Gradient. Mar. Environ. Res., 133: 99-104.

Sayol, J.M., Marcos, M., 2018. Assessing flood risk under sea level rise and extreme sea levels scenarios. Application to the Ebro Delta (Spain). Journal of Geophysical Research: Oceans, 123, 794–811.

Schmitt, M., Hughes, L.H., Qiu, C., and Zhu, X., 2019. Aggregating Cloud-Free Sentinel-2 Images with Google Earth Engine. ISPRS Annals of Photogrammetry, Remote Sensing and Spatial Information Sciences IV-2/W7: 145–52.

Seegers, B.N., Stumpf, R.P., Schaeffer, B.A., Loftin, K.A., Jeremy Werdell, P., 2018. Performance Metrics for the Assessment of Satellite Data Products: An Ocean Color Case Study. Opt. Express, 26: 7404-7422.

Sei, A., 2015. Efficient Correction of Adjacency Effects for High-Resolution Imagery: Integral Equations, Analytic Continuation, and Padé Approximants. Appl. Opt. 2015, 54, 3748.

Serrano, J., Shahidian, S., Da Silva, J.M., 2019. Evaluation of Normalized Difference Water Index as a Tool for Monitoring Pasture Seasonal and Inter-Annual Variability in a Mediterranean Agro-Silvo-Pastoral System. Water (Switzerland) 11 (1).

Shimabukuro, Y.E., Ponzoni, F.J., 2017. Spectral Mixture for Remote Sensing. Linear Model and Applications, Springer Nature: Basel, Switzerland: 1-8.

Shoaf, W.T., Lium, B.W., 1976. Improved extraction of chlorophyll a and b from algae using dimethyl sulphoxide. Limnol. Oceanogr., 21: 926-928.

Sit, M., Demiray, B. Z., Xiang, Z., Ewing, G.J., Sermet, Y., Demir, I., 2020. A comprehensive review of deep learning applications in hydrology and water resources. Water Sci. Technol., 82 (12): 2635-2670.

SNAP v8.0- ESA Sentinel Application Platform. Available at: http://step.esa.int.

Sobel, R.S., Kiaghadi, A., Rifai, H.S., 2020. Modeling water quality impacts from hurricanes and extreme weather events in urban coastal systems using Sentinel-2 spectral data. Environ Monit Assess 192, 307.

Soomets, T., Uudeberg, K., Jakovels, D., Brauns, A., Zagars, M., Kutser, T., 2020. Validation and comparison of water quality products in baltic lakes using Sentinel-2 MSI and Sentinel-3 OLCI Data. Sensors, 20, 742.

Soriano-González, J., Angelats, E., Fernández-Tejedor, M., Diogene, J., Alcaraz, C. First Results of Phytoplankton Spatial Dynamics in Two NW-Mediterranean Bays from Chlorophyll-a Estimates Using Sentinel 2: Potential Implications for Aquaculture. Remote Sens. 2019, 11, 1756.

Soriano-González, J., Angelats, E., Martínez-Eixarch, M., Alcaraz, C., 2020. Rice farming and macrophyte dynamics monitoring through Sentinel-2 MSI as a proxy of disturbance of agricultural practices over an enclosed bay. Proceedings of FIG Working Week 2020, 10-14 May.

Sòria-Perpinyà, X., Vicente, E., Urrego, P., Pereira-Sandoval, M., Tenjo, C., Ruíz-Verdú, A., Delegido, J., Soria, J.M., Peña, R., Moreno, J. 202. Validation of water quality monitoring algorithms for Sentinel-2 and Sentinel-3 in Mediterranean inland waters with *in situ* reflectance data. Water., 13, 686.

Spyrakos, E., O'Donnell, R., Hunter, P.D., Miller, C., Scott, M., Simis, S.G.H., Neil, C., Barbosa, C.C.F., Binding, C.E., Bradt, S., Bresciani, M., Dall'Olmo, G., Giardino, C., Gitelson, A.A., Kutser, T., Li, L., Matsushita, B., Martinez-Vicente, V., Matthews, M.W., Ogashawara, I., Ruiz-Verdú, A., Schalles, J.F., Tebbs, E., Zhang, Y., Tyler, A.N., 2018. Optical types of inland and coastal waters. Limnol. Oceanogr., 63: 846-870.

Steinmetz, F., Deschamps, P.Y., Ramon, D., 2011. Atmospheric Correction in Presence of Sun Glint: Application to MERIS, Opt. Express, 19 (10): 9783-9800.

Sutherland, T.F., Leonard, C., Taylor, F.J.R., 1992. A Segmented Pipe Sampler for Integrated Profiling of the Upper Water Column. J. Plankton Res., 14: 915-923.

T

Tavares, M.H., Lins, R.C., Harmel, T., Fragoso, C.R., Martínez, J.M., Motta-Marques, D., 2021. Atmospheric and sunglint correction for retrieving chlorophyll-a in a productive tropical estuarine-lagoon system using Sentinel-2 MSI imagery. ISPRS J. Photogramm. Remote Sens., 174: 215-236.

Tavus, B., Kocaman, S., Nefeslioglu, H.A., Gokceoglu, C., 2020. A fusion approach for flood mapping using sentinel-1 and sentinel-2 datasets. Int. Arch. Photogramm. Remote Sens. Spat. Inf. Sci.-ISPRS Arch. 43: 641-648.

Toming, K., Kutser, T., Laas, A., Sepp, M., Paavel, B., Nõges, T., 2016. First experiences in mapping lake water quality parameters with Sentinel-2 MSI imagery. Remote Sens., 8, 640: 1-14.

Tornos, L., Huesca, M., Dominguez, J.A., Moyano, M.A, Cicuendez, V., Recuero, L., and Palacios-Orueta, A., 2015. Assessment of MODIS Spectral Indices for Determining Rice Paddy Agricultural Practices and Hydroperiod. ISPRS Journal of Photogrammetry and Remote Sensing, 101: 110-24.

U

Ustin, S.L., 2004. Remote sensing for natural resource management and environmental monitoring (3rd ed.). John Wiley & Sons.

Uudeberg, K., Ansko, I., Põru, G., Ansper, A., Reinart, A., 2019. Using optical water types to monitor changes in optically complex inland and coastal waters. Remote Sens., 11, 2297.

V

Van Niel, T.G., McVicar, T., 2004. Current and potential uses of optical remote sensing in rice-based irrigation systems: A review. Australian Journal of Agricultural Research, 55: 155-185.

Vanhellemont, Q., Ruddick, K., 2018. Atmospheric Correction of Metre-Scale Optical Satellite Data for Inland and Coastal Water Applications. Remote Sens. Environ., 216: 586–597.

Volpe, G., Santoleri, R., Vellucci, V., Ribera d'Alcalà, M., Marullo, S., D'Ortenzio, F., 2007. The Colour of the Mediterranean Sea: Global versus Regional Bio-

Optical Algorithms Evaluation and Implication for Satellite Chlorophyll Estimates. Remote Sens. Environ., 107: 625-638.

Vos, K., Splinter, K., Harley, M., Simmons, J., Turner, I., 2019. CoastSat: A Google Earth Engine-enabled Python toolkit to extract shorelines from publicly available satellite imagery. Environmental Modelling & Software, 122, 104528.

W

Wan, L., Cen, H., Zhu, J., Zhang, J., Zhu, Y., Sun, D., Du, X., Zhai, L., Weng, H., Li, Y., Li, X., Bao, Y., Shou, J., He, Y., 2020. Grain Yield Prediction of Rice Using Multi-Temporal UAV-Based RGB and Multispectral Images and Model Transfer – A Case Study of Small Farmlands in the South of China. Agricultural and Forest Meteorology, 291, 108096.

Wang, H., Chen, J., Wu, Z., Lin, H. 2012. Rice Heading Date Retrieval Based on Multi-Temporal MODIS Data and Polynomial Fitting. International Journal of Remote Sensing, 33 (6): 1905-16.

Wang, L., Zhang, F-C., Jing, Y-S., Jiang, X-D., Yang, S-B., Han, X.M., 2014. Multi-Temporal Detection of Rice Phenological Stages Using Canopy Stagespectrum. Rice Science, 21 (2): 108-15.

Wang, T., Shi, J., Letu, H., Ma, Y., Li, X., Zheng, Y., 2019. Detection and removal of clouds and associated shadows in satellite imagery based on simulated radiance fields. Journal of Geophysical Research: Atmospheres, 124, 7207-7225.

Wang, Y., 2011. Smoothing Splines: Methods and Applications. Ed. by F Bunea, V Isham, N Keiding, T Louis, R.L. Smith, and H Tong. Smoothing Splines: Methods and Applications. Santa Barbara, California, USA: CRC Press.

Warren, M.A., Simis, S.G.H., Martinez-Vicente, V., Poser, K., Bresciani, M., Alikas, K., Spyrakos, E., Giardino, C., Ansperd, A., 2019. Assessment of atmospheric correction algorithms for the Sentinel-2A MultiSpectral Imager over coastal and inland waters. Remote Sens Environ., 225: 267-289.

Wetz, M.S., Yoskowitz, D.W., 2013. An 'extreme' future for estuaries: Effects of extreme climatic events on estuarine water quality and ecology. Marine Pollution Bulletin, 69(1), 7-18.

Wu, M., Yang, C., Song, X., Hoffmann, W.C., Huang, W., Niu, Z., Wang, C., Li, W. and Yu, B., 2018. Monitoring cotton root rot by synthetic Sentinel-2 NDVI time series using improved spatial and temporal data fusion. Sci Rep, 8 (1).

X

Xiao, X, Boles, S, Liu, J, Zhuang, D, Frolking, S, Li, C, Salas, W, Moore, B., 2005. Mapping Paddy Rice Agriculture in Southern China Using Multi-Temporal MODIS Images, Remote Sens. Environ., 95: 480-492.

Xu, H., 2006. Modification of normalised difference water index (NDWI) to enhance open water features in remotely sensed imagery. International Journal of Remote Sensing, 27: 3025-3033.

Xue, L., Li, G., Qin, X., Yang, L., and Zhang, H., 2014. Topdressing Nitrogen Recommendation for Early Rice with an Active Sensor in South China. Precision Agric., 15: 95-110.

Y

Yang, D., Yang, C., 2009. Detection of Seagrass Distribution Changes from 1991 to 2006 in Xincun Bay, Hainan, with Satellite Remote Sensing. Sensors, 9: 830-844.

Yentsch, C.S., Menzel, D.W., 1963. A Method for the Determination of Phytoplankton Chlorophyll and Phaeophytin by Fluorescence. Deep Res. Oceanogr. Abstr., 10: 221–231.

Z

Zeng, L., Wardlow, B.D., Xiang, D., Hu, S., Li, D. 2020. A Review of Vegetation Phenological Metrics Extraction Using Time series, Multispectral Satellite Data. Remote Sensing of Environment, 237: 111511.

Zhang, B., Liu, X., Liu, M., Meng, Y., 2019. Detection of Rice Phenological Variations under Heavy Metal Stress by Means of Blended Landsat and MODIS Image Time Series. Remote Sensing, 11 (1).

Zhang, R., Sun, D., Li, S., & Yu, Y., 2013. A stepwise cloud shadow detection approach combining geometry determination and SVM classification for MODIS data. International Journal for Remote Sensing, 34(1): 211 226.

Zhao, H., Fu, Y.H., Wang, X., Zhao, C., Zeng, Z., Piao, S., 2016. Timing of Rice Maturity in China Is Affected More by Transplanting Date than by Climate Change. Agricultural and Forest Meteorology, 216: 215–20.

Zheng, H., Cheng, T., Yao, X., Deng, X., Tian, Y., Cao, W., Zhu, Y., 2016. Detection of rice phenology through time series analysis of ground-based spectral index data. F. Crop. Res., 198: 131-139.

Zhu, Z., Wulder, M.A., Roy, D.P., Woodcock, C.E., Hansen, M.C., Radeloff, V.C., Healey, S.P., Schaaf, C., Hostert, P., Strobl, P., Pekel, J-F., Lymburner, L., Pahlevan, N., and Scambos, T.A., 2019. Benefits of the free and open Landsat data policy. Remote Sensing of Environment, 224: 382-385.

Research activity

The following references have been produced during the present investigation:

INTERNATIONAL PAPERS

1. **SORIANO-GONZÁLEZ, J.**, ANGELATS, E., FERNÁNDEZ-TEJEDOR, M., DIOGENE, J., ALCARAZ, C. First Results of Phytoplankton Spatial Dynamics in Two NW-Mediterranean Bays from Chlorophyll-*a* Estimates Using Sentinel 2: Potential Implications for Aquaculture. *Remote Sensing*. 2019, 11, 1756.

2. **SORIANO-GONZÁLEZ, J.**, ANGELATS, E., MARTÍNEZ-EIXARCH, M., ALCARAZ, C. Monitoring rice crop and yield estimation with Sentinel-2 data. *Field Crops Research*, 281, 2022.

3. **SORIANO-GONZÁLEZ, J.**, URREGO, E.P., SÒRIA-PERPINYÀ, X., ANGELATS, E., ALCARAZ, C., DELEGIDO, J., RUÍZ-VERDÚ, A., TENJO, C., VICENTE, E., MORENO, J. Towards the combination of C2RCC processors for improving water quality retrieval in inland and coastal areas. *Remote Sensing*. 2022, 14, 1124.

4. GAMBÍN, A., ANGELATS, E., **SORIANO-GONZÁLEZ**, **J.**, MIOZZO, M., AND DINI, P. Sustainable Marine Ecosystems: Deep Learning for Water Quality Assessment and Forecasting. *IEEE Access*, 2021, 9, 121344-121365.

INTERNATIONAL CONFERENCE PAPERS

1. **SORIANO-GONZÁLEZ, J.**, ANGELATS, E., MARTINEZ-EIXARCH, MAITE., ALCARAZ, C. Rice farming and macrophyte dynamics monitoring through Sentinel-2 MSI as a proxy of disturbance of agricultural practices over an enclosed bay. Conference paper in FIG Working Week. 2020, May. Amsterdam (Netherlands)

2. ANGELATS, E., **SORIANO-GONZÁLEZ, J.**, FERNÁNDEZ-TEJEDOR, M., ALCARAZ, C. Combined inundation and water quality monitoring during short extreme events using Sentinel-2: The case of study of Gloria storm in Ebro Delta. Proceedings of XXIVth ISPRS Congress, Niece, 06-11 June, 2022.

NATIONAL CONFERENCE PAPERS

1. **SORIANO-GONZÁLEZ, J.**, ANGELATS, E., ALCARAZ, C. Sentinel 2: Una nueva herramienta para la gestión sostenible de la acuicultura en zonas costeras. XVII Conference paper in Congreso Nacional de Acuicultura. 2019, May. Cartagena (Spain)

2. ANGELATS, E., **SORIANO-GONZÁLEZ, J.**, ALCARAZ, C. Automatic mapping of Seagrass beds in Alfacs Bay using Sentinel 2 imagery. Conference paper in X Jornadas de Geomorfología Litoral. 2019, September. Barcelona (Spain)

CONFERENCE POSTERS

1. **SORIANO-GONZÁLEZ, J.**, ANGELATS, E., FERNÁNDEZ-TEJEDOR, M. Chlorophyll-a estimation from Sentinel-2 imagery in Ebro Delta bays: application to aquaculture management. Poster presetation at Ocean Optics XXIV. 2018, October. Dubrovnik (Croatia)

2. **SORIANO-GONZÁLEZ, J.**, ANGELATS, E., ALCARAZ, C. Sentinel-2 MSI Imagery pre-processing strategy for improving chl-a monitoring at Ebro Delta bays (NW-Mediterranean, Spain). Poster presentation at ESA living planet symposium. 2019, May. Milan (Italy)

3. URREGO, E.P., DELEGIDO, J., TENJO, C., RUIZ VERDÚ, A., **SORIANO GONZÁLEZ, J.**, PEREIRA SANDOVAL, M., SÒRIA PERPINYÀ, X., VICENTE, E., SORIA, J.M & MORENO, J. Validation of chlorophyll a and total suspended matter products generated by C2RCC processor using Sentinel 2 and Sentinel 3 satellites in inland waters. Poster at *XX Congreso de la Asociación Ibérica de Limnología*. 2020, June. Murcia (Spain).

SHORT STAYS IN SPAIN

2019 IPL*, Image Processing Laboratory (University of Valencia, Valencia, Spain)*
Learning the theory and practice of above-water radiometry measurements. Colaborating in field surveys, extending them to coastal waters (Ebro Delta), and starting a research between IPL, IRTA and CTTC on the validation of atmospheric correction processors in inland and coastal waters.
Duration: 4 months (1 Jul – 30 Oct)
Advisor: Dr. Jesús Delegido
Financing: Grant 2019FI_B1 00195

NATIONAL AND INTERNATIONAL PROJECTS

HEIMDALL: Multi-hazard cooperative management tool for data exchange. Coordinador: DLR. Programa H2020-SEC-2016-2017. Topic: SEC-01-DRS-2016. 261.125 €. 2017-2020.

SEN2BAYS: Generació d'una sèrie temporal de mapes de Chl-*a* de les badies del Delta del Ebre durant el període 1 Octubre 2019 – 30 de Setembre 2021. Projecte industrial per a IRTA (ESP). 14.500€. 2021.